Jose Romero Lopera

Statistical Analysis of Flux Ropes in the Plasma Sheet of the Magnetotail

MASTERARBEIT

zur Erlangung des akademischen Grades

Diplom-Ingenieur

Masterstudium Elektrotechnik

eingereicht an der

Technischen Universität Graz

Betreuer

Ao. Univ.-Prof. Dipl.-Ing. Dr.techn. Erich Leitgeb

Institut für Hochfrequenztechnik

Betreuerin IWF / ÖAW: Doz. Dr. Rumi Nakamura

Graz, März 2017

Statistical Analysis of Flux Ropes in the Plasma Sheet of the Magnetotail

Master's thesis

Jose Romero Lopera

Institute of Microwave and Photonics Engineering
Graz University of Technology

in cooperation with

Graz Institut für Weltraumforschung
Österreichische Akademie der Wissenschaft

TU Graz Supervisor: Ao. Univ.-Prof. Dr. Erich Leitgeb
IWF Supervisor: Doz. Dr. Rumi Nakamura

Graz, March 2017

Abstract

The aim of this study is the identification and analysis of small scale magnetic flux ropes existing during periods of multiple magnetic reconnection (with multiple X-line formation) on the Earth's magnetotail.

The data from the ESA Cluster mission are evaluated for a series of previously selected events where magnetic reconnection with multiple X-line formation takes place. The Cluster mission consists of 4 identical spacecraft which fly in an adjustable tetrahedron formation, allowing a multi-scale analysis of the regions covered by the orbit of the mission. Data from 2001 to 2005, the first 5 years of the Cluster mission, is analyzed on this work.

An automatic detection algorithm for the identification of small scale magnetic flux ropes is developed. The algorithm uses a search criterion based on known models of flux ropes presented in previous works, where the measurements of the vectorial components of the magnetic field should match very characteristic patterns. The proper adjustment of the search criteria is the key to detect real small scale flux rope structures and to avoid fake detections. The proper development of this automatic detection algorithm is the first of the two core sections of this work.

The second main section of this work is the statistical analysis of the detected flux ropes. The statistics performed are meant to study the properties of the magnetic flux ropes and get a better understanding of its nature. The following characteristics of flux ropes are examined: duration and size; spatial distribution and direction of motion; relationship between core field, background magnetic field, Hall field and guide field.

The statistical study of spatial distribution shows how the flux ropes are distributed in space and in which direction they move. The result obtained from this analysis shows how most of the flux ropes are located on the earthward side of the X-line and are moving towards the earth.

The core field study shows how the polarity of the background magnetic field is coherent with the polarity of the hall field and how the polarity of the core field is driven up to some extent by the combined effect of the Hall field and the guide field polarity.

The statistical analysis of the flux ropes' duration and size leads to no clear conclusions of how these parameters are influenced depending on their position relative to the X-line, although a very interesting result is obtained from those statistics. There are some flux ropes in one region of the southern hemisphere which experience a motion directed towards the X-line, contrary to what should be expected. This motion was predicted in some previous studies based in fully-kinetic simulations, which makes this result very interesting to consider.

Kurzfassung

Das Ziel dieser Masterarbeit ist die Identifizierung und Analyse von kleinen Strukturen magnetischer Flußröhren, die während Perioden mehrfacher magnetischer Rekonnexion (mit mehrfacher Entstehung von X-Linien) im Magnetschweif der Erde auftreten.

Für eine Reihe vorausgewählter Ereignisse, bei denen magnetische Rekonnexion mit Entstehung mehrfacher X-Linien auftritt, werden Daten der ESA Cluster-Mission ausgewertet. Die Cluster-Mission besteht aus vier identischen Satelliten, die in einer einstellbaren Tetraeder-Formation fliegen, wodurch eine Multi-Skalen-Analyse von Regionen möglich ist, die von der Mission abgedeckt werden. In dieser Arbeit werden Daten aus den ersten fünf Jahren der Mission (2001 bis 2005) analysiert.

Ein Algorithmus für die automatische Detektion der kleinen Flußröhren-Strukturen wird entwickelt. Der Algorithmus verwendet Suchkriterien, die auf bereits bekannten Flußröhren-Modellen vorheriger Arbeiten aufbauen. Dabei sollen die Messungen der Vektorkomponenten des Magnetfeldes sehr charakteristischen Mustern entsprechen. Die geeignete Anpassung der Suchkriterien ist von großer Wichtigkeit für die Erkennung von realen kleinen magnetischen Flußöhren und zur Vermeidung von unechten Detektionen. Die Entwicklung dieses automatischen Detektions-Algorithmus ist der erste von zwei Hauptteilen dieser Arbeit.

Der zweite Hauptteil dieser Arbeit ist die statistische Analyse der detektierten Flußröhren. Mit den durchgeführten Statistiken sollen die Eigenschaften der magnetischen Flußröhren untersucht und ein besseres Verständnis ihrer Beschaffenheit erreicht werden. Es werden folgende Eigenschaften von magnetischen Flußröhren untersucht: Dauer und Größe; Raumverteilung und Bewegungsrichtung; Beziehungen zwischen Kernfeld, Hintergrundmagnetfeld, Hall-Feld und Führungsfeld ('guide field').

Die statistische Studie der Raumverteilung zeigt die Position von Flußröhren im Weltraum und in welche Richtung sie sich bewegen. Die Ergebnisse dieser Analyse zeigen, dass sich die meisten Flußröhren auf der der Erde zugewandten Seite der X-Linie befinden und sich zur Erde hin bewegen.

Die Untersuchung des Kernfelds zeigt, wie die Polarität des Hintergrundmagnetfeldes mit der Polarität des Hall-Feldes zusammenhängt, und wie die Polarität des Kernfeldes vom Zusammenwirken des Hall-Felds und der Polarität des 'guide field' bis zu einem gewissen Grad beeinflusst wird.

Die statistische Analyse von Dauer und Größe der Flußröhren führt zu keinem klaren Ergebnis darüber, wie diese Parameter abhängig von der relativen Position zur X-Linie beeinflusst werden, obwohl aus dieser Statistik ein sehr interessantes Ergebnis hervorgeht. Es gibt einige Flußröhren in einer Region der südlichen Halbkugel, die sich zur X-Linie hin bewegen, im Gegensatz zu den Erwartungen. Diese Bewegung wurde schon in einigen vorherigen, auf völlig kinetischen Simulationen basierenden Studien vorhergesagt. Deshalb ist das Ergebnis der statistischen Analyse als sehr interessant einzustufen.

Deutsche Fassung:
Beschluss der Curricula-Kommission für Bachelor-, Master- und Diplomstudien vom 10.11.2008
Genehmigung des Senates am 1.12.2008

EIDESSTATTLICHE ERKLÄRUNG

Ich erkläre an Eides statt, dass ich die vorliegende Arbeit selbstständig verfasst, andere als die angegebenen Quellen/Hilfsmittel nicht benutzt, und die den benutzten Quellen wörtlich und inhaltlich entnommene Stellen als solche kenntlich gemacht habe.

Graz, am ……. ……..
(Unterschrift)

Englische Fassung:

STATUTORY DECLARATION

I declare that I have authored this thesis independently, that I have not used other than the declared sources / resources, and that I have explicitly marked all material which has been quoted either literally or by content from the used sources.

……. ……..
date (signature)

Acknowledgments

This work was realized under the supervision of Erich Leitgeb for the institute of Microwave and Photonics Engineering of the Technical University of Graz, in cooperation with the Space Science Institute of Graz under the supervision of Rumi Nakamura.

I would like to express my immense gratitude to Rumi Nakamura, who gave me the opportunity of working in this project and so gave me also the chance to be part of the space research scientific community, something I have always wishful thought about it. I am also with all my hearth grateful to her for all the patience she had during this year I was under her supervision and all the support I always received from her side when I needed it, without her help this work would not have been possible and this thesis will today not be a reality. I would always keep a good memory of her not only as a scientist, but also as person.

I knew for the first time Erich Leitgeb during an Excursion to Zagreb on the first semester of this Master. We had a very comfortable and interesting talk during the excursion, this is why he was the first person that came to my mind when I had to look for a supervisor at the University for my Thesis. He always made everything easy and supported me a lot during the time I was dedicated to this work. Besides being an excellent professor, he is one of the more friendly and kind persons I have ever met, and I will always keep a good memory of him.

I would also like to specially thank Takuma Nakamura for all his help and the time he spent with me discussing over my results. He always was disposed to met and add his valuable opinion, without which this work may absolutely not be the same. He is also a very kind person, to whom I desire the best for his future.

I would like to dedicate also some lines to the persons with whom I shared my day-to-day in IWF. My office college and current friend Ali Varsani, with whom I shared office during the first half year of this thesis and we developed a strong friendship that hopefully will last forever. Also to Zoltan Vöros, who was like a parental figure for me and to Kristina Kyslyakova who always brought good mood to our 'cultural-exchange' lunchtimes. I would like to thank them all for making going there everyday a very pleasant experience, and for all the interesting talks we had during the lunchtimes.

I want to express also my biggest and immense gratitude to my parents and my sister, who always supported me during all this time and encouraged me to never give up and look forward. Without their unconditional support and affection none of this work and even the whole Master would have been possible. Thank you for always believe in me.

But if there is one person to whom I would like to dedicate the most emotive part of this acknowledgments section is my sentimental partner, and the love of my life Patricia Mesa Ortega. She was always at my side during the whole time I was dedicated to this work and she gave me strength through love, affection and a big smile every day. I love you Patricia, thank you for always being there.

Last before closing this section I would like to dedicate these lines to my high school

maths professor Amor Segura, who I consider one of the best professors I ever had. She was not only my professor, but also a friend and still nowadays after many years and two University studies I keep a small place for her in my memories.

Thanks also to the Austrian academy of sciences for the possibility of realizing this work, it was was a very enriching experience for me which I will never forget.

Graz, im January 2017 Jose Romero Lopera

Contents

1 Introduction

Plasma is a state which can be said to be the 4th state of matter. It consists on negative and positive charged particles which are present in equal numbers in order to restore quasi-neutrality of the entire gas they conform. It is formed when a gas reaches extremely high temperatures, as the particles this gas is made up are ionized with increasing temperature and they overcome the strong Coulomb forces for temperatures sufficiently high. Plasmas are characterized depending on its temperature and density among other parameters and despite its quasi-neutral behavior, they are sensitive to electric and magnetic fields and can carry electric currents.

On the one hand artificial plasmas can be generated in a laboratory under certain conditions and are an important field of research for the realization of the nuclear fusion, which will be hopefully the main energy source in a distant future. On the other hand natural plasmas exist already in the space, for example as the raw material which forms the stars, or in the surrounding of planets which possess a magnetic field, like the Earth. Information regarding this plasma is hard to achieve, this is the reason why space missions are meant to. Particularly, the cluster mission, which will be used as data source for this work supplies information about plasma and magnetic field in the near Earth environment, which will be the basis of this work.

The cluster mission from the ESA launched in 2000 was designed to analyze the environment that surrounds the Earth, and provides the data which will be used for this work. The cluster satellites orbit around the earth, crossing periodically during its orbit the region of the tail, located on the opposite side of the Sun. There, the phenomenon known as magnetic reconnection occurs as a consequence of the interaction between the incoming solar wind expelled from the Sun and the Earth's magnetic field. The magnetic field lines that compose the solar wind and those correspondents to the magnetic field of the earth merge under some specific conditions, and so new field lines are formed and the plasma contained inside each of those magnetic field lines are combined.

When magnetic reconnection happens, the magnetic field lines merge and change topology, consequently the plasma which was frozen-in inside those lines is mixed. Reconnection in the magnetosphere was proposed by James Dungey in 1961 as a cycle starting on the dayside where magnetic field lines of the magnetopause were joined by the incoming field lines of the solar wind; those will travel then to the night side of the magnetosphere and reconnect again to reach stability. In such a way the plasma located inside the earth magnetosphere is constantly supplied by plasma from the solar wind.

After magnetic reconnection, the magnetic field energy exchanged during the process is converted into acceleration of the particles that form the plasma. These particles can travel then along the magnetic field lines to the earth, more precisely to the poles, where the magnetic field lines close and then generate electric currents in the Ionosphere, this triggers the phenomenon which we know as the aurora. This will be more intense during periods of

strong solar activity or sporadic sunstorms, as magnetic reconnection will occur at a higher rate.

1.1 Structure

If single or multiple magnetic reconnection occurs, some helical magnetic structures known as flux ropes can be generated during the process and be swept with the motion of the magnetic field lines; either directed to the earth if they are generated in the earthward side or far away from the earth, directed to the tail. The main objective of this work is the detection and analysis of the nature of such structures. The phenomena previously mentioned will be explained in detail in chapter 2.

Flux ropes are structures complicated to detect, therefore the instrumentation onboard the four Cluster spacecrafts will be used to analyze the data collected during periods of multiple reconnection on the magnetotail. The details regarding the Cluster mission and the instruments carried by each spacecraft can be found in chapter 3, which is dedicated in its totality to the Cluster mission.

A detection algorithm is developed to look for the existence of flux ropes contained among the data from the cluster mission. The algorithm will check if the patterns of the magnetic field components on the data resemble the characteristic patterns of a flux rope. The development of the detection algorithm can be found in chapter 4.

The collection of flux ropes detected will be submitted under statistical analysis in order to understand the nature of the parameters which characterize a flux rope. The studies considered for the statistical analysis will focus on: duration and length; position and direction of movement relative to the X-line; factors which could influence the polarity of the core and background magnetic field.

The statistical analysis realized for this work and its correspondent conclusions can be found in chapter 5.

1.2 Motivation of the work

The two first chapters of this thesis will introduce all the theoretical basis and the characterization of the instruments of the Cluster mission. It may be interesting to highlight the main objective of this work before going further into the more technical details of Chapters 4 and 5 to keep a good perspective of what is actually looked for.

The motivation for this work is based on the study of small scale magnetic flux ropes in the plasma sheet of the magnetotail which may be generated during periods of multiple X-line reconnection. The mechanisms which originate these flux ropes are uncertain, although some studies based on fully-kinetic simulations *[Nakamura. et. al, 2016; Daughton.et.al, 2006; Daughton.et.al, 2011; Lapenta.et.al 2015]*][9, 6, 7, 8], have predicted that those flux ropes may be generated during secondary reconnection processes taking place inside the primary reconnection sites generated during multiple X-line magnetic reconnection.

Based on those simulation results, it may be interesting to examine the existence and characteristics of those predicted small scale flux ropes using real measurements from the Cluster mission during periods of magnetic reconnection. A list of previously identified

multiple X-line reconnection events *[Alexandrova, 2016]*[4] will be taken as database for this Thesis. The data collected from the Cluster spacecraft will be examined to check the existence of small scale flux rope structures among it. For this purpose an automatic detection algorithm is developed. The development of the detection algorithm and the criteria over which this algorithm is constructed is commented in detail in Chapter 4.

After the flux ropes are registered and a database of flux ropes is generated, a series of statistical studies of these small scale flux ropes will be realized in Chapter 5. The statistical study is thought to put some light on the nature of these small scale flux ropes and determine how its characteristics are influenced by different factors. The results obtained from these analysis may also corroborate or contradict the predictions obtained from the simulations, being this one of the motivations for the realization of this study in this thesis.

The results obtained from this study are expected to increase the actual knowledge regarding the small scale flux ropes, whose nature and formation mechanisms are still poorly understood. The conclusions obtained from this thesis are intended to open new directions of research into which further studies could be directed.

2 Fundamentals

The Earth is the 3^{rd} planet of the solar system located at a distance of about $150 \cdot 10^6$Km from the sun. This distance is the average distance that separates the earth during its complete orbit around the sun and it is referred to as Astronomical Unit (AU) corresponding exactly to 149.597.870.700 meters. This distance may seem huge, but as the diameter of the sun is about 1.392.000 Km, up to 109 times as great as the Earth's diameter of 12.742 Km, the influence of the sun on the Earth would have lethal consequences if the earth would not be protected of the impinging radiation from the solar wind.

Solar wind consists on magnetic field lines and ionized particles conforming plasma that are expelled from the sun and travel through the space. The magnetosphere plays this shielding role, deflecting the magnetic field lines of the solar wind and protecting the earth from the solar radiation, when the solar wind crosses the earth in its trajectory.

Under certain conditions, the interaction between the Earth's magnetosphere and the impinging solar wind will lead to a phenomenon called *magnetic reconnection*, which is at the same time related with the formation of a certain kind of magnetic structures called *flux ropes*.

This chapter will be dedicated to the basis of all this definitions and processes previously mentioned.

2.1 The Magnetosphere

The Earth possesses its own magnetic field, which is thought to be generated based on the Dynamo theory by a convecting, rotating and electrically conducting fluid. In the Earth this fluid consists on liquid iron that flows on the outer core of the earth, driven by heat flow from the inner core. This flow acquires a helical trajectory due to the effect of the coriolis force which creates helical circulating currents and so, the Earth's magnetic field is generated.

As the solar wind approaches the earth, the magnetic field of this solar wind, which is called Interplanetary Magnetic Field (IMF) is deflected by the magnetic field of the Earth. The solar wind flows around and so is the earth confined inside. This region is called the magnetosphere and it consists of several regions contained inside of it, although due to the interaction between the IMF and the terrestrial magnetic field also important regions are defined outside of it. The main regions representing the whole picture of the Earth's magnetic field and the IMF are shown in Figures 2.1 and 2.2:

The regions Inside of the Magnetosphere are the *Magnetopause* (border), *Plasma mantle*, *Plasma sheet*, *Current sheet or neutral sheet*, *Plasmasphere* and *Ionosphere*. The regions outside of the Magnetosphere are the *Bow shock* and the *Magnetosheath*.

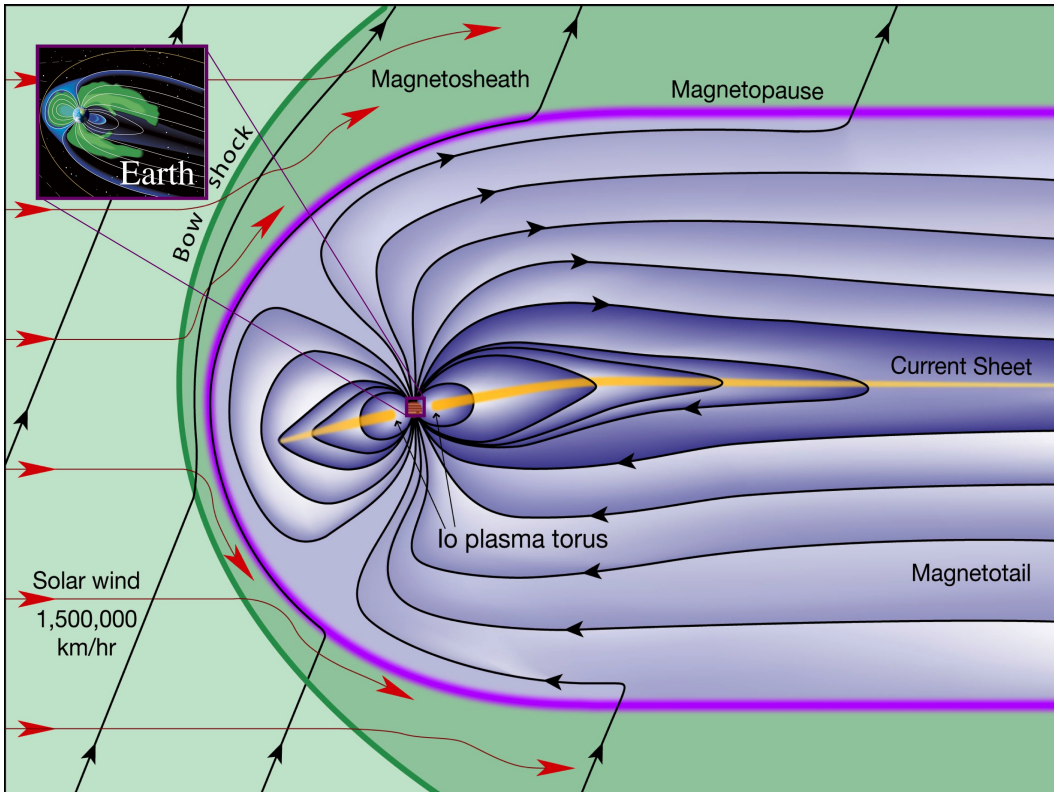

Figure 2.1: Main components of the magnetosphere in 2-D[30]

2.1.1 The Magnetopause

The **magnetopause** is the outer boundary of the magnetosphere and it is a border between the solar wind plasma and the region governed by the terrestrial magnetic field. When the solar wind collides with the Earth's magnetic it cannot freely pass through it, but is rather slowed down and deflected around it. As the solar wind reaches the Earth at supersonic speed, a static shock wave is generated and the plasma is slowed down, converting its kinetic energy into thermal energy, this region is called the *bow shock*. The slowed and heated subsonic plasma is contained in a region called the *Magnetosheath*, whose plasma density and temperature is much higher than the one initially carried by the solar wind. This hot denser plasma, mainly composed of H^+ and He^{++} ions cannot dive into the terrestrial magnetic field, since the solar wind particles are linked to the IMF lines due to the frozen-in condition for highly conducting plasmas, which will be discussed later, and those cannot penetrate the terrestrial field lines. This interface between the magnetosheath and the magnetosphere is the aforementioned *magnetopause*.

More precisely, the exact position of the magnetopause will be determined by the condition of pressure balance between the magnetosheath $P_{total\,mh}$ and the magnetosphere $P_{total\,mp}$. The total pressure in each region is composed by the plasma pressure P_p and the magnetic pressure P_B. In the magnetosheath, the plasma pressure of the solar wind dominates over the

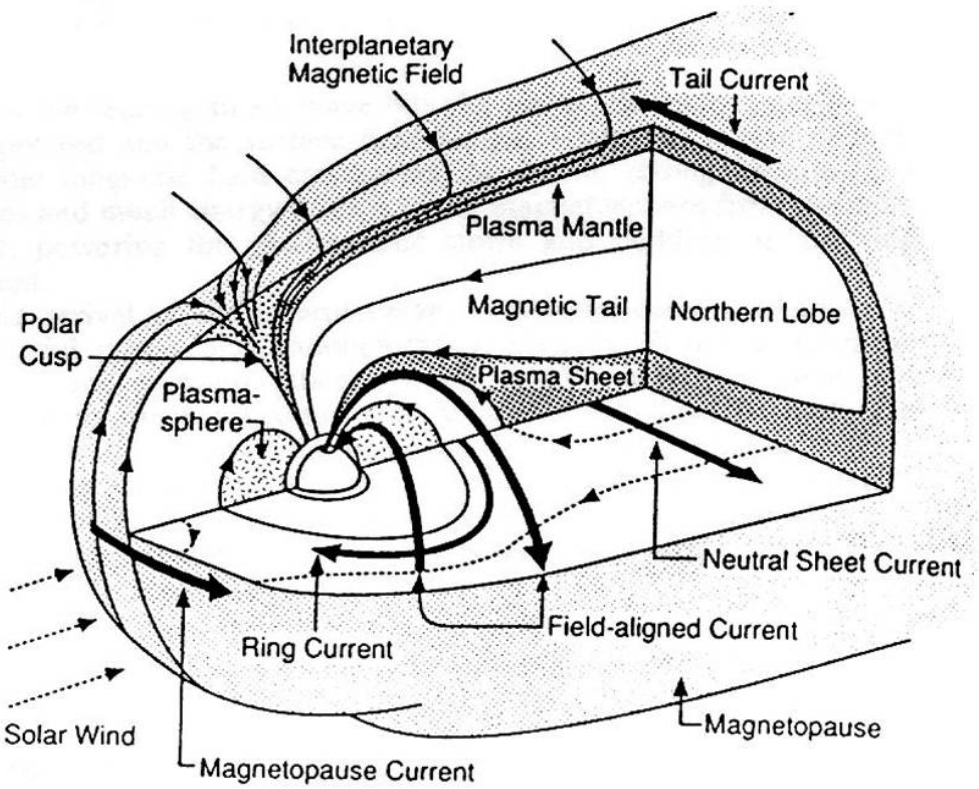

Figure 2.2: Main components of the magnetosphere in 3-D[31]

magnetic pressure, while in the magnetosphere the magnetic pressure dominates. Assuming the simplification that the total pressure is represented only by its most relevant contribution, the magnetopause will be defined when the pressure of the plasma trapped in the IMF lines contained in the magnetosheath, and the magnetic pressure of the terrestrial magnetic field are in equilibrium[2].

$$P_{total} = P_p + P_B \tag{2.1}$$

$$P_p = \frac{1}{2}\rho v^2 = nK_BT \tag{2.2}$$

$$P_p = \frac{1}{2}\rho v^2 = nK_BT \tag{2.3}$$

$$P_{p\,mh} \gg P_{p\,mh} \rightarrow P_{total\,mh} = P_{p\,mh} + P_{p\,mh} \approx P_{p\,mh} \tag{2.4}$$

$$P_{p\,mp} \ll P_{p\,mp} \rightarrow P_{total\,mp} = P_{p\,mp} + P_{p\,mp} \approx P_{B\,mp} \tag{2.5}$$

From the equations above can be noticed, that the equilibrium condition will be achieved when sufficient kinetic energy from the solar wind particles is converted into heat and the plasma is slowed down enough in the magnetosheath. The solar wind is not always constant, and it will vary depending on the solar activity and many other factors. Higher values of solar wind supersonic speeds will shift the magnetopause towards the earth, since the plasma needs to get slowed down longer in the magnetosheath, while lower supersonics speeds will cause the opposite effect. The average distance it can be found is around 14 R_E in the sunward side from the earth and around 100 R_E in the magnetotail.

2.1.2 The Magnetotail

The magnetotail comprehends the region of the magnetosphere which is oppositely directed to the sun. The magnetic field lines of the magnetosphere become elongated on the nightside, due to the effect of the solar wind, reaching distances far beyond lunar orbit up to $100R_E$. Several different regions are contained in the magnetotail: lobes; plasma sheet; current sheet or neutral sheet; plasma mantle (if frozen-in condition violated); X-line (if magnetic reconnection occurs).

Under normal circumstances, when no reconnection occurs, the lobes represent the outer part of the magnetotail. This region are separated as northern and southern lobe, and consist on oppositely directed magnetic field lines. The northern lobe is directed towards the earth and merges in the magnetic north pole while the southern lobe begins at the magnetic south pole and is directed away from the earth, both lobes are connected somewhere at a distance of $100R_E$ from the Earth, forming the closed magnetic field lines of the magnetosphere in the magnetotail. The magnetotail lobe contains a rarified plasma with typical values for the electron density and temperature, as well as the magnetic field intensity of $v \approx 10^{-2} cm^{-3}$ $T_e \approx 5 \cdot 10^5\ K$ and $B \approx 30\ nT$respectively.

The plasma sheet is a region located around the center of the magnetotail and separated by the lobes by a region called the plasma sheet boundary layer (PSBL). The electron density in this region is about $0.5cm^{-3}$, more than 10 times the plasma density from the lobes. It is also a hot region with electron temperatures of $T_e \approx 5 \cdot 10^6 K$ and lower magnetic field intensity $B \approx 10nT$. The plasma density and temperature increases for inner regions of the plasma sheet that are closer to the central plane of the magnetotail, which is called the *current sheet*.

The **current sheet** or **neutral sheet** is a relatively thin region which separates the northern and southern sides of the magnetotail, characterized by weak values of the magnetic field. This region carries electric currents called *neutral sheet currents*, which are originated according to the generalized Amperes' law *[Shay.et.al, 2001]*[5].

$$\nabla \times \mathbf{B} = \mu_0 \left(\mathbf{j} + \epsilon_0 \frac{\partial \mathbf{E}}{\partial t} \right) \tag{2.6}$$

$$\mathbf{\Delta B} = \mu_0 \mathbf{I} \tag{2.7}$$

The neutral sheet currents are a consequence of the distortion of the magnetic dipole of the earth's magnetic field in the dayside of the magnetosphere. The *magnetopause* currents

occur due to the compression of the magnetic field, while in the nightside magnetosphere, the *tail currents* and the *neutral sheet currents* appear, being both connected and forming a Θ like current system *[Baumjohann; Treumann, 1996]* [3].

The position inside the magnetotail and each corresponding region can be represented by the plasma β parameter, reaching higher values for regions closer to the current sheet. It represents the ratio between the plasma pressure and the magnetic field pressure in the magnetotail.

$$\beta = \frac{P_p}{P_B} = \frac{nkT}{\frac{B^2}{2\mu_0}} \tag{2.8}$$

From the definition of the β parameter, all the aforementioned regarding the different regions can be noticed. The lobes present a value of β below 0.25 which corresponds to regions of high magnetic field intensity and low particle density and relatively low temperature. Values of $0.25 < \beta < 2$ correspond to the PSBL where the values of the magnetic field are lower than in the lobes, while the plasma in this region is characterized by higher values of density and temperature. Values of $\beta > 2$ represent deeper regions of the plasma sheet, it reaches very high values close to the neutral sheet, where magnetic field is really weak.

Under normal circumstances, the aforementioned regions compose the Earth's magnetotail. Nevertheless, an additional region called *plasma mantle* exists in the magnetotail as boundary between the magnetopause and the lobes due to magnetic reconnection. The plasma mantle is composed by a plasma population from the magnetosheath and the ionosphere. This means that plasma from the regions out and inside of the magnetopause are combined, which only can happen if the frozen-in flux condition is violated and the magnetic field lines on the dayside are reconnected. This process is called dayside reconnection and its a part of the earth convective cycle, it will be discussed later on.

When dayside reconnection occurs, magnetosheath plasma penetrates the magnetopause and is guided along the magnetic field lines towards the poles, forming the *dayside cusp population*. The magnetic field lines converge in this point, and so is the intensity increased. The particles are bounced back due to the mirror effect and leave this region to accumulate in the *plasma mantle*. In the mantle, the particles from the solar wind, mainly H^+ and He^{++}, are mixed with Ionospheric plasma, consisting of O^+, H^+ and He^+. When magnetic reconnection in the tail occurs, the mantle plasma travels towards the center plane of the magnetotail due to the magnetic field gradient of the lobe flowing down the tail. In the X-line, the plasma from the mantle flows in and it's accelerated and expelled into the plasma sheet[2]. The whole reconnection process will be discussed later in this work.

2.1.3 Inner Magnetosphere

The *Ionosphere*, the *plasmasphere* and the *Van Allen radiation belts* comprehend the innermost part of the magnetosphere, which is almost symmetric on the day and night sides of the earth.

The **Ionosphere** is a region of the Earth's atmosphere. The neutral particles contained in the atmosphere are ionized due to the impinging solar ultraviolet radiation, recovering its neutrality due to collisions between particles. For altitudes above 80 Km, the particle density is not big enough and collisions are too infrequent to result in rapid recombination,

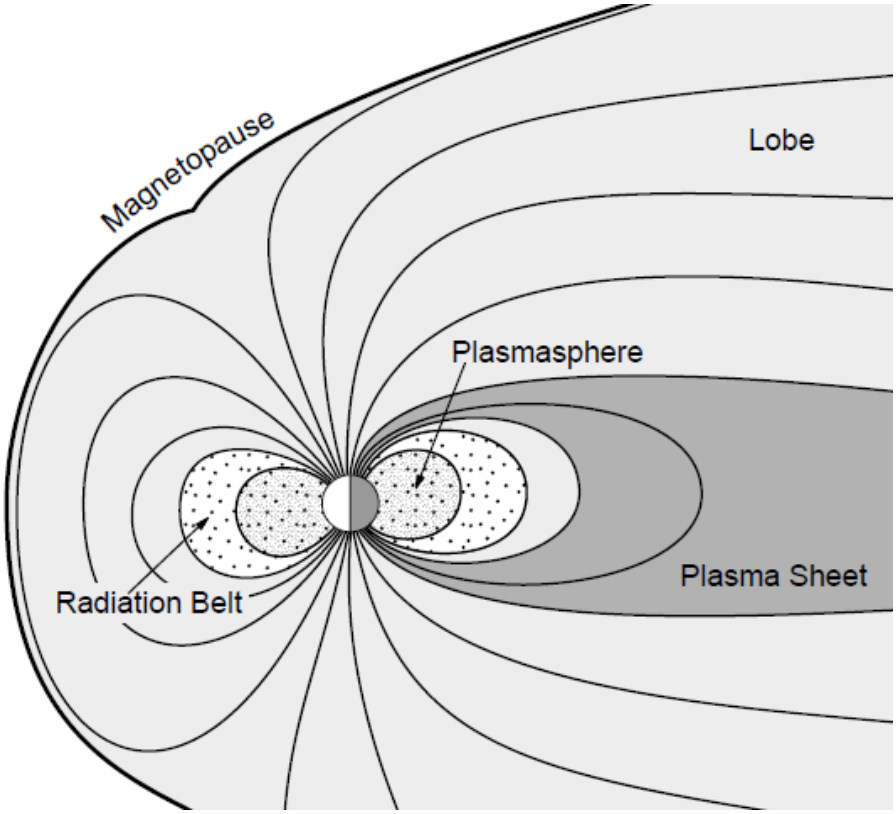

Figure 2.3: Structure of the Earth's magnetosphere showing the plasmasphere and the radiation belts [3]

so a region containing a population of permanently ionized particles is formed. This region is called the *Ionosphere* and it extends to rather high altitudes, while for low- and mid-latitudes it gradually merges in the plasmasphere. The Ionosphere is separated into lower and upper Ionosphere and structured in many different layers depending on its radio wave propagation properties *[Baumjohann; Treumann, 1996]*[3].

D-Region: The lower part of the Ionosphere above 90 Km. It is very weakly Ionized and cannot be considered a plasma due to high collision frequencies.

E-Region:First layer of the upper Ionosphere. It is formed by the absorption of longer wavelength ultraviolet radiation ($\approx 90nm$) which passes the higher altitudes until the density of molecular oxigen becomes too high around 150 Km height, thus oxigen ions dominate the E-region. This region is more ionized than the D-Region, but still partially Ionized.

F-Region:The highest layer of the upper Ionosphere, it splits into two layers, the *F1-Region* at around 200 Km and the *F2-Region* around 300 Km height. The former is a dayside feature created in the same way as the E-region, but the absorbed wavelengths are

shorter ($\approx 20 - 80nm$) because of different absorbent molecules. The most important layer in this region is the *F2-region*. Its formation is determined by the height variation of the neutral densities and the recombination and attachment rates for the different atmospheric constituents. In this way, the competition between Ionization and attachment leads to a Ionization peak at about 300 Km. This regions contains the densest plasma in the earth's environment, with electron densities up to $n_e = 10^6 cm^{-3}$

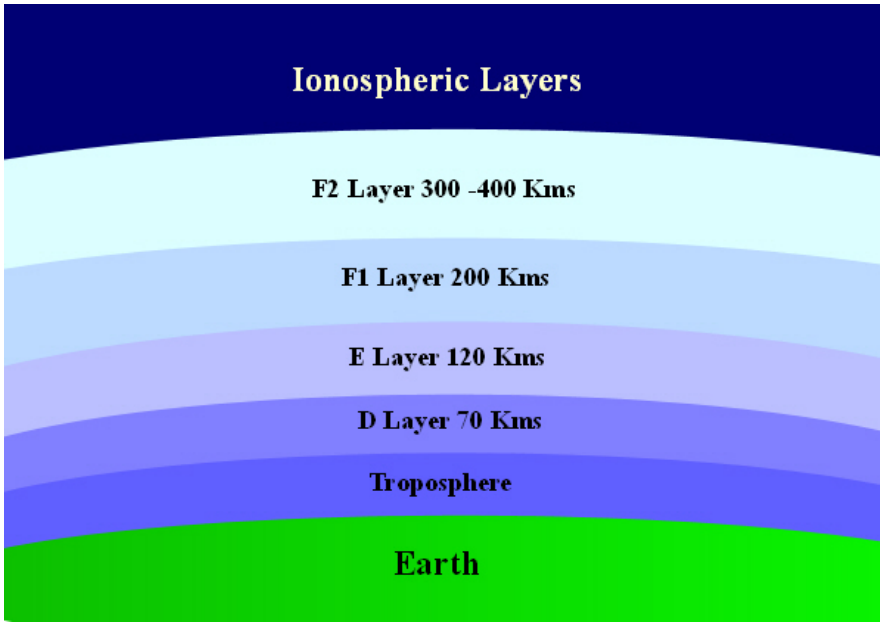

Figure 2.4: Layers of the Ionosphere [27]

The **plasmasphere** arises from the Ionosphere at altitudes, where the density is low enough to support and sustain a plasma due to low collision rate, which holds of up to about 90 Km from the ground. It is a thorus-saped volume confined inside of the radiation belt. The plasma in plasmasphere is dense and cold plasma of Ionospheric origin, with electron density and temperature of $n_e = 2 \cdot 10^2 cm^{-3}$ and $T_e = 5 \cdot 10^5 K$ respectively. It corrotates with the earth and in the equatorial plane it extends out to about 4 R_E, where the density drops sharply to about $1\,cm^{-3}$, this region is called the *plasmapause [Baumjohann; Treumann, 1996]*[3]. The Van allen Radiation Belts consists on dipolar field lines between about 2 and 6 RE. It consists on energetic electrons and Ions which move along the field lines and oscillate back and forth between the two hemispheres, although the origin of the particles of the outer and inner radiation belt is different. The outer belt consist of energetic electrons coming mainly from the outer magnetosphere, while the inner belt is composed of protons and electrons from both, outer magnetosphere and the Ionosphere. Typical electron densities and temperatures are $n_e = 1\,cm^{-3}$ and $T_e = 5 \cdot 10^7 K$ while the magnetic field intensity here ranges between 100 and 1000 nT. The belts are closely related to the aurora-phenomenon *[Baumjohann; Treumann, 1996]*[3], *[Rott, 2010]*[2].

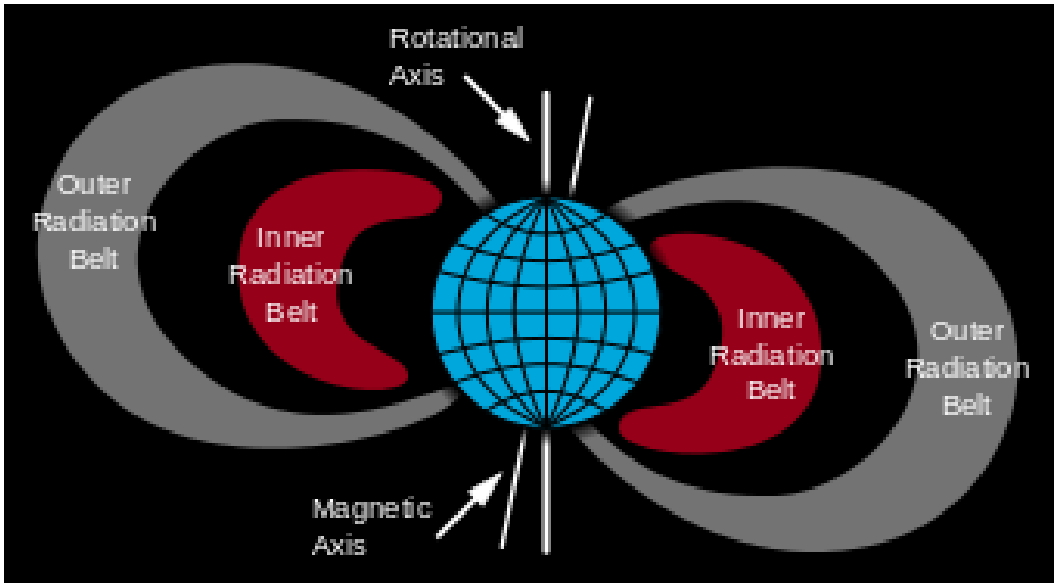

Figure 2.5: Van allen inner and outher radiation belts[28]

2.2 The Frozen-in Flux Concept

As aforementioned, the frozen-in Flux Concept is the reason why the plasma carried in the solar wind is deflected around the magnetosphere instead of penetrate it. This holds unless magnetic reconnection happens and this condition is violated.

A particle in a dipole field will gyrate, bounce and drift at the same time, being the drift motion much slower than the rest. The drift motion is differentiated into magnetic drift and electric drift. The former depends strongly in the particle energy, while the latter is a consequence of the presence of an electric field *[Baumjohann; Treumann, 1996]*[3]. Energetic particles tend to move across magnetic field lines under the influence of magnetic gradients or curvature Forces due to the magnetic drift. On the other hand, cold plasma particles with near zero energy, like magnetospheric plasma,do not feel the magnetic forces because their energy is too low. Cold particles in absence of electric fields do not experience drift in direction of magnetic field gradients and they stay close to the field lines they gyrate about. Consequently, whenever a magnetic field line is moved due to an external force, also the cold plasma tied to this field line will move together, and same situation will occur for moving cold plasma. Hence the motions of the plasma and flux tube are deeply related. This is the principle of the frozen-in flux condition.

In order to describe plasma dynamics there are two possible approaches; *single particle description* and *Magnetohydrodynamics* (MHD). On the one hand, the single particle description determines important parameters which characterize plasma like the *gyroradius*, *gyrofrequency*, *debye length* or *plasma frequency*. On the other hand, MHD describes the properties of plasma in an averaged form.

For the MHD interpretation should exist a significant population of statistically independent particles, time scales should be long compared to microscopic particle motion such

as the plasma frequency, and spatial scales large compared with the Debye length or the gyroradius. Under this conditions, the conservation laws for Energy, mass and momentum can be applied and combined with the Maxwell's equations and so is the set of MHD equations built. The frozen-in flux condition is derived from this equations*[Baumjohann; Treumann, 1996]*[3], *[Rott, 2010]*[2].

$$\frac{\partial p}{\partial t} + \nabla (p\upsilon) \qquad \text{Continuity equation} \qquad (2.9)$$

$$\mathbf{E} + \mathbf{v} \times \mathbf{B} = \frac{1}{\sigma_0}\mathbf{j} \qquad \text{Generalized Ohm's law (simplified)} \qquad (2.10)$$

$$\nabla \times \mathbf{E} = -\frac{\partial \mathbf{B}}{\partial t} \qquad \text{Faraday's law} \qquad (2.11)$$

$$\nabla \times \mathbf{B} = \mu_0 \mathbf{j} \qquad \text{Ampere's Law in MHD limit} \qquad (2.12)$$

In the previous set of equations, the Generalized Ohm's law is not shown in its complete form, since the rest of terms could be neglected for this scenario. The complete equation including all the terms as well as an explanation of the conditions under which rest of coefficients should be considered is shown in the following section as Equation 2.21 .

Combining the Electric field **E** obtained from the Generalized Ohm's law and the current density **j** from Ampere's law with Faraday's law, an expression for the magnetic field induction which is only dependent from the magnetic field B and the particle velocity **v**.

$$\frac{\partial \mathbf{B}}{\partial t} = \nabla \times (\mathbf{v} \times \mathbf{B}) + \frac{1}{\mu_0 \sigma_0} \nabla^2 \mathbf{B} \qquad (2.13)$$

In the equation, μ_0 is the magnetic susceptibility in vacuum, while σ_0 is the plasma conductivity due to Coulomb or neutral collisions defined as $\sigma_0 = \frac{n_e e^2}{m_e v_c}$, n_e and m_e represent the number and mass of electrons , e the charge of an electron and v_c the collision frequency between particles. This equation indicates how variations on the magnetic field in a plasma can occur either by motion of the plasma (1^{st} right-hand term) or by magnetic diffusion (2^{nd} right hand term).

Assuming motionless plasma (v=0) then the first term of the equation is dropped, and the equation becomes a magnetic field's diffusion equation, where $D_m = (\sigma_0 \mu_0)^(- 1)$ is referred to as magnetic diffusion coefficient.

$$\frac{\partial \mathbf{B}}{\partial t} = D_m \nabla^2 \mathbf{B} \qquad (2.14)$$

The magnetic field lines tend to diffuse across the plasma under the influence of a finite resistance ($\sigma_0 > 0$) . Magnetic field lines which move through the plasma could meet magnetic field lines from different regions and merge into new magnetic topologies.

The solution for the diffusion equation is obtained by substitution of the vector gradient $\nabla^2 \mathbf{B} = \frac{1}{L_B^2}$, L_B is called the *characteristic length*, and represents the inverse of the vector gradient. The solution of the diffusion equation gives the *magnetic diffusion time* τ_d.

$$B = B_0 e^{\pm \frac{t}{t_d}} \qquad (2.15)$$

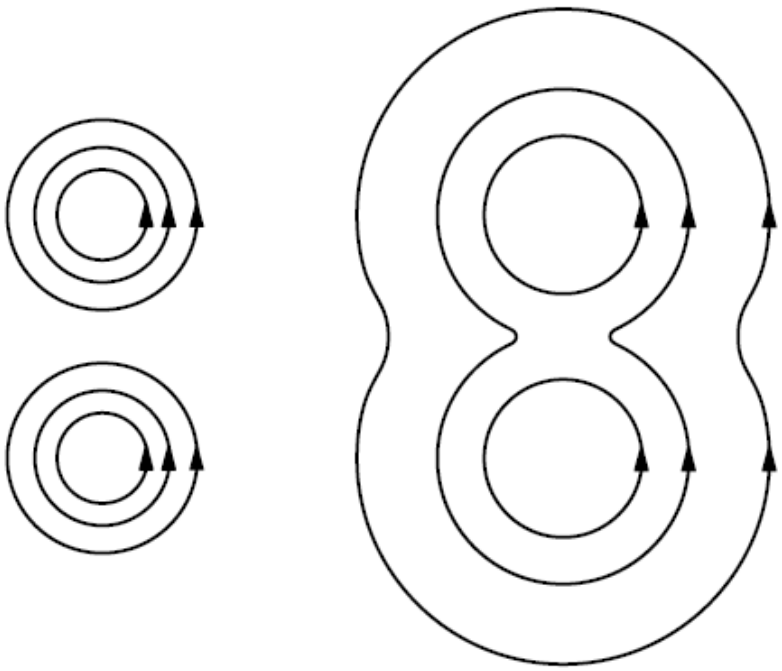

Figure 2.6: Diffusion of two closed magnetic field lines into a new topology[3].

$$\tau_0 = \mu_0 \sigma_0 L_B^2 \tag{2.16}$$

Diffusion will not occur under scenarios where plasma conductivity $\sigma_0 \to \infty$ or the characteristic length L_B becomes too large (magnetic field gradient $\nabla \mathbf{B}$ is small), since the diffusion time τ_d becomes extremely long. This is most likely the situation for most of the geophysical plasmas, where conductivities are high and characteristic lengths are huge, resulting in values of τ_d mostly higher than the age of the object, or even in some cases even higher than the age of the universe itself. Considering the aforementioned, it would make sense to ignore the effect of diffusion in the case of magnetospheric or solar wind plasmas. Nevertheless diffusion plays a role in the E-region of the Ionosphere due to the reduction on the plasma conductivity as a consequence of the high collision frequency, which leads to diffusion times $\tau_d \approx 10^{-9} L_B^2$.

Considering diffusion to be negligible, then the 2^{nd} right-hand term of the equation 2.13 drops off and only the $1st$ right hand term remains. In this case the equation is representing dependency between the variation of the magnetic field and the plasma motion, this dependency is called *frozen-in magnetic flux*.

$$\frac{\partial \mathbf{B}}{\partial t} = \nabla \times (\mathbf{v} \times \mathbf{B}) \tag{2.17}$$

This equation implies that any changes in the magnetic field are such as if the magnetic field lines were constrained to move with the plasma. If two populations of plasma move into

different directions, the magnetic field lines containing this plasma will move according to this motion deforming its original shape.

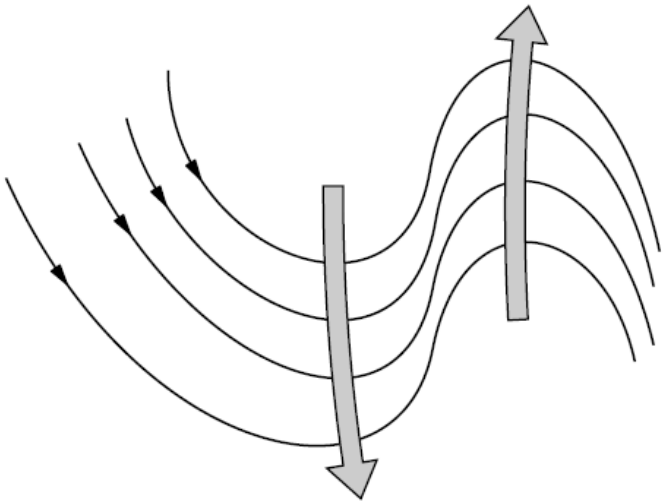

Figure 2.7: Frozen in magnetic flux following the motion of the plasma[3].

If the magnetic field lines are deformated as consequence of plasma motion, then the total magnetic induction of a closed field line will remain unchanged independently of the plasma motion, even if different plasma regions are moving at different velocities. All the field lines which are bounded to the plasma form a volume which is called flux tube. A flux tube is defined by a closed loop surface moving parallel to the magnetic field lines confined in the plasma, and contain a constant amount of magnetic flux. The frozen-in flux concept states that all particles and all magnetic flux contained in a flux tube at a certain instant will stay inside the flux tube at all instants, independent from any motion on the flux tube or any change in the form of its bounding surface*[Baumjohann; Treumann, 1996]*[3]. The relationship between the plasma and the magnetic field lines is analogue to *hydrodynamics*, this is why equation 2.17 is usually called *hydromagnetic theorem* (HMT). The HMT for the frozen-in flux is sometimes expressed as its equivalent in terms of the Electric field **E** from Faraday's law.

$$\mathbf{E} + \mathbf{v} \times \mathbf{B} = 0 \tag{2.18}$$

From this new structure it can be concluded that, for an infinite conducting plasma (no diffusion) the Electric field components aligned with the direction of the plasma motion or the direction of the magnetic field **B** cannot exist, and can only result as consequence of Lorentz's transformations in the direction of the cross product $\mathbf{v} \times \mathbf{B}$.

Another interesting approach to determine the behavior between plasma and magnetic field can be obtained if equation 2.13 is redefined.

$$\frac{B}{\tau} = \frac{VB}{L_B}\frac{B}{\tau_d} \tag{2.19}$$

Here B is the average magnetic field intensity, V represents the average plasma velocity perpendicular to the field, τ denotes the characteristic time of magnetic field variations and L_B is again the characteristic length over which the field varies. The first term defines the convection motion of the field with the plasma, while the second term so does with the diffusion. The ratio between the first and second terms is called the *Magnetic Reynolds number*, which is proportional to the conductivity, velocity and characteristic length.

$$R_m = \mu_0 \sigma_0 L_B V \tag{2.20}$$

Values of R_m indicate if a medium is either diffusion or convection dominated.

- If $R_m \gg 1$ then diffusion in the medium can be neglected and the plasma is frozen in to the field lines. The magnetic field lines move together with the flow.
- If $R_m \approx 1$ diffusion becomes important and the plasma can separate from the magnetic field lines.
- If $R_m \ll 1$ the region is mostly diffusion dominated and the plasma can freely stream through the magnetic field lines without any effect on them.

2.2.1 Magnetic reconnection

The *frozen-in flux* condition ensures that, since magnetic field lines from different regions don't merge into new ones due to the absence of magnetic diffusion, plasma from those two different regions cannot be mixed. Nevertheless, under some conditions, the *frozen-in* concept is violated, plasma from different sources can be mixed, and magnetic field lines can change its topology due to magnetic diffusion. The rearrangement of the magnetic field lines to form new ones with mixed plasma from two different populations is known as **magnetic reconnection**.

The violation of the *frozen-in* flux condition can be understood if the complete expression of the generalized Ohm's law *[Baumjohann; Treumann, 1996]*[3], *[Shay.et.al, 2001]*[5] is analyzed. The complete version includes additionally to the resistive term $\frac{1}{\sigma}\mathbf{j}$,the Hall or Lorentz force term $\frac{1}{n_e}\mathbf{j} \times \mathbf{B}$, an electron pressure gradient term, and a term considering the variation of the current density.

$$\mathbf{E} + \mathbf{v} \times \mathbf{B} = \frac{1}{\sigma}\mathbf{j} + \frac{1}{n_e}\mathbf{j} \times \mathbf{B} - \frac{1}{n_e}\nabla \mathbf{P_e} + \frac{m_e}{n_e}\frac{\partial \mathbf{j}}{\partial x} \tag{2.21}$$

The influence of the additional terms is insignificant in cases where weak, slow varying currents and vanishing pressure gradients are present, therefore the generalized Ohm's law was previously shown in a simplified version in Equation 2.10. Nevertheless, in current sheets such as the neutral sheet or the magnetopause, those terms cannot be neglected and the frozen-in flux concept does not hold anymore, thus originating merging of the magnetic field lines.

It is common to encounter close to current sheets such as the magnetopause or the neutral sheet on the magnetotail, a scenario where two frozen-in magnetic field lines are antiparallel as shown in Figure 2.8. If the magnetic field lines stay motionless and don't approach to the current sheet, this situation could be stable over long periods. However, if the lines approach

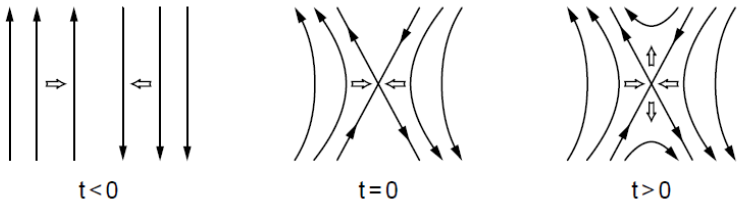

Figure 2.8: Merging of the magnetic field lines[3]

to the current sheet, the *frozen-in* condition will be broken due to the current density carried by the current sheet and diffusion will allow the field lines to merge into new ones. Another interpretation for the violation of the *frozen-in* condition is a decrease of the *Reynolds number* to values of $R_E \approx 1$. The change on RE is caused by anomalous collisions originated by the interaction of the plasma particles with the electric field fluctuations present on the current sheet. The *plasma frequency* v_c regarding the collisionless plasma has to be replaced by an *anomalous collision frequency* v_{an}, which is higher, thus reducing the plasma conductivity and consequently the *magnetic diffusion time* τ_d. When this situation happens even in a small region of space, the magnetic field lines may vanish in a central point called *neutral point* due to diffusion and magnetic reconnection. The X-shaped topology adopted by the field lines while merging can be seen in Figure 2.9, the field lines crossing the neutral point forming the X are called the *separatrix* and this particular magnetic topology is called an *X-line*.

For the case of magnetic reconnection in the magnetotail, antiparallel magnetic field lines and plasma from the lobes are transported due to diffusion from the upper and the southern hemispehere to the neutral point, located in the current sheet. As they reach the neutral point, the antiparallel field lines split and recombine itself with the ones of the other side, generating new magnetic field lines with a population of plasma which is a mixture of those from the original magnetic field lines.

Nevertheless, the situation previously described considers an inflow of plasma into the X-line from the upper and southern hemisphere, but no outflow is considered. If a steady state is assumed $\left(\frac{\partial}{\partial t} = 0\right)$ then due to Faraday's law a spatially uniform Electric field $\mathbf{E_y}$ is needed, since for the x component $\left(\frac{\partial}{\partial t} = 0\right)$ and so the equation holds

$$-\nabla \times \mathbf{E} = \frac{\partial \mathbf{B}}{\partial t} = 0 \tag{2.22}$$

This electric field in the plane of the current sheet drives flow inwards from the upper and lower sides of the X-line, while it expels it to the Earthward and tailward side as it is shown in figure 2.9. The region surrounding the neutral point is called the *diffusion region*. It is there where the MHD approach collapses and diffusion becomes important, thus originating magnetic reconnection and therefore generating new magnetic field lines with mixed plasma from the former field lines. The diffusion region is rather small, but the new reconnected magnetic field lines are partially contained inside this region as they are created*[Rott, 2010]*[2].

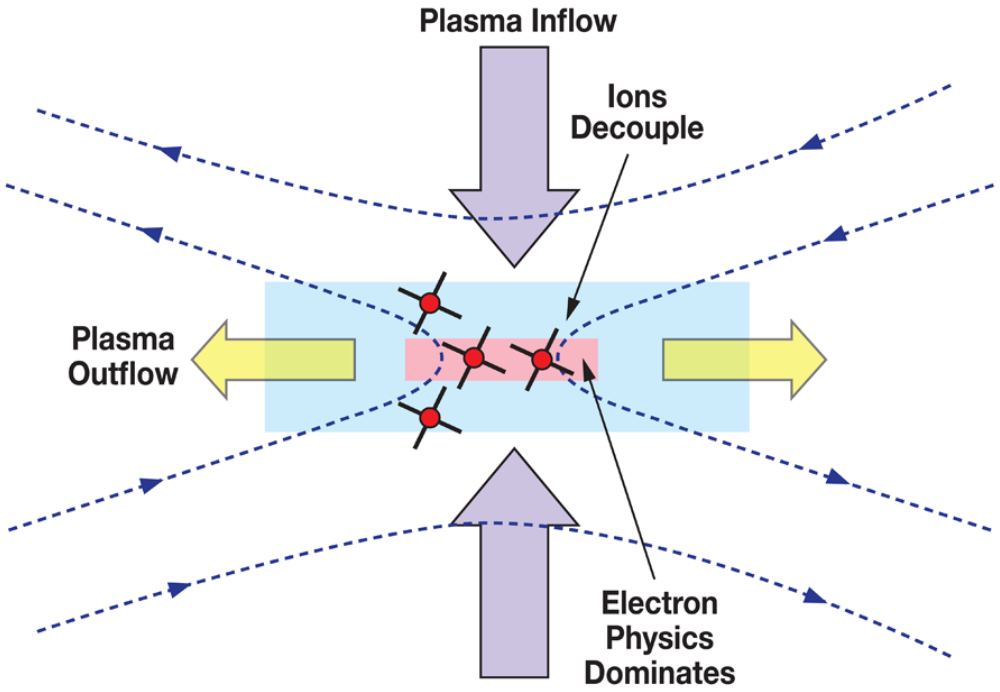

Figure 2.9: Merging of the magnetic field lines[29]

2.3 Magnetospheric convection

In the previous section it was discussed how the merging of the magnetic field lines when the frozen-in condition is broken down allows plasma from different regions to be mixed. This phenomenon is of great interest to understand the interaction between the solar wind and the magnetosphere.

Under certain conditions, the IMF of the solar wind can merge with the magnetic field lines of the magnetosphere at the dayside, thus creating a couple of open field lines containing a plasma population which is a mixture of the solar wind and magnetospheric plasma. These new field lines possess a noon toward midnight directed motion and so they are slowly directed to the tail, adding up to the lobes on the nightside. Field lines from the lobes then generate a second reconnection, creating a closed magnetic field line on the magnetotail and an IMF which continues its path away from the Earth. This whole process is called convection cycle, and it constantly renews the plasma contained in the magnetosphereas solar wind plasma existing on the magnetic field lines due to reconnection is transported into the magnetosphere.

The *flux tubes* originally stemming from the solar wind moving with a velocity v_{SW} have no local electric field present due to its for practical purposes infinite conductivity. However, due to the *Lorentz transformation*, an Electric field would be sensed from the Earth's stagnant reference frame $\mathbf{E} = -\mathbf{v_c} \times \mathbf{B}$.This electric field is referred to as *convection electric field*, it

is down-to-dusk directed and it plays a role in the whole convection cycle which transports plasma between different regions of the magnetosphere.

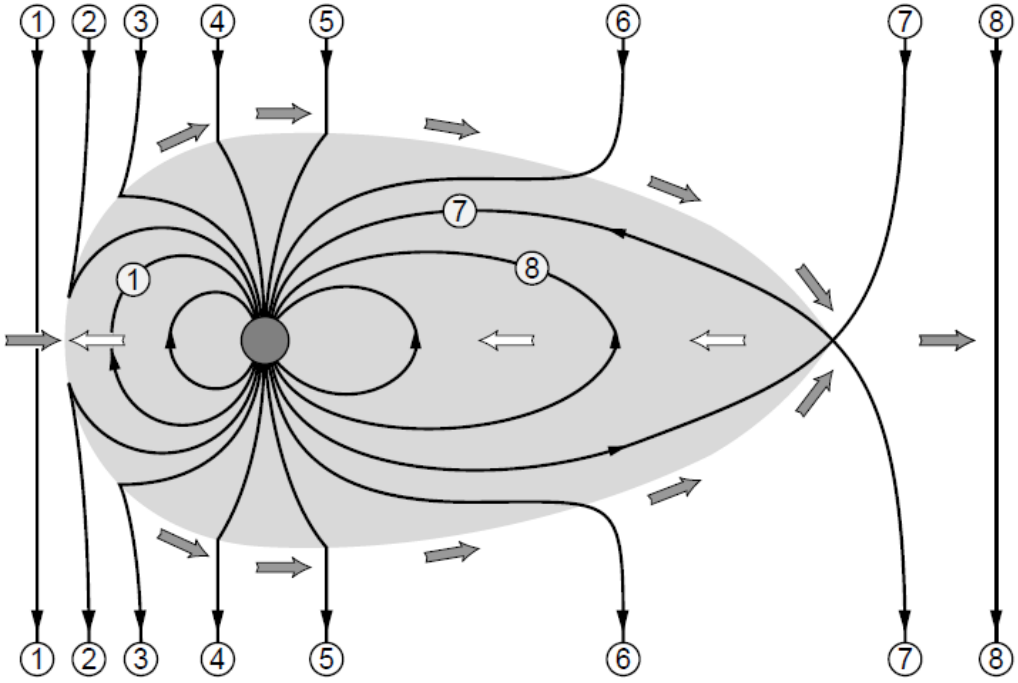

Figure 2.10: Sketch of the convection cycle on the magnetosphere[3]

If a scenario where the IMF lines are north to south directed, the magnetospheric field lines are northward directed and both antiparallel field lines approach the magnetopause, magnetic reconnection can occur and the field lines could merge forming new ones. This situation can be observed in figure 2.10. Here the antiparallel magnetic field lines represented as 1 corresponding to the IMF and the dayside magnetosphere respectively reconnect close to the magnetopause, thus originating two new different field lines which are represented as 2. Each one of those new field lines has one end connected to the Earth on the polar caps, and the other to the solar wind. The solar wind transports the magnetic field lines to the tail across the polar caps, therefore the part of the field line enclosed in the magnetosphere will be carried down the tail, as can be appreciated in the positions 3 to 6. When the two open field lines reach the end of the magnetosphere at 7, the field lines from both lobes merge again. After magnetic reconnection takes place, two new magnetic field lines, one closed, stretched magnetic field line inside the magnetosphere and an IMF line which moves away from the Earth, this is represented as 8. Afterwards, the magnetic tension accumulated in the closed field lines is slowly released, shortening its length and transporting the plasma, which is once again *frozen-in*, along the tail towards the Earth. Finally the cycle closes itself when this magnetic field line is again back to the dayside magnetosphere, so that the magnetic field at the dayside is not depleted in case of high reconnection rate. This whole process represents how plasma from the solar wind and the dayside magnetosphere convects along the tail back

to the earth, thus being the plasma inside the magnetosphere constantly renewed by the convection cycle*[Baumjohann; Treumann, 1996]*[3].

Dayside and nightside reconnection does not occur are singular points, but rather do in lines which can be considered perpendicular to the plane shown on 2.10. Due to its magnetic topology, these lines are called *X-lines*.

2.3.1 Magnetospheric substorms

Magnetic reconnection in the day and nightside are connected, although the whole convection cycle is in reality not stationary. On the one hand, reconnection rate on the dayside depends of the existence of a southwards directed component of the IMF, which varies highly, therefore in periods of northwards directed IMF, no reconnection in the frontside occurs.

On the other hand, all the magnetic flux transported to the tail has to be reconnected and brought back again to the dayside magnetosphere. This process does not need to occur simultaneous to the dayside reconnection and the *reconnection rates* may differ, since only the average rates must coincide. The magnetic field lines which are not reconnected remain in the lobes and add itself to the existing ones, increasing the magnetic flux density in the region. After some time, the magnetic field lines reconnect in the tail and all the accumulated magnetic flux is suddenly released. This explosive energy release is referred to as *magnetic substorm*.Substorms affect the magnetospheric plasma and are responsible of phenomena like the aurora or Ionospheric currents, the process consists on several phases.

Substorm growth: This is the first phase and is triggered as the reconnection rate on the dayside is enhanced. The magnetic field lines originated from reconnection travel down the tail and some of them originate reconnection on the tail, the rest are added to the lobes and increase the magnetic flux density. The magnetic flux density on the lobes and the currents circulating on the current sheet are related through the Biot Savart's law *[Baumjohann; Treumann, 1996]*[3], an increase in the magnetic flux will lead to higher neutral sheet currents which will at the same time pull the field lines of the lobes to the center. After a period of time of about one hour, magnetic field lines start to become unstable and need to release the excess of energy, which leads to the next phase.

Substorm onset and expansion: When the magnetic field lines of the lobes become unstable, an explosive magnetic reconnection takes place in the magnetotail which is referred to as *substorm onset* and indicates the beginning of the *expansion phase*. During the expansion phase, dramatic effects occur in the magnetosphere and aural zone ionosphere, the ionospheric current flow is strongly enhanced and the stretched magnetic field in the plasma sheet becomes more dipolar, it lasts between 30 and 60 minutes. The increase of this dipolar magnetic field is caused by the appearance of a new magnetic topology. A second neutral line called *Near Earth Neutral Line (NENL)* at around 30 R_E is originated and it forms a closed loop of magnetic field with the original *Distant Neutral Line (DNL)* at about 100-200 R_E. This newly formed magnetic structure is called a *plasmoid* and can be seen in the second sketch of Figure 2.11. Its field lines are neither connected to the magnetospheric nor to the IMF, but rather form closed loops which encloses hot plasma from the plasma sheet. In the case the magnetic field of the plasmoid has down-dusk orientation,

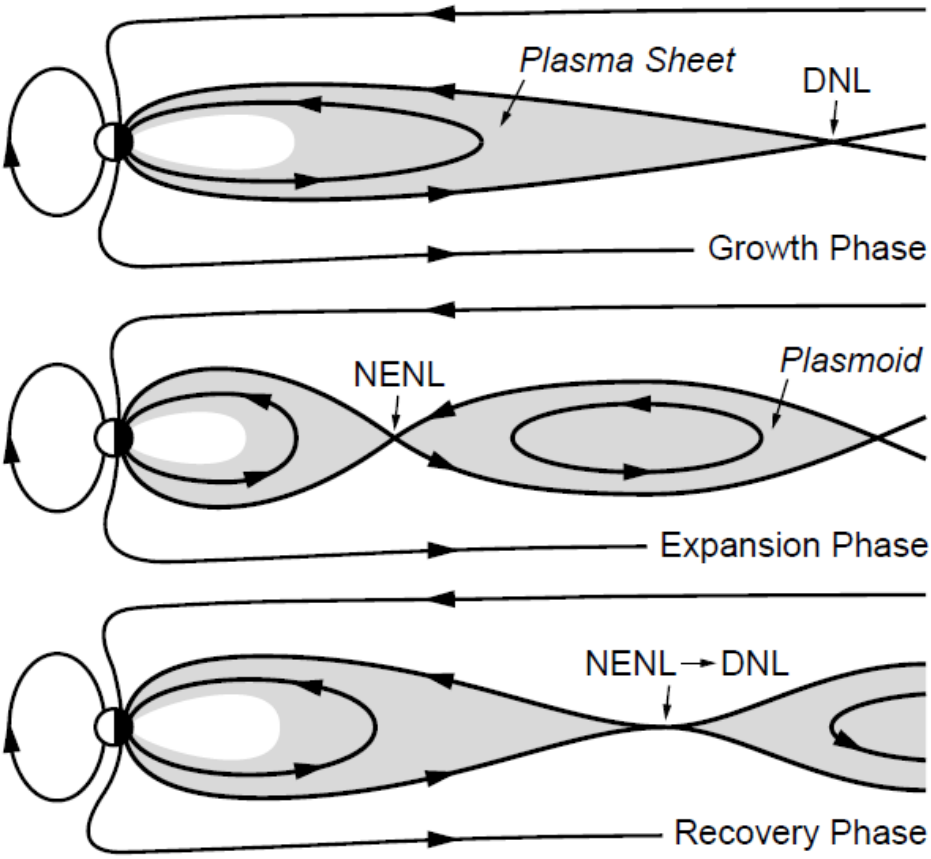

Figure 2.11: Phases of magnetic substorms[3].

the field lines will present a 3D helical magnetic structure instead of a *2-D* closed magnetic loop.

Substorm recovery: The last phase of the substorm begins when the ionospheric currents and the dipolar field orientation in the plasma sheet on the tail start to decrease. The substorm activity settles and the *NENL* moves down the tail until it expels the plasmoid out of the magnetosphere and it occupies the position of the *DNL*. The whole process takes about 1-2 hours and finishes when the magnetosphere returns to a quiet state. Nevertheless, since the recovery process is relatively long, superposition of this phase with the beginning of a new substorm can occur, specially for periods of strong southwards directed IMF on the dayside.

In cases where the IMF stays southwards directed during long periods of time, successive substorms can be generated, thus overlapping the effect of one with the previous while it is still in the recovery phase. If this situation persists in time it is called *magnetic storm* and it has strong consequences on the earth magnetosphere, such as the high ionospheric currents or the global scale decrease of magnetic field strength at ground level.

2.4 Magnetic flux ropes

In the previous section it was discussed how the presence of *plasmoids* is related to the substorms originated due to magnetic reconnection in the tail. These plasmoids are looplike magnetic field structures with hot plasma from the plasma sheet trapped inside. Many of these plasmoids exhibit an strong enhancement on an axial magnetic field components, originating a magnetic field in the plasmoid center which usually coincides with the Y direction of the magnetosphere in GSE coordinates. This enhancement corresponding to an axial component is called *core field* and under its influence, the plasmoid presents a helical magnetic structure around the *core field* axis instead of the original looplike structure. This 3-D helically-shaped variant of the plasmoid is called **flux rope** and its core field can in some cases even surpass the amplitude of the ambient lobe magnetic field. The size of the aforementioned structures is more than R_E scale, and they are originated by primary reconnection of the magnetic field lines.

This thesis is thought to study the properties of flux ropes whose size is much smaller than the aforementioned plasmoids. Although the formation mechanism of this family of flux ropes much smaller than R_E is still unknown, there exist several studies which have proven the formation process of the secondary small scale flux ropes within the primary large scale reconnection layer based on simulation results.

Recent kinetic simulations demonstrated that the primary large-scale reconnection process, which would eventually form the global-scale plasmoid (flux rope in 3-D) as shown in figure 2.11, secondarily may produce the smaller scale (electron to ion kinetic/inertial scales) flux ropes within the primary reconnection layer *[Daughton.et.al, 2006]*[6]. The secondary flux ropes may originate in the whole region of the primary reconnection site for the strong guide field case *[Daughton.et.al, 2011]*[7], or in the front region of the reconnection jets for the very weak guide field case]*[Lapenta.et.al 2015]*[8]. Further kinetic simulation studies demonstrated that these small-scale flux ropes can interact with each other and grow as lager ones *[Nakamura. et. al, 2016]*[9]. These results indicate that the size of the flux ropes existing in the magnetotail would widely spread in a range from electron (secondary reconneccted flux ropes) to global scales (for the primary reconnected flux ropes). Several attempts have been made in order to model those *flux ropes*, from analytical to purely theoretical models, leading to advances in the understanding of those structures *[Hesse. et. al, 1998]*[10].

One of the models is the one proposed by *[Borg. et. al, 2012]*[11].This is a *2-D* analytical model, where the flux rope's *Core field* is assumed to be aligned with the y axis, and the rotation of the mentioned helical magnetic field will occur around this axis. This is of course a simplification of what occurs in reality, as the Core field of the flux rope rarely coincides with the direction of the y axis and most likely flux ropes are tilted referring to the y direction. Nevertheless this is assumed, since there are results from previous works which support this model *[Borg. et. al, 2012; Teh. et. al, 2013]* [11, 12]. Notice that the directions refer to the corresponding coordinate system, which uses to be a minimum variance coordinate system.

A set of different possible scenarios in which a spacecraft encounters a flux rope are shown in figure 2.12. The three axis system form a right-handed orthogonal set with the X direction pointing to the earth along the current sheet, and the Y axis with positive down-dusk orientation, being the current sheet contained in the X-Y plane, finally the Z axis completes the orthogonal set, being perpendicular to the current sheet. In the figure, the circular black

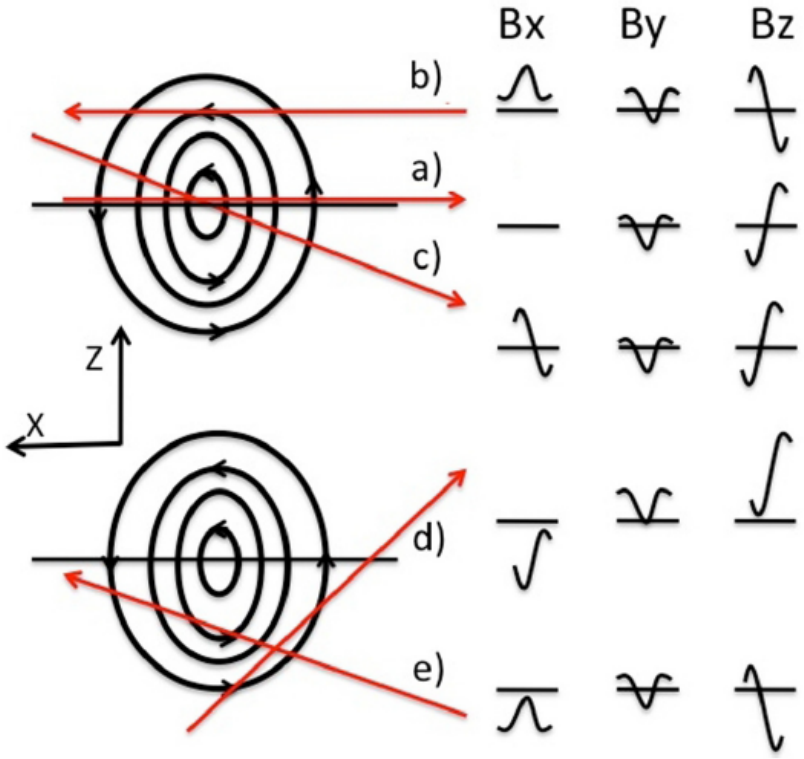

Figure 2.12: Sketch of the model used to identify the existence of flux ropes showing the spacecraft trajectories for several scenarios[11]

lines represent the flux rope, while the horizontal black line represents the current sheet; the red lines represent the trajectories of different hypothetic situations when a crossing between a spacecraft and a flux rope occurs. The shape of the magnetic field components measured by the spacecraft during each hypothetic scenario are shown aside, where can be noticed, the core field of the flux rope $B_{y\,CORE}$ which is parallel to the Y direction is assumed to be negative for this examples, whereas the background B_y is assumed to be positive, the background values of B_x and B_z will be assumed to be 0. Moreover, the rotation of the magnetic field lines should be anti-clockwise, independently of being found on the earthward or tailward side of the X-line, as it should sustain coherency with the polarity of the magnetic field lines' orientation that merge during magnetic reconnection.

On the left side of figure 2.12, five different hypothetic scenarios are considered. The velocity at which a spacecraft moves is some orders of magnitude slower than the velocity at which a flux rope moves, which is related to the Ion outflow velocity parallel to the X direction in the vicinity of an X-line. Under this assumption it can be considered that the spacecraft stays stagnant while a flux rope passes through. A relative movement relative movement consisting in a rectilinear trajectory between flux rope and spacecraft can be considered independent of the moving body, this is shown as red lines in figure 2.12. The five

different scenarios show the following evolution of the magnetic field components:

Scenario a: In this case, the spacecraft crosses the flux exactly at the center of the plasma sheet along the current sheet in the negative X direction, the signature of the B_x component does not experience any variation respect to its corresponding background value, as the spacecraft encounters the magnetic field lines of the flux rope always parallel to the Z direction through its trajectory. With respect to the B_y component, a peak value showing a minimum is detected for the moment when the spacecraft crosses the central point of the flux rope. This is showing how the flux rope core field $B_{y\,CORE}$ assumed to be negative is superposed to the background value of By, which was assumed to be positive, the maximum value of $B_{y\,CORE}$ is detected by the spacecraft in this case, as it crosses the central point of the flux rope. Finally, regarding the signature of the B_z component, a very characteristic symmetric signature can be appreciated. The signature shows first a minimum and then a maximum, going from negative to positive values and finally coming back to the B_z background value after the encounter finishes. The minimum corresponds to the beginning of the encounter, where the magnetic field lines have stronger magnitude and they have pure negative Z direction, whereas the maximum refers to the magnetic field lines at the end of the encounter which are positive Z directed. The central point of the signature between minimum and maximum showing the same background value of B_z as before the encounter occured corresponds to the central point of the X-line, where only core field has an effect and no closed field lines in the X-Z plane are present.

Scenario b: The crossing here takes place in the upper half of the flux rope at some distance parallel to the current sheet in the positive X direction. In this case the B_x component shows a positive value with a local maximum in the signature, which is related to the "half way" of the trajectory, as magnetic field lines here are completely parallel to the X axis and pointing into the positive X direction. On the other hand, the magnetic field lines at the beginning and end of the encounter are Z and X directed, being B_x positive for both cases, thus justifying the positive value of B_x along the whole crossing. Regarding the values of the B_y component, the result is very similar to the one shown in *scenario a*. The B_y signature goes from a positive background value to a negative value at a local minimum, which represents the maximum value of the core field $B_{y\,CORE}$ registered during the crossing. However, the value in this case does not represent the total value of the flux rope's core field, as the intensity of $B_{y\,CORE}$ increases radially approaching to the central point of the flux rope, which was not crossed during this encounter. It would also be important to mention, that if the crossing would have taken place still a bit further away from the current sheet, it could happen the situation where the value of B_y shown in the minimum would still be positive, despite being $B_{y\,CORE}$ negatively directed. Finally, about the B_z component the bipolar signature around the background value is reversed compared to *scenario a*, as the direction of the crossing is also reversed. The component shows a maximum and then a minimum, although the magnitude of the maximum and the minimum should be less than the one in *scenario a*, since magnetic field lines here are not purely Z directed at the beginning and end of the encounter.

Scenario c: In this case the crossing starts on the flux rope's left side of the northern hemisphere and finishes on the right side of the southern hemisphere, the trajectory is negative

X and Z directed. Unlike to the previously commented scenarios, the B_x signature in this case is showing a variation similar to the ones characteristic of the B_z component. This is caused due to the change of hemisphere during the encounter, as magnetic field lines have always a positive B_x component in the northern hemisphere and a negative in the southern, the crossing takes place in this case through the center of the flux rope, so the value of B_x in that point goes back to the background value. The signature of B_z presents in this encounter the same as in *scenario a*, given that the spacecraft crosses the flux rope across its center. The intensity of the B_y component increases radially when approaching the central point of the flux rope independently of the direction due to the helically nature of the flux rope's magnetic field. The maximum value of the core field $B_{y\,CORE}$ is that way reached and superposed to the positive value of B_y background. Finally, the B_z component shows also a very similar shape to *scenario a*, however with higher magnitude in the maximum and minimum values. The magnetic field lines at the beginning and end of the crossing are not only Z directed, but still show the same polarities in the Z direction than *scenario a*, this is why the magnitude of B_z is lower here. Besides, the background value is reached in between the bipolar variation due to the crossing through the flux rope center. Notice that in comparison with *scenario a*, the big difference lies in the distribution of the magnetic energy, as the magnitude registered in the B_z component is now distributed between B_z and B_x.

Scenario d: This situation shows an encounter where the spacecraft crosses the flux rope only through the lower right quadrant. This situation is close to the border of non-detection, as the flux rope is barely seen by the spacecraft. The B_x signature here will show a minimum and then a progressive way back to background Bx, as the crossing starts in a point where the magnetic field lines are almost completely negative X directed, and finishes with nearly pure positive Z directed magnetic field lines where B_x is almost negligible (but still negative). In respect to the B_y component, a variation in this signature will be in this case barely noticed. A small variation of the By component showing a local minimum will be detected, nevertheless this will only represent a small portion of the flux rope's core field $B_{y\,CORE}$, since the crossing occurs too far away from the center of the flux rope along the whole trajectory. Regarding the B_z component, a signature increasing progressively from the background value of B_z to a local maximum and then returning back to the background would be registered in this case, the value will be positive during all the crossing, as only positive values of B_z are detected during the whole trajectory. Based on the signatures registered for this particular case, one can notice this is a very bad type of scenario, in which a flux rope will be very complicated to detect, as the shape of the components are not clearly defined.

Scenario e: This last scenario considers the situation where the spacecraft crosses the flux rope only through the southern hemisphere moving towards positive X direction. In this case, the signature of the measured B_x component will start decreasing until it reaches a local minimum corresponding to the point where the magnetic field lines are completely parallel to the X axis in the negative direction, and then it will go back to the corresponding background value of B_x. Notice that in 2.12, there is a mistake in the shape of the magnetic field component B_x of *scenario e*, as the signature shows a local maximum there instead of a local minimum. The B_y component presents again in this case a minimum superposed on a positive background. The total value of the core field $B_{y\,CORE}$ is not represented in the

measurement, as the spacecraft does not cross the center of the flux rope. In regard to the B_z component, the shape is in this case showing a non-symmetric bipolar variation. Due to the oblique trajectory of the spacecraft across the flux rope, first a small maximum and then a bigger minimum are registered, since the spacecraft encounters almost horizontal magnetic field lines with positive B_z at the beginning, and almost vertical magnetic field lines with negative B_z at the end.

These 5 considered scenarios cover most likely all possible situations that could occur during the crossing between a flux rope and a spacecraft. Only the scenario where a spacecraft would move from the southern to the northern hemisphere (or north to south), while staying always in either the left or the right side of the central point of the flux rope is not considered here. This scenario despite being hypothetically possible, is physically not very realistic, since flux rope's motion is originated due to the ion outflow of an X-line formed during magnetic reconnection, being this directed in the X axis, whereas this scenario suggests a higher velocity of the flux rope in the Z axis than in the X axis.

2.5 Hall Field

When magnetic reconnection occurs an X-shaped magnetic topology called *X-line* is generated. The X-line is characterized by a region called the *separatrix*, which is determined by the magnetic field lines that cross the *neutral point*. Close to the neutral point, there is the so called *diffusion region* where the ions and the electrons decouple from the magnetic field lines and the *frozen-in condition* is violated. Due to magnetic reconnection, stored magnetic energy is converted into kinetic energy close to the X-line. This originates an inflow of ions from the upper and lower sides of the X-line and an outflow parallel to the current sheet directed to the left and right side of the X-line in and out of the diffusion region, as can be seen in 2.14.

Inside the diffusion region, two regions need to be defined, the ion and the electron diffusion region, both regions are shown in figure 2.13 as the grey and yellow areas respectively. Before reaching the diffusion region, electrons and ions are *frozen-in* and move together with the magnetic field lines. As the magnetic field lines penetrate the ion diffusion region, the ions decouple from the field lines due to the violation of the *frozen-in* condition, but not the electrons, whose inertial length is approximately 40 times shorter than the ion inertial length. The electrons remain frozen until they reach the electron diffusion region, located much closer to the central point of the X-line. The differential motion between the magnetized electrons and the unmagnetized ions due to the different decoupling instants originates strong Hall currents opposing the electron flow in the reconnection layer, the electron motion is represented in figure 2.13 with a red dotted line. The electrons remain magnetized until they reach the electron diffusion region, where they also decouple from the field lines. The currents originated by the electron flow pattern create a quadrupolar magnetic field pattern perpendicular to the plane *[Birn et. al, 2001; Nagai et. al, 2001; Pritchett et. al, 2001; Shay et. al, 2001]*[13, 14, 16, 5]. This particular structure of the magnetic field is called the *Hall Field* and is a signature of the *Hall effect [Zweibel et. al, 2016]*[20].

The Hall currents generated flow along the field lines of the separatrix of the different regions opposing the inflow and outflow of particles as shown in figure 2.14 directed inside

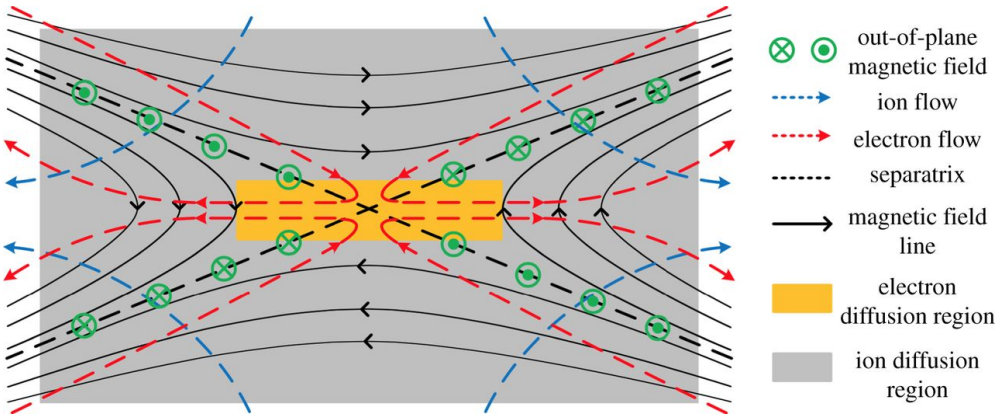

Figure 2.13: Hall field pattern in the vicinity of an X-line inside the diffusion region[20]
.

and outside of the diffusion region, this way generating field aligned currents in the separatrix. On the one hand, the differential electron motion of the inflow from the upper and lower regions of the X-line is compensated by field aligned currents directed away from the X-line neutral point. On the other hand, the current sheet opposing the outflow on the left and right sides of the X-line will travel through the separatrix to the neutral point reaching the diffusion region. In such a way, a field aligned current sheet structure shown in figure 2.14 is generated in the separatrix. *[Birn et. al, 2001; Nagai et. al, 2001; Pritchett et. al, 2001; Zweibel et. al, 2016]*[13, 14, 16, 20].

The double field aligned current sheet structure is antiparallel and can be interpreted as a circulating current sheet around the separatrix *[Nagai et. al, 2003]*[15]. The current carriers are due to the *Faraday's law of induction*, this circular current **I** generates a magnetic field distortion perpendicular to the plane where currents are circulating, the direction is determined by the right hand rule. A very characteristic magnetic field pattern is originated in the separatrix.

The **Hall field** has a quadrupolar topology, since the polarity of the magnetic field is inverted for each of the hemispheres and sides of the X-line due to the circulating Hall currents, as can be seen in figure 2.13 and is considered to be a good indicator of the existence of magnetic reconnection. The magnitude of the quadrupolar Hall field is small, around 16% of the magnetic field magnitude in the lobes, although there are hypothesis that state it could play an important role in the still poorly understood formation of the flux ropes. Influence of the hall field on the flux rope's background magnetic field and core field polarities will be submitted to analysis in this work.

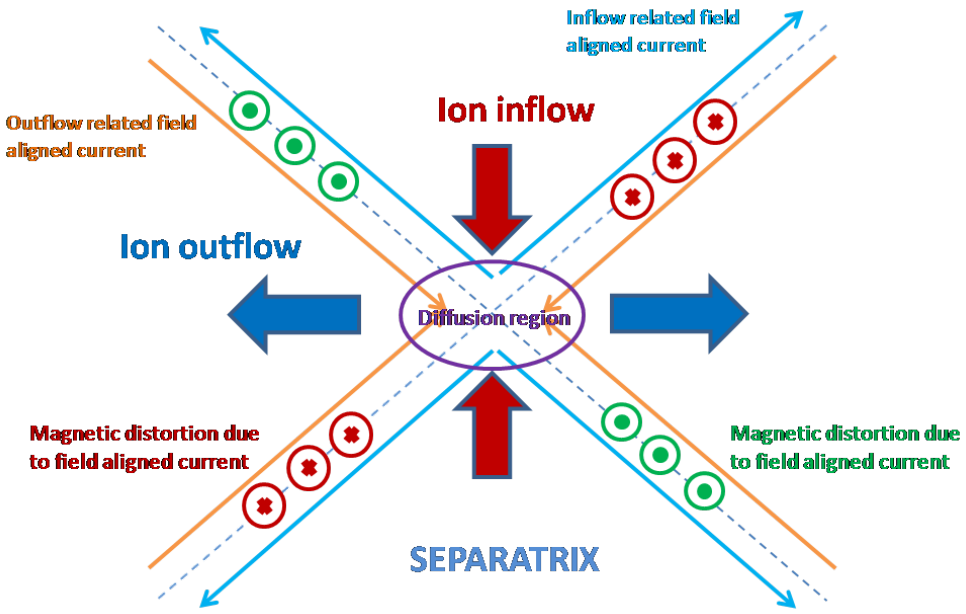

Figure 2.14: Field aligned currents and magnetic distortions in the vicinity of an X-line.

3 The Cluster Mission

The **Cluster Mission** is a multi-spacecraft mission from the *European Space Agency (ESA)* composed of 4 identical spacecrafts that fly in a tetrahedral configuration. The aim of this mission is the study of small-scale structures of the magnetosphere and its environment in three dimensions. A scientific payload composed of eleven instruments is found on-board with the aim of collecting scientific data.

3.1 History of the Cluster mission

The Cluster mission was first proposed in November 1982 in response to an *ESA* Call for Proposals for the next series of science missions. The idea was developed into a proposal to study the *cusp* and the *magnetotail* regions of the Earth's magnetosphere with a polar orbiting mission.The Cluster idea developed into a proposal and then a mission and in 1985 was presented to the scientific community.Sort after in 1986 the ESA Science Program Committee selected included the cluster mission together with the SOHO Mission in the *Solar Terrestrial Science Programm (STSP)*. In 1996, Cluster was ready to be launched.

Cluster was expected to benefit from a 'free' launch on the first test flight of the newly developed Ariane-5 booster. After several minor delays, Ariane-501 lifted off from Kourou, French Guiana on 4 June 1996, carrying its payload of four Cluster satellites. Unfortunately, the launcher's maiden flight lasted just 37 seconds before intense aerodynamic loads resulted in its break up and initiation of the automatic destruct system, as it came off course. Debris from the Cluster spacecraft were scattered across the mangrove swamps near the launch site.

It seemed to all concerned that 10 years of work had come to nothing. However, in July 1996, after considering possible ways of recovering at least some of the unique science from the mission, ESA decided to build a fifth Cluster satellite out of the spare parts of the experiments and subsystems of the old cluster mission. This spacecraft was to be identical to the original Cluster spacecraft and so it was appropriately baptized as *Phoenix*, referring to the mythical bird which was reborn by rising from its own ashes. By taking advantage of the existing hardware, together with the knowledge and experience gained in the original program, Phoenix was expected to be fully integrated and tested by mid-1997, opening the way for a launch later that year. This rapid response to the launch failure soon gave way to a longer term strategy.

An awareness that the scientific objectives of the Cluster mission could not be met by a single spacecraft led to proposals to rebuild three or four full-size Cluster spacecraft alongside Phoenix. These proposals had significant implications for an ESA science budget that was already fully committed, nevertheless it was considered that the costs of a full rebuilding program would be much lower, since the spacecraft had already been through a complete cycle of design, development and testing.

As the Ariane-5 was considered too expensive to meet the stringent cost cap imposed by the *Science Programme Comitee (SPC)*, Arianespace suggested looking at the possibility of using the Russian Soyuz rocket to launch the spacecraft. The Soyuz Rockets were recently started to being marketed by the newly created Starsem, a European-Russian venture between Aerospatiale, Arianespace, the Russian Space Agency and Samara Space Center. In view of this new launch option, the SPC was asked exceptionally to delay the decision by four weeks, in order to make a preliminary study on the launch with Soyuz. The results obtained from this preliminary study showed that the performance of Soyuz were perfect for Cluster II. On 3 April 1997, the recovery mission of the initial Cluster program was approved by the SPC.The contract to provide four Cluster II spacecraft was signed on 28 November 1997, with the Prime Contractor Daimler Benz Aerospace (Dornier), Germany and the contract for the launch was signed with Starsemon 24 July 1998.

The launch was realized in two phases, each of them corresponding to the launch of a Soyuz Rocket. The first Soyuz carrying two of the cluster Spacecraft was launched on 16^{th} July 2000 from the Baikonur Cosmodrome, Kasakhstan. However, the Cluster mission had to wait until the 9^{th} of August 2000 to be completely arisen from its ashes, when the second Soyuz Rocket carrying the remnant cluster spacecraft was launched. So was Cluster mission back on track as initially planned, just with a few years of delay regarding the original schedule [?].

3.2 Scientific objectives and characteristics of the Cluster mission

The main goal for which the Cluster mission was designed is to develop a study of the small-scale plasma structures in the key plasma regions, those are the *Bow shock and the Solar wind*, *Magnetopause*, *Polar Cusp*, *Magnetotail* and the *Auroral zone*.

The measurements obtained by the four spacecraft represent a 3-dimensional space-time analysis of the key regions. Shape and size of smallscale-plasma structures existing in the key regions, as well as its time evolution can be observed by proper analysis of the data. In this work, measurements of the cluster spacecraft during orbital crossing of the magnetotail are used for the detection of existing flux ropes inside this region.

In order to match the scientific objectives of the mission an inertially fixed, highly elliptical polar orbit (90° inclination) was chosen with a perigee at 4 Earth-radius (R_E) and apogee at 19.6 R_E, the orbital period is 57 hours.The cluster spacecraft are positioned in this final orbit after a sequence of previous orbits. After launch of the Soyuz rocket and separation of the rocket's nose module carrying two of the Cluster spacecraft, they are positioned in a low-Earth orbit for a short time. The main engine of the module is then started and an intermediate elliptical orbit with an inclination of 64.9° is achieved. Finally, after a smooth roll to stabilize the spacecraft during its release, the two spacecraft separate from the module. The spacecraft are then carried after a series of complex maneuvers which last around 3 weeks to the desired elliptical polar orbits. The spacecrafts are spin-stabilized while already in orbit. The same sequence is realized for each pair of cluster spacecraft.

The initial orbit for the operational cluster mission will be in the dawn-dusk meridian with the apogee at dusk. Then due to rotation around the Sun and the fact that the orbit is inertially fixed, the apogee will be in the solar wind after 3 months, around the flank of the magnetosphere at dawn after 6 months, in the plasma sheet around midnight local time after

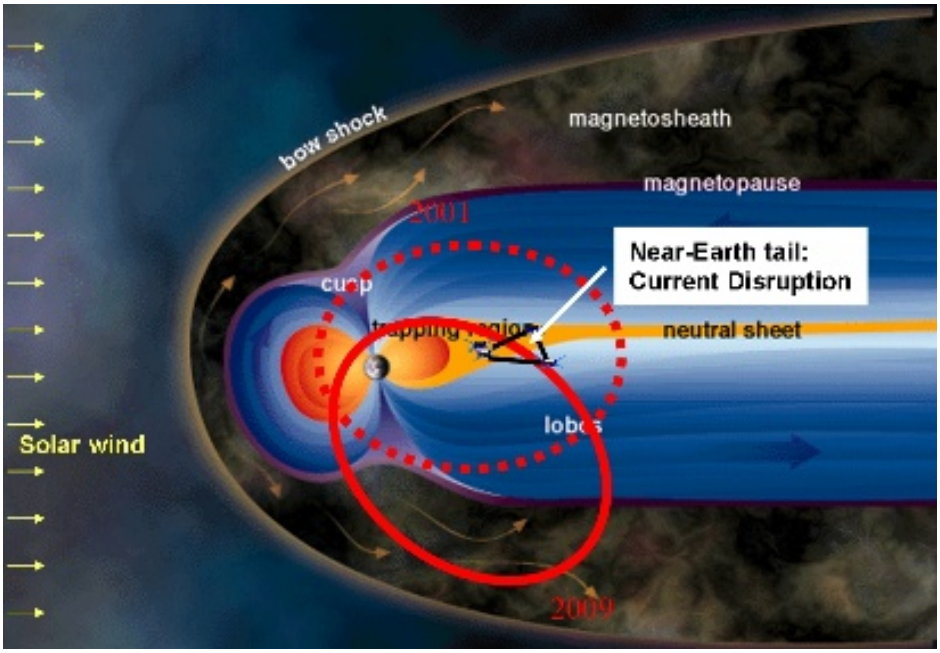

Figure 3.1: Highly elliptical polar orbits of the cluster mission for 2001 (early stages of the cluster mission, 9 months after launch) and 2009[21]

9 months (Figure 3.1) and again at the initial point after one complete year of the mission. This orbit was identically maintained for the first 4 years of mission. After this period, new positions of the orbit referring to the ecliptic plane were studied, as shown in Figure 3.1. The perigee, apogee and inclination of those new orbits are identical to the initial ones and they will prevail during the whole life of the mission.

The four Cluster spacecraft orbit around the Earth in a tetrahedral configuration as shown in Figure 3.2. Initially, all inter-spacecraft distances were meant to be equal, forming a regular tetrahedron. The scale of the tetrahedron was changed during each tail season but still a regular tetrahedron configuration was being used. It was not until 2005, when a change of strategy took place, and a multi-scale configuration was established. In this configuration, spacecraft 1, 2 and 3 have same inter-spacecraft distances, while spacecraft 3 and 4 are separated by a distance some orders of magnitude smaller in the normal direction of the plane comprehended by spacecraft 1 to 3. In 2006, the spacecraft were one more time configured as a regular tetrahedron, with inter-spacecraft separation of 10000 Km. The multi-scale configuration was readopted from 2007 to nowadays, as is was considered to be a better strategy in order to find connections between phenomena occurring at different spatial scales.

The up to date inter-spacecraft distance evolution is shown in Figure 3.3, were periods using either regular tetrahedron or multi-scale configuration are clearly distinguishable. It can be appreciated, that a wide range of different inter-spacecraft separations were configured during the whole lifetime of the cluster mission, especially in the case of multi-scale configuration. Among this configuration, the separation between spacecrafts 3 and 4 reached

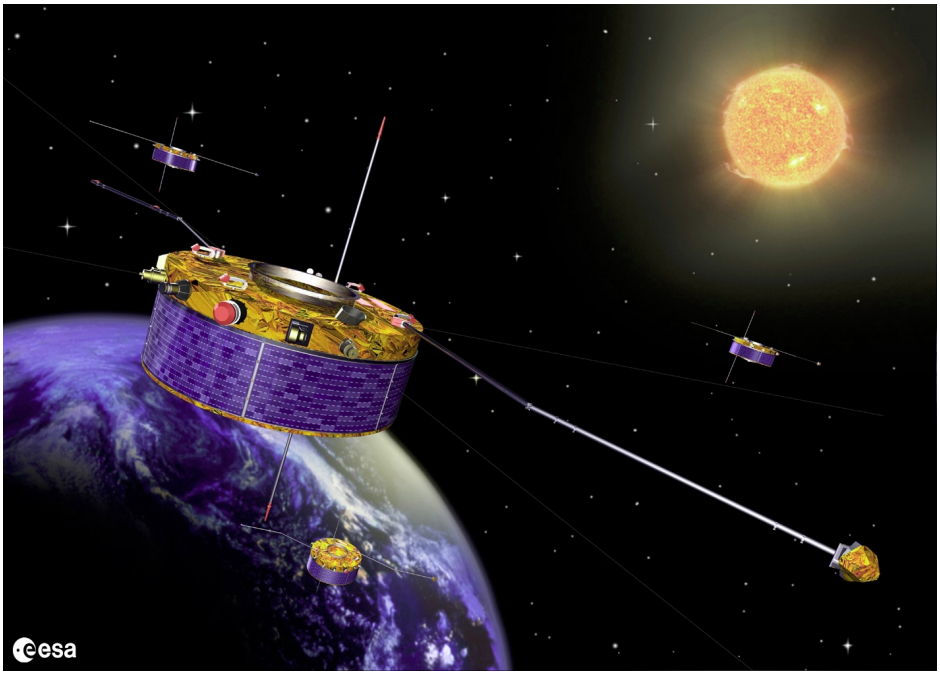

Figure 3.2: Tetrahedral configuration of the four Cluster spacecrafts orbiting around the earth[21].

even values of less than 100 Km, or even 10 Km in the most recent years of the mission. The inter-spacecraft distances are normally modified every six months, as it coincides with the moment where proper crossings of the tail and the cusp occur.

3.3 Cluster spacecraft characteristics

The cluster spacecraft has a cylindrical design with dimension of 1.3 m high and 2.9 m diameter, the appearance of the spacecraft is shown in Figure 3.4. This shape is driven by the implementation of a body-mounted solar array and also by the optimization of the fields of view available to the experiments located on the main equipment platform, which is located on the upper side of the spacecraft. The spacecraft is spin-stabilized, rotating at 15 rpm in nominal configuration.

3.3.1 Structure and Subsystems

The compact structure of the Cluster spacecraft consists on many differentiated sub-structures:

- **The central cylinder:** accommodates the solar-array panels and the MEP
- **The Main Equipment Plattform (MEP):** All experiments are allocated.
- **Tank support structure:** Six tank propellants are carried with about 1180 Kg of propellant.

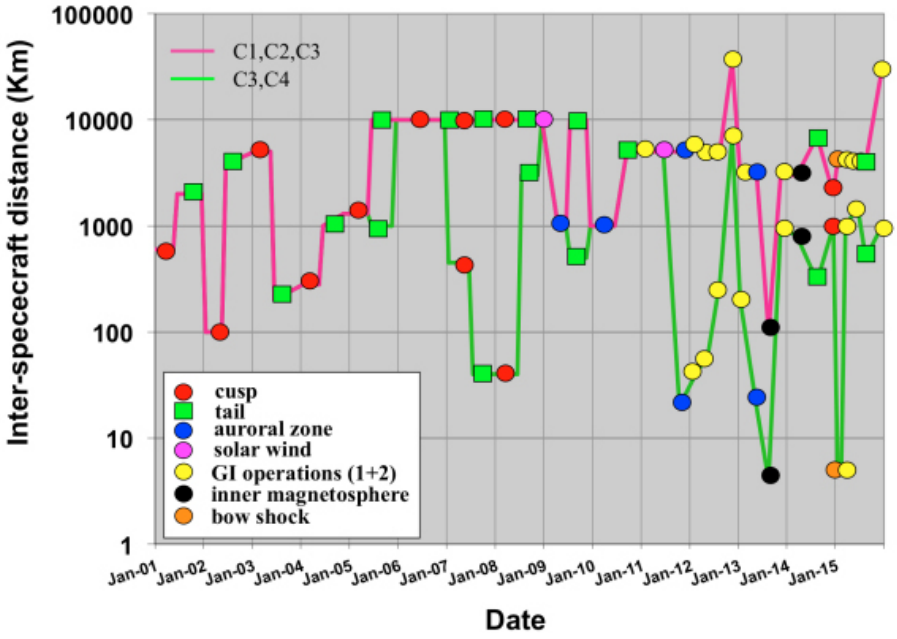

Figure 3.3: Evolution of the inter-spacecraft distances since the beginning of the Cluster mission to nowadays[21].

- **Platform internal to central cylinder:** Supports the single main engine.
- **Reaction Control System (RCS) support ring:** Four radial 10 Newton thrusters are allocated.

Additionally to the structural design, many other important aspects should be defined for the proper operation of the spacecraft once this is set in orbit. Several subsystems correspond to the design of those[1]:

Propulsion Design: The *Reaction Control Subsystem (RCS)* defines the propulsion design of the spacecraft. It is configured as a conventional bi-propellant system based on a single 400 N main engine and eight 10 N thrusters. The propellant is stored in the six tanks pressurized by Helium stored in two smaller spherical tanks.

Thermal Design: The passive thermal control of the Cluster Spacecraft is based on a low-emisivity concept, insulating the spacecraft from the exterior environment enough to survive the eclipses while still allowing the internally generated heat to be rejected. An *Optical Surface Reflector (OSR)* radiator is integrated in the top surface to allow high dissipation of the RF amplifiers. An *external Power Dumper (EPD)* radiator located within the central cylinder dissipates excess power generated by the solar arrays. Heaters are used to keep equipment within specified temperature ranges throughout all the mission, including eclipses.

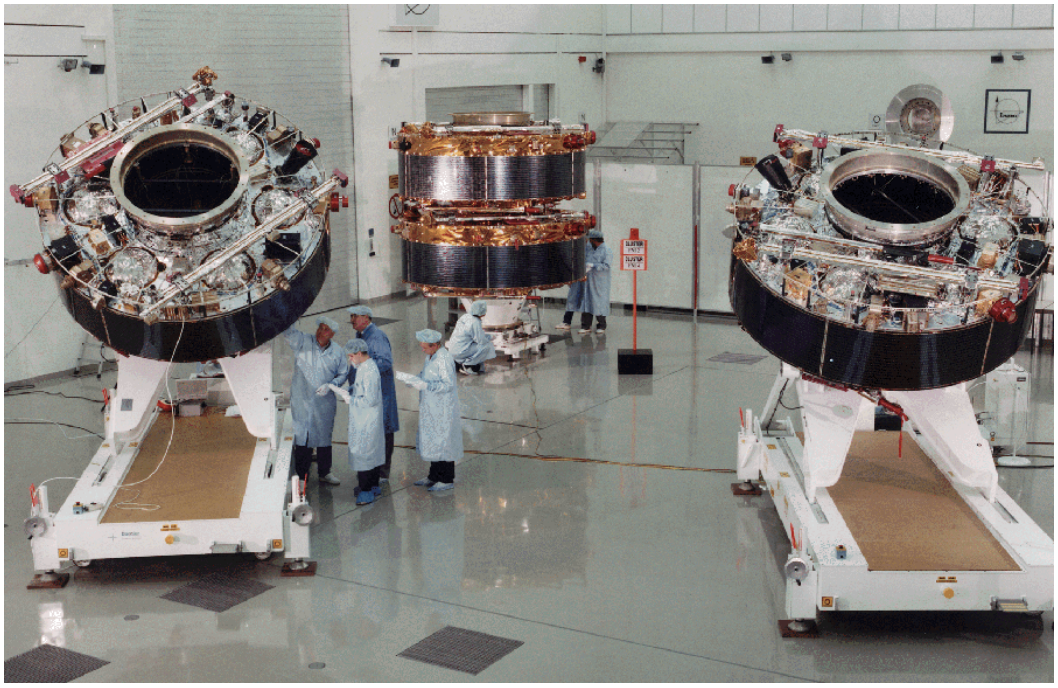

Figure 3.4: All four Cluster spacecraft before launch was committed [22].

Electrical Design: The electrical design of the spacecraft consist in four big functional areas:

- **Power supply subsystem:** power demands will be met by the body-mounted solar array and five silver/cadmium batteries. The batteries will fed the spacecraft during eclipses and support the solar array during periods of peak power demand. Full protection against short-circuit or overload is provided by limiting the maximum current in any supply line. Excess solar-array output power is routed to Internal or External Power Dumpers.

- **On Board Data Handling (OBDH) Subsystem:** Performs the primary spacecraft control functions. Consists on a *Central Data Management Unit (CDMU)*, a *Remote Terminal Unit (RTU)* and two *Solid-State Recorders (SSRs)*. The OBDH decodes and distributes commands received by the telecommunication subsystem and acquires and encodes telemetry from payload and subsystem units. Telemetry goes then to the telecommunications subsystem for real time transmission, or to the SSRs for later transmission. It also provides timing and synchronization signals to payload and subsystem units, as well as AOCMS data to the payload.

- **Attitude and Orbit Control and Measurement (AOCMS) Subsystem:** Performs the attitude and orbit of the spacecraft. Spacecraft attitude and spin rate are provided by a star mapper and a X-beam Sun sensor. Orbit and attitude maintenance is performed by using control thrusters together with the main engine, used to perform

the large orbital manouvers.

- **Telecommunications Subsystem:** Uplink and downlink capabilities of the spacecraft are included in this subsystem. It supports the telecommand, telemetry and tracking functions. Connects with the ESA ground segment and the NASA Deep-Space Network at S-Band frequencies (Uplink 2025-2110 MHz; Downlink 2200-2290 MHz). Consists of three low-gain antennas, a transponder set with redundancy and a 10 W HPA amplifier, and a RF distribution unit between the three low-gain antennas. Two of the low-gain antennas are mounted on deployable booms attached to upper and lower faces of the spacecraft to ensure spherical coverage for uplink and hemispherical for the downlink.

3.3.2 Instrumentation

To accomplish the objectives for which the Cluster mission was realized, several experiments are carried out by the spacecraft, constantly gathering data during its orbit. Each of those experiments is realized by a specific instrument mounted in the MEP[1]:

Flux Gate Magnetometer (FGM): Main instrument for the magnetic field investigation experiment that measures the magnetic field vector. Two FGM are mounted in each spacecraft together with an on-board *Data-Processing unit (DPU)* to conform the whole structure of the experiment. The FGM measures the value of the magnetic field components correspondent to its 3 local axis, as well as the absolute value of the magnetic field. The data obtained from the DPU represents the magnetic field vector data in GSE coordinates. Different resolutions of the data are available for this experiment. The lowest is the spin resolution, corresponding to a sampling rate of $T_s = 4$ s, which represents the time that the spacecraft needs to spin around completely at the spin velocity of 15 rpm determined by the spin-stabilization. On the other hand, also full resolution at a sampling frequency of approximately $f_s = 22$ Hz with corresponding sampling rate of $T_s = 0.0454$ s is available.

Cluster Ion Spectrometry (CIS) Experiment: The CIS experiment is a comprehensive ionic plasma spectrometry package capable of obtaining full three-dimensional ion distributions with resolution of one spacecraft spin with mass per charge composition determination. The CIS package consists of two different instruments, the *Hot Ion Analyzer (HIA)* and a time-of-flight *ion COmposition and DIstribution Function analyser (CODIF)*, an additional on-board *Data Processing Sytem (DPS)* completes the package. Both analyzers use symmetric optics resulting in continuous, uniform and well characterized phase space coverage.

- **CODIF:** Consists on a high sensitivity mass resolving spectrometer with an instantaneous $360° \times 8°$ field of view to measure full 3D distribution functions of the major ion species, to wit H^+, He^{++},He^{++},O^+ within one spacecraft spin. The sensor primarily covers the energy range between 0.02 and 0.04 KeV/charge. To cover the large dynamic range required for accurate measurements in the low-density plasma located at the magnetotail on the one hand and the dense plasma in the magnetosheath-cusp boundary layer on the other, two different sensitivities on the time-of-flight system have to be employed. The time-of flight system measures the velocity of an Ion by the time that it

needs to travel the 3 cm distance between a carbon foil and the surface of the "stop" microchannel plate (MCP). The minimum number of counts in a distribution needed for computing the basic plasma parameters is about 100.

- **HIA:** This instrument combines the selection of incoming ions according to the ion energy per charge ratio by electrostatic deflection in a symmetrical quadrispherical analyser which has a uniform angle-energy response with a fast imaging particle detection system. The quadrispherical electrostatic analyzer consists on a uniform 360° disc-shaped field of view (FOV) and extremely narrow angular resolution capability. The HIA instrument has $2 \times 180°$ FOV sections parallel to the spin axis with two different sensitivities which are referred to as *low g* and *High G*. On the one hand,the *low g* is characterized by a high angular resolution of 5.625° on the 8 central nodes, while the remnant 8 sectors have an angular resolution of 11.25°, the remaining 45° to complete the 180° degree of the section consist on two blank 22.5° sections allocated on the sides, this sensitivity allows the detection of solar wind. On the other hand, the *high G* section of 180° is divided into 16 anodes each of them with an angular resolution of 11.25°. For each sensitivity section, a full 4π steradian scan is completed every complete spin of the spacecraft giving a full 3-D distribution of ions in the energy range from about $5\frac{eV}{e}$ to $32\frac{KeV}{e}$. So can the basic plasma parameters be computed.

The Wave Experiment Consortium (WEC): The WEC was stablished as a way to put together all the results obtained from the experiments *STAFF*, *EFW*, *WHISPER*, *WBD* and *DWP*, dedicated to the analysis of field and wave experiments, in order to get the maximum scientific return from the available resources.

- **STAFF:** The *Spatio-Temporal Analysis of Field Fluctuations (STAFF)* experiment measures the fluctuations corresponding to electromagnetic fields. Consists of a three-axis search coil magnetometer and a spectrum analyzer.

- **EFW:** The *Electric Field and Wave (EFW)* experiment Designed to measure quasi-static electric field, measurements over short periods of time of up to five simultaneous 4 KHz bandwidth waveforms (2 electric and 3 magnetic), and plasma density fluctuations.

- **WHISPER:** *Waves of HIgh frequency and Sounder for Probing of Electron density by Relaxation (WHISPER)* is designed to provide an absolute measurement of the total plasma density. This is achieved by means of a resonance sounding technique which measures the total electron density and the subsequent resonances of the local plasma.

- **WBD:** The *Cluster Wide-Band (WBD) Plasma Wave* is designed to provide very high-resolution frequency-time measurements of plasma waves in the Earth's magnetosphere. It consists of a digital wide-band receiver that can provide electric or magnetic-field waveforms.

- **DWP:** The Digital Wave Processing (DWP) is responsible for the coordination of the WEC operations at several levels.

Electron Drift Instrument (EDI): Measures the drift of a weak beam of test electrons that, when emitted in certain directions, return to the spacecraft after one or more gyrations.

The drift is related to the electric field and the magnetic field gradient.

Active Spacecraft POtential Control (ASPOC): Designed to ensure proper measurements of the ambient plasma distribution functions (by PEACE or CIS) by maintaining the electrostatic potential of spacecraft with respect to plasma at a low level.

Plasma Electron And Current Experiment (PEACE): An electron analyser which measures the three dimensional velocity distribution of electrons. The instrument consists on two parts. One of them measures faster electrons, the *High Energy Electron Analyzer (HEEA)* while the other does the same with the slower, the *Low Energy Electron Analyzer (LEEA)*.

Research with Adaptive Particle Imaging Detectors (RAPID): An advanced particle detector which records the highest energy electrons and ions which enter it from space. It is composed by two spectrometers, the Imaging *Ion Mass Spectrometer (IIMS)* and the *Imaging Ion Spectrometer (IIS)*. The particles pass through pinholes to reach the electron detectors. This enables it to build up a picture of where both the electrons and ions come from. Identification of the ions is based on analysis of the particles' velocities and energy.

For the purpose of this work, only magnetic field data obtained from the FGM and Ion velocities correspondent to the plasma distributions obtained from both, HIA and CODIF from the CIS experiment, will be used in further chapters. A much more detailed explanation of those instruments in comparison with the rest of instruments which are not used during this work was given for this reason.

4 Data Analysis

This chapter will be dedicated to the whole process of data acquisition, preparation, processing and analysis. The aim of this study consists in the detection of flux ropes during magnetic field reconnection events and the statistical analysis of its properties. The data object of analysis is composed by a collection of preselected magnetic reconnection events on the Eart's magnetotail with multiple X-lines formation [4]. Data is obtained from the Cluster mission in a specific format, being necessary some previous pre-processing of the data before being ready to be examined. The methodology used to identify the desired structures contained among this data will be explained in this chapter. The process consists on, acquisition of spacecraft data, processing of this data, definition of the criteria to detect the desired structures, and time analysis of the whole dataset under this criteria. The criteria used for proper detection of the flux ropes structures avoiding poor quality results is one, if not the most, critical point of this section. The acquisition of solid results is primordial, since they will be used later on in this work to perform statistics with the purpose of diving into the physical basics of those structures.

4.1 Data set

The data which will be analyzed is a collection of previously selected magnetic field reconnection events on the near-earth magnetotail [4].Each of the magnetic reconnection events will be examined in order to find small scale flux rope structures among this data. The events will be evaluated using data from the Cluster mission, which can be downloaded from the *Cluster Science Archive (CSA)* [23].

The experiments from the Cluster spacecrafts whose data was acquired are the *Cluster Ion Spectrometer (CIS)* and the *Flux Gate Magnetometer (FGM)*. A detailed description of Both instruments was previously explained with detail in chapter 3.

The CIS, which is composed from the instruments CODIF and HIA, provides information of the ion velocity, calculated from the plasma particle distribution. On the one hand, the velocities of the major ionized particles (H^+,H_e^+ and O^+) can be obtained by CODIF. On the other hand, the velocities of a particle stream are provided by HIA. For both instruments, the particle's velocity is referenced in GSE (Geocentric Solar Ecliptic) coordinates, being defined for a single spacecraft in x,y and z directions of this system. The ion velocity is not relevant for the process of flux rope detection, but it will be important for subsequent statistical studies. A resolution of 4 seconds sampling rate corresponding to the spin rate of the spacecraft is available for this instrument, which is sufficient for the realization of the statistical analysis. No data of CIS from cluster spacecraft 2 is available, since it was damaged shortly after the satellite was launched.
The *Flux Gate Magnetometer (FGM)* provides information about measured magnetic field vector data. Different resolutions are available for the data from the FGM; to wit,spin and

full resolution. Spin resolution refers to one measurement at a time one spacecraft needs to spin completely, which is 4 seconds sampling rate, this resolution coincides with the one from the CIS instrument. On the other hand, full resolution data has a sampling frequency $f_s = 22$ Hz, correspondent to a sampling rate of $T_s = 0.04461$ seconds. The use of full resolution data from the FGM is the most adequate choice for the purpose of this work, since the detection of small scale flux ropes is primordial and most of them would not be detected using spin resolution of 4 seconds sampling rate.

Event number	**Event begin**	**Event end**
1	2001-08-17 | 16:08:00	2001-08-17 | 17:05:00
2	2001-08-22 | 09:25:00	2001-08-22 | 10:25:00
3	2001-08-27 | 03:40:00	2001-08-27 | 04:35:00
4	2001-09-10 | 07:30:00	2001-09-10 | 08:20:00
5	2001-09-12 | 12:40:00	2001-09-12 | 13:50:00
6	2002-09-15 | 04:35:00	2002-09-15 | 05:35:00
7	2001-10-01 | 09:05:00	2001-10-01 | 10:15:30
8	2001-10-08 | 12:35:00	2001-10-08 | 13:25:00
9	2001-10-11 | 03:10:00	2001-10-11 | 04:00:00
10	2002-08-14 | 02:30:00	2002-08-14 | 03:30:00
11	2002-08-14 | 03:30:00	2002-08-14 | 04:40:00
12	2002-08-18 | 16:45:00	2002-08-18 | 17:35:00
13	2002-08-18 | 17:10:00	2002-08-18 | 17:55:00
14	2002-08-21 | 07:30:00	2002-08-21 | 09:00:00
15	2002-08-28 | 09:37:00	2002-08-28 | 10:25:00
16	2002-09-13 | 17:51:00	2002-09-13 | 18:40:00
17	2002-09-18 | 12:41:00	2002-09-18 | 13:55:00
18	2002-10-02 | 20:55:00	2002-10-02 | 21:55:00
19	2002-10-26 | 08:55:00	2002-10-26 | 09:45:00
20	2003-10-02 | 00:10:00	2003-10-02 | 01:15:00
21	2003-10-09 | 02:00:00	2003-10-09 | 02:50:00
22	2003-07-29 | 18:10:00	2003-07-29 | 18:55:00
23	2003-08-22 | 13:00:00	2003-08-22 | 13:50:00
24	2003-08-24 | 18:15:00	2003-08-24 | 19:30:00
25	2003-09-01 | 04:05:00	2003-09-01 | 04:55:00
26	2003-09-19 | 23:10:00	2003-09-19 | 23:50:00
27	2003-10-04 | 05:51:00	2003-10-04 | 06:50:00
28	2004-08-19 | 17:40:00	2004-08-19 | 18:50:00
29	2004-10-03 | 17:30:00	2004-10-03 | 18:45:00
30	2005-08-22 | 23:15:00	2005-08-23 | 00:14:00
31	2005-08-28 | 23:21:00	2005-08-29 | 00:04:00

Table 4.1: List of magnetic reconnection events on the magnetotail [4]

The data from CIS and FGM is downloaded from the CSA for the list of events shown in

Table 4.1, where the duration of each event was extended about 15 minutes before and after magnetic reconnection happened. This list of events forms the dataset which will be used as basis for this work.

The data will be analyzed using the commercial software *IDL(Interactive data language)*[24] and the *TDAS (Themis Data Analysis Software) /SPEEDAS (Space Physics Environment Data Analysis Software)*[26] libraries, which will add some additional features to the basis contents of IDL.

A complete step by step walk-through of the whole data acquisition process from the CSA and its graphical user interface as well as an extensive description of the main IDL and TDAS functions used to handle the data are shown in Appendix B.

4.2 Flux rope crossing

Flux ropes located on the magnetotail are helical magnetic structures which are associated with either plasmoids produced by *Multiple X-line Reconnection (MXR) [Hughes and Sibeck, 1987; Slavin, et. al, 2003]* [17, 18] or as a secondary magnetic islands formed in the unstable electron current layer of a single reconnection site. Due to its helical structure, a flux rope should show a very characteristic pattern on its magnetic field components when a spacecraft crosses such a structure.

4.2.1 Shape of the magnetic field components

The nature of the flux ropes and its characteristic magnetic field patterns were previously discussed in section 2.4. Different scenarios in which a spacecraft could encounter a flux rope traveling down or up the tail represented in figure 4.1 were considered and the different shape for the magnetic field components were analyzed. In figure 4.1 the trajectories are shown in red, the circular black lines represent the flux ropes, the horizontal black line represents the current sheet, and the shape of the magnetic field components are shown aside. Gathering the situations shown in all scenarios together, it could be concluded, that independently of the occurring trajectory in which a flux rope crosses the spacecraft, some patterns in the measurements of the magnetic field components are always very characteristic:

A bipolar variation of the $\mathbf{B_z}$ component is always measured, the symmetry of the signal will depend on how far the points of entry and exit are situated referenced to the current sheet, becoming more symmetric for much similar distances. The "polarity" of the bipolar variation depends on the direction of the flux rope's motion. If the flux rope moves towards the positive X direction (towards earth), then the B_z component will show a minimum and then a maximum, going from more negative (or less positive) values to less negative (or more positive) values depending on the value of B_z background. On the other hand, the inverted polarity will characterize the signal when the flux rope moves to the negative X direction (against the earth). In this case B_z will show a maximum and then a minimum, going from more positive (or less negative) values to less positive (or more negative) values.

A local maximum or minimum in the $\mathbf{B_y}$ component will be always registered, the polarity of the core field $B_{y\,CORE}$ will determine the shape of this measurement. For a

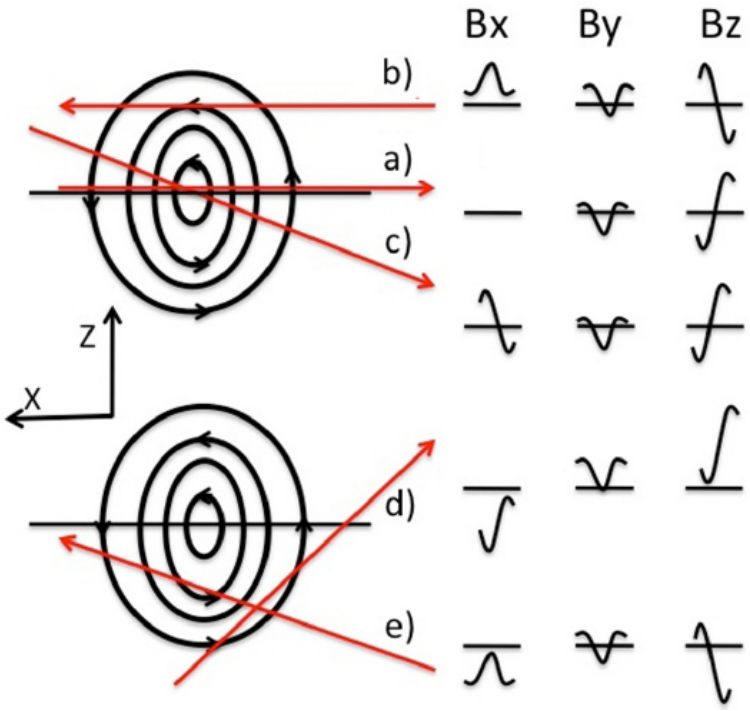

Figure 4.1: Sketch of the model used to identify the existence of flux ropes showing the spacecraft trajectories for several scenarios[11]

determined background value of B_y which could be either positive or negative, a minimum will be encountered if the polarity of $By\,CORE$ is negative, reaching more negative (or less positive) values, whereas a maximum will occur if $B_{y\,CORE}$ polarity is positive, achieving more positive (or less negative) values. This point should be located in time between the time instants of the two points characterizing the bipolar B_z variation, and it would be a good reference point to allocate the instant where a flux rope is detected.

A maximum or a minimum in |B| referenced to the background will also be measured due to the combined effect of all three magnetic field components. The bipolar variation of B_z registers the background value of B_z for the instant where the peak of B_y occurs, while at the same time B_x will either show also the background value of B_x, if the signature of the signal is bipolar, or a peak value which could also be a maximum or a minimum and will be superposed in that case to the peak value of B_y. Based on the previous explanation can be concluded, that the value of $|B|$ will always show a maximum or a minimum independently of the trajectory if a flux rope is encountered. Furthermore, this instant will coincide with the instant where the peak on the B_y component is measured.

Those mentioned above are the three ideal criteria which will be used to detect flux ropes existing among the data to be analyzed. The real implementation of such criterion is not as

simple, and it will lead to a series of selective criteria and acceptance thresholds which will be explained afterwards in section 4.3.2.2.

4.2.2 Transformation from GSE to LMN coordinate system

The characteristic patterns of the magnetic field components characterizing a flux rope have been explained in detail in the previous section 4.2.1. Nevertheless, the coordinate system used in the model was a right-handed orthogonal coordinate system whose Z axis was normal to the current sheet, whereas the remaining two axis X and Z where tangential to the plane of the current sheet, while the data downloaded from the CSA is expressed in GSE coordinates. The former system should show a clear, almost constant value of the background values of the magnetic field components, and the patterns in each of the magnetic field components which characterize the crossing between a spacecraft and a flux rope should be clearly recognizable, making it relatively easy to detect. However in the latter, the values of the background magnetic field components will not remain around a constant value, and the patterns in each magnetic field component during a flux rope encounter will be partially allocated in the remaining components, being the patterns in the corresponding magnetic field components gradually less recognizable as the difference between GSE and the former coordinate system of the model presented in Figure 4.1 becomes more accentuated.

The data downloaded from the CSA is expressed in GSE coordinates. The *Geocentric Solar Ecliptic (GSE)* coordinate system has its X axis towards the Sun and its Z axis perpendicular to the ecliptic plane, which is the rotation plane of the Earth around the sun, the Y-axis is contained in the ecliptic plane from dusk to down, opposing planetary motion. This system is fixed with respect to the Earth-Sun line and it is convenient for specifying magnetospheric boundaries. On the other hand , the model for the flux rope crossing uses a right-handed orthogonal local coordinate system whose Z axis is normal to the current sheet, whereas the remaining two axis X and Z are tangential to the plane of the current sheet. This coordinate system shows a clear, almost constant value of the background values of the magnetic field components, and the patterns in each of the magnetic field components charactering the crossing between a spacecraft and a flux rope should be clearly recognizable, making it relatively easy to detect. This local coordinate system is called *LMN* and is obtained through a minimum variance analysis of the magnetic field data. The methodology is explained in Appendix C.

The data acquired from the CSA expressed in the GSE coordinate system has to be transformed to LMN coordinate system correspondent to the *Minimum Variance Analysis (MVA)*. The new coordinates are achieved applying a coordinate transformation which basically consists in a rotation of the vectors, since the former system GSE and the latter LMN are orthogonal right-handed systems, the rotation is executed as:

$$\overrightarrow{r}_{LMN} = M_{uv} \cdot \overrightarrow{r}_{XYZ} \tag{4.1}$$

$$\begin{pmatrix} \overrightarrow{r}_L \\ \overrightarrow{r}_M \\ \overrightarrow{r}_N \end{pmatrix} = \begin{pmatrix} m_{LX} & m_{LY} & m_{LZ} \\ m_{MX} & m_{MY} & m_{MZ} \\ m_{NX} & m_{NY} & m_{NZ} \end{pmatrix} \cdot \begin{pmatrix} \overrightarrow{r}_X \\ \overrightarrow{r}_Y \\ \overrightarrow{r}_Z \end{pmatrix} \tag{4.2}$$

Where X,Y and Z represent the coordinates of GSE, whereas L,M and N are the

correspondent in the minimum variance system. The 3×3 simmetric matrix M_{uv} represents the rotation matrix whose coefficients are obtained through realization of a minimum variance analysis from the magnetic field measurements of the cluster spacecraft during a crossing of the current sheet, a detailed explanation about the minimum variance analysis fundamentals can be found in Appendix C. The corresponding transformation matrices for each event were calculated for each of the events on the list shown in Table 4.1, and are shown in the tables on appendix A.

The minimum variance matrices shown in the four tables from Appendix A, are obtained from a previous work *[Alexandrova,2016]*[4], whose main topic was the temporal evolution and spatial characteristics of the magnetotail. The minimum variance analysis was realized with magnetic field data registered before magnetic reconnection occurred. Nevertheless, due to the rearrangement and merging of the magnetic field lines occurring during reconnection, the minimum variance coordinates may be no longer corresponding to the calculated minimum variance coordinate system corresponding to the situation before reconnection happened. Despite this fact, the current corresponding LMN coordinates will be considered to be representative of the minimum variance coordinate system for each corresponding event. However in order to be exhaustively accurate, after a flux rope is detected in the current frame, a local MVA should be realized using the magnetic field data registered close to the instant where the detection is located, this would lead to a multi-step or even iterative analysis of the data. This possibility was decided to be not considered during this work, as the initial MVA should give a sufficiently good orientation of the vectors for a good analysis of the magnetic field components, although it could be an interesting direction to go for further improvements.

4.3 Flux rope detection

The variables obtained from the FGM containing the magnetic field data as well as the variables from the CIS containing the velocities of the particles will be the basis for this study. The former will be indispensable for the detection of the flux ropes following the model explained *[Borg et. al. 2012]*[11], the latter will not be used for the purpose of flux rope detection, but used later on as a very important flux rope's characteristic parameter for the statistical analysis. Data is properly transformed to the correspondent minimum variance coordinate system as explained in the previous section, being the variables shown in LMN components.

The time series of the variables corresponding to the event of 22^{th} August 2001 is shown in Figure 4.2 as an example of how is really the data from the events looking alike. The event should always start with an almost constant value in the variables among time, as magnetic reconnection has still not occurred and the phenomena acting in this situation (e.g. solar wind) have small influence under the magnetic field signatures of the data. However, after some point data starts to change rapidly in time and it starts to acquire a really stochastic nature, indicating that magnetic reconnection is starting to occur after this point. This situation will last until the end of the reconnection event, indicated when the values of the magnetic field components tend to go back again to its initial value after reconnection started. The magnitude of the out-of-plane magnetic field component B_m measured before magnetic reconnection started to influence the magnetic field signatures is called the magnetic *guide*

field. The **guide field** could be estimated averaging the measurements of the out-of-plane magnetic field component B_m from the starting point of the event until the point when magnetic reconnection started. In practice, the guide field will be calculated averaging the data of the first 15 minutes of event, which were added to the initial and final times of each event to ensure a reliable calculation of this guide field. The aforementioned region where guide field is calculated is indicated with a purple arrow in Figure 4.2.

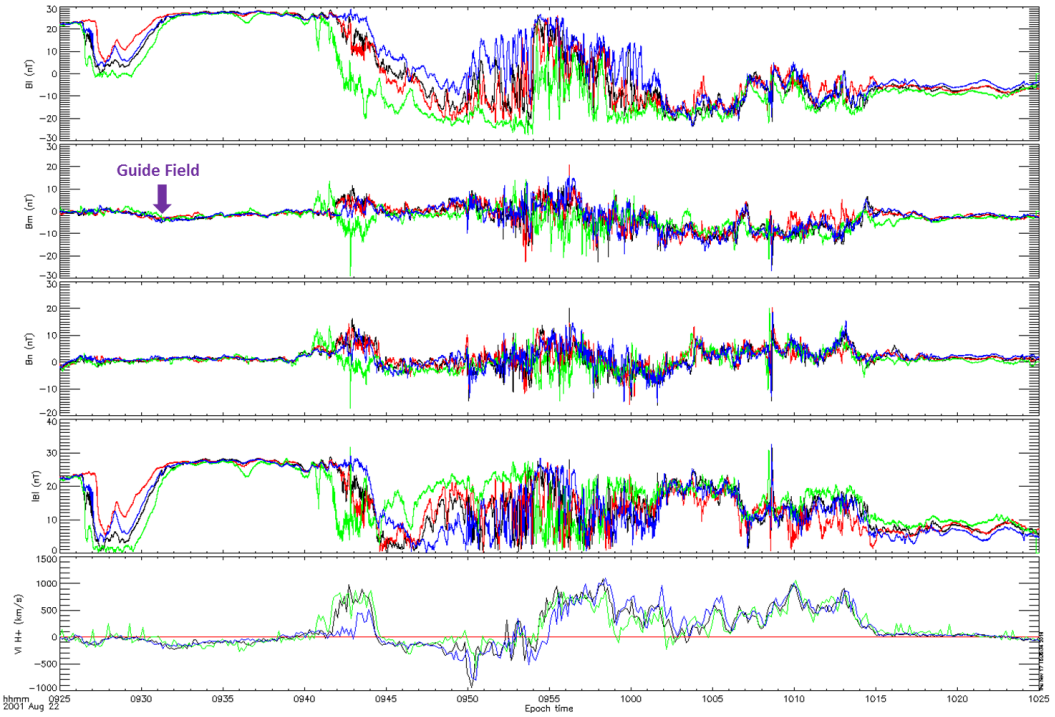

Figure 4.2: Time series of the LMN magnetic field components, magnitude and ion velocity in L direction from CODIF, each spacecraft is represented with a different color: 1-black, 2-red, 3-green, 4-blue.

The representation in Figure 4.2 intends to show a perspective view about the appearance of the data characterizing an event. The most relevant parameters for the process of flux rope detection are the magnetic field components B_n and B_m as well as the absolute magnitude of the magnetic field $|B|$, where the characteristic patterns of a flux rope encounter should appear.

For a proper analysis of the data, an automated search algorithm is developed to check the contents of the data and look for the desired patterns in each signal. The algorithm should be capable of detecting every possible flux rope independently of its size, starting with a setup designed to detect the biggest structures, and changing its setup progressively to detect more and more small structures as the analysis runs.

4.3.1 The time analysis window

This analysis is realized in time domain, so a window which could be named as *big analysis window* will be defined to scan the data. This analysis window will be defined by a certain number of time samples N_{big}, and it is designed to analyze the data which is contained inside. Furthermore, a new smaller window contained inside the big analysis window and whose center will be placed at sample $\frac{N_{big}}{2}$ will also be defined, this will be named the *small analysis window* and its size corresponds to $N_{small} = \frac{N_{big}}{4}$. These two windows will be used to scan the whole collection of data of an event and the specific objective of each one will be explained in detail later in this section. First of all at the windows start at the initial sample and will scan the data contained inside the first N_{big} samples, straightforward the big window will move a distance of $\frac{N_{big}}{32}$ samples, and so will do the small window in the adequate proportion corresponding to the updated middle sample of the big window.

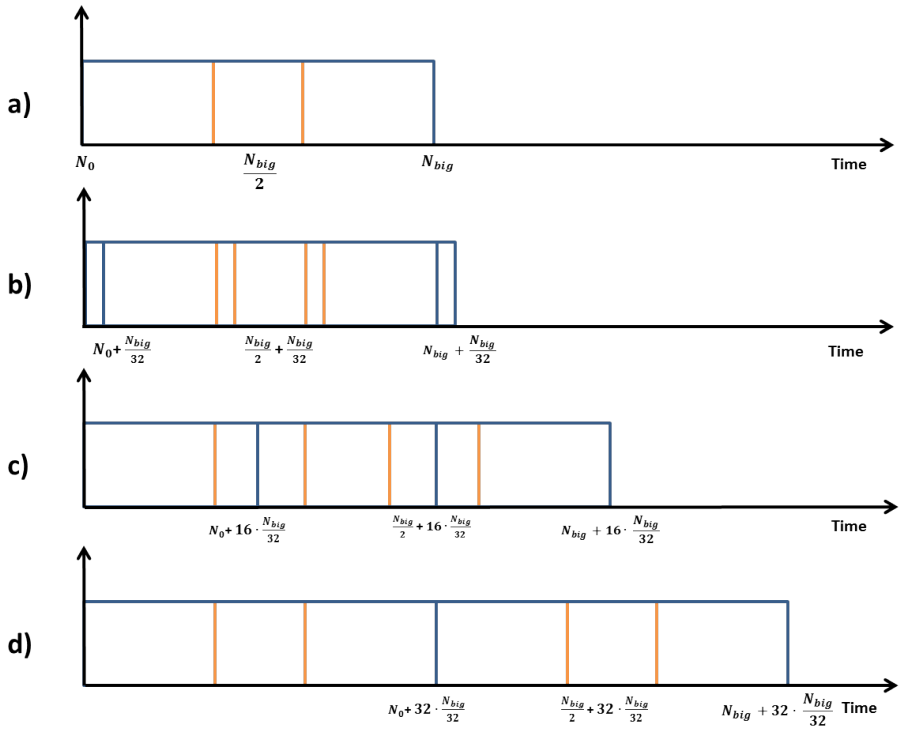

Figure 4.3: Sequence of the big(blue) and small (orange) analysis windows motion, 32 iterations are needed until data is completely renewed.

This small displacement of the window will lead to redundancy in the data analysis, since the data contained inside a window will not be completely refreshed until 32 iterations are done, this sequence is shown in Figure 4.3, where the situations shown are: a) Windows at starting instant of the analysis; b) First iteration with the windows displaced a time corresponding to $\frac{N_{big}}{32}$ samples; c) Iteration number 16 with the windows displaced a time corresponding to $\frac{N_{big}}{2}$ samples; d) Iteration number 32 with the windows displaced a time

corresponding to N_{big} samples, data after this point is completely new in respect to the first window. This amount of iterations may seem a bit excessive, but due to the fact that the conditions imposed for the flux rope detections are very restrictive, it would be reasonable to examine the data many different times with slightly small variations in the data contained inside the windows. This will help not to overlook flux rope detections just because the conditions imposed where slightly not fulfilled. This number of 32 overlapping windows was determined empirically after some try and error, since no remarkable improvement on the flux rope detections was appreciated for higher number of overlapping windows than 32, while signal processing times started to increase dramatically.

For the definition of analysis windows to be complete, the number of samples N_{big} needs to be defined. As was mentioned previously, the algorithm should be designed to detect each possible size of flux rope, so it was decided to make a sequential scan of overlapping windows of the whole data several times for different window sizes. The window size will be characterized by a time duration T_{big}, and several different time scales will be considered to cover the whole range of possible flux rope sizes, the number of samples will then be calculated by simple multiplication with the sample frequency of the full resolution data, which is around $f_s = 22$ Hz or around a sample rate of $T_s = 0,045$ sec. The different windows sizes and the corresponding scales are shown in Table 4.2 ordered from 1 to 8 from bigger to smaller.

Big window scale	**Big window time T_{big}**	**Big window samples N_{big}**	**Small window samples N_{small}**
1	360 s	7920	1980
2	180 s	3960	990
3	90 s	1980	495
4	45 s	990	248
5	25 s	550	138
6	15 s	330	83
7	10 s	220	56
8	5 s	110	28

Table 4.2: Size of the different windows determined for each scan of the data with a sample frequency around $f_s = 22$ Hz.

The method of the moving windows will be used to scan the data of each event several times as was explained before. The windows will sweep all data from an event until it encounters some amount of data contained inside of them which fulfills the detection criteria, which will be explained soon after finishing this section. The situation in Figure 4.4 shows how a window is relatively small compared to the whole duration of the event, a full scope scenario of both windows can be seen in Figure 4.5, where it is realized, this is a window of scale 3 type with a duration of 90 seconds for the big window. Taking a look to Figure 4.5 can be understood why the windows are defined in such a way. In this situation, the signatures of the magnetic field components contained inside of the small window resemble the patterns on the magnetic field components commented in 4.2.1, while the fraction of the data located between the big and the small window could be considered to be the background

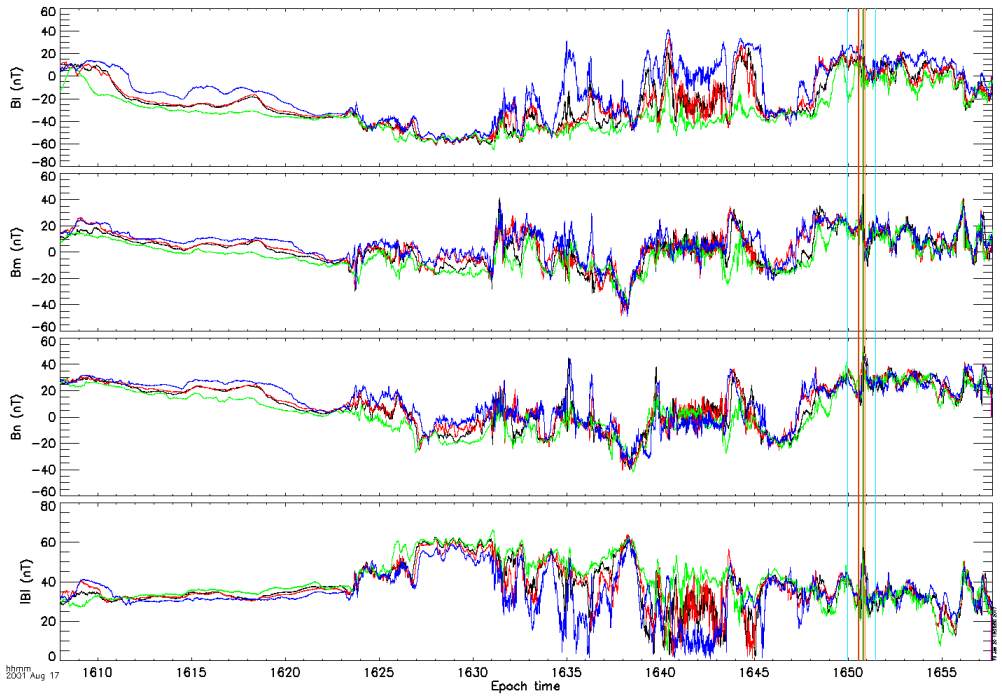

Figure 4.4: Big (blue) and small (orange) analysis windows shown in the frame of the whole event.

value of the magnetic field, in case this would be a flux rope detection. Generalizing, the big window will be used to determine the values of the background magnetic field (before and after) regarding a flux rope encounter, while the purpose of the small window will be the delimitation of the area where the magnetic field patterns are checked for existence.

4.3.2 Detection criteria

The criteria for the flux rope detection will be based on the characteristic patterns of the magnetic field components commented during section 4.2.1, although the criteria should be adapted to a more realistic case.

The criteria should define a more or less clear shape of the magnetic field components, although in reality, the shape of the magnetic field components will always differentiate a bit from this "ideal" shape. In the end, a compromise between accuracy and reality should be reached in order to avoid fake detections of flux rope structures, but also avoid overlooking some flux rope structures just because one or some of the conditions are slightly not fulfilled.

4.3.2.1 Parameter definition

The detection criteria will consist in a series of restrictive conditions that ensure the shape of the magnetic field components to resemble the magnetic field patterns previously discussed. The conditions will be established based on the parameters represented in figures 4.6 and 4.7,

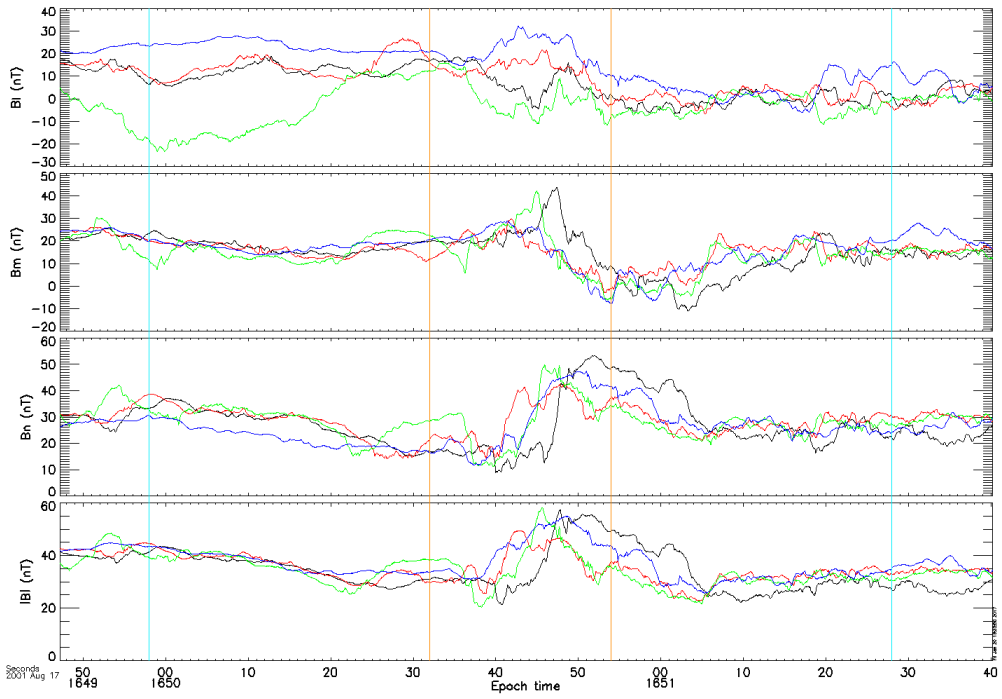

Figure 4.5: Big (blue) and small (orange) analysis windows shown in a proper scale.

those are:

Big window: Region corresponding to the samples contained inside the two vertical blue lines shown in Figure 4.6. The window is divided in left and right side, separated by the small window, characterized here by the two orange vertical lines. The left side of the big window begins at the sample where the left blue vertical line is placed N_{BWB} and finishes at the sample where the left orange vertical line is placed N_{SWB}. The right side of the window begins at the sample where the right orange vertical line is placed N_{SWE} and finishes at the sample where the right blue vertical line is located N_{BWE}. The size of the window corresponds to the number of samples separating both vertical blue lines ΔN_{BW}.

$$\Delta N_{BW} = N_{BWE} - N_{BWB} \tag{4.3}$$

Small window: Region corresponding to the samples contained inside the two vertical orange lines shown in Figure 4.6. The window size is 8 times smaller than the big window N_{BW} and corresponds to the number of samples separating the two vertical orange lines ΔN_{SW}, which coincide with the final and starting points of the left and right big window sides respectively.

$$\Delta N_{SW} = N_{SWE} - N_{SWB} \tag{4.4}$$

Small and big windows central point ($\mathbf{N_{W\,mid}}$): The central sample corresponding

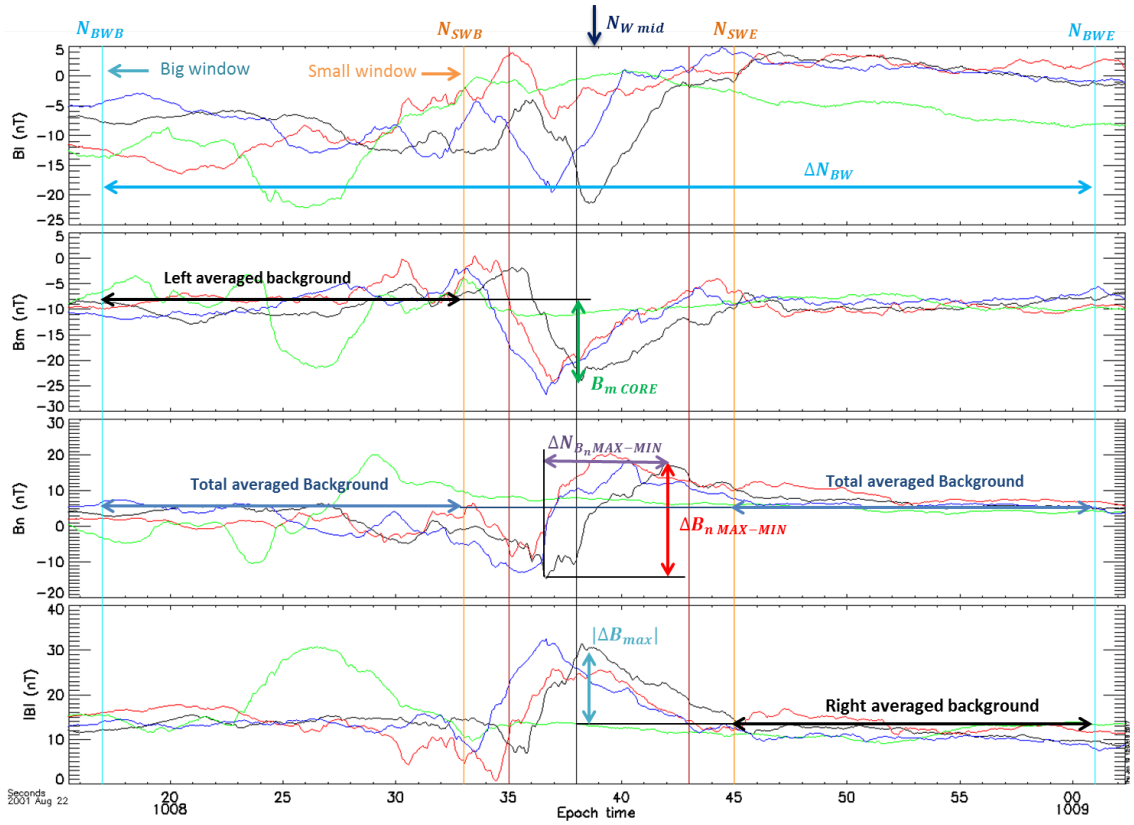

Figure 4.6: First of two pictures representing the flux rope detection on 22 Aug 2001 of spacecraft 1 (black) where the multiple parameters used to define the detection criteria are shown.

to the instant at which the windows are symmetric to the left and the right side.

$$N_{W\ mid} = \frac{N_{BWB} + N_{BWE}}{2} = \frac{N_{SWB} + N_{SWE}}{2} \tag{4.5}$$

Left averaged background $\left(\overline{\mathbf{B_{left\ BG}}}\right)$**:**Averaged value of the magnetic field data for the region contained inside the left side of the big window (small window region excluded).

$$\overline{B_{left\ BG}} = \frac{1}{N_{SWB} - N_{BWB}} \sum_{i=N_{BWB}}^{N_{SWB}} B_i \tag{4.6}$$

Variance of the left background $\left(\mathbf{var}\left(\overline{\mathbf{B_{left\ BG}}}\right)\right)$**:** Second central moment of the magnetic field data contained inside the left side of the big window.

$$var\left(\overline{B_{left\ BG}}\right) = \frac{1}{N_{SWB} - N_{BWB}} \sum_{i=N_{BWB}}^{N_{SWB}} \left(B_i - \overline{B_{left\ BG}}\right)^2 \tag{4.7}$$

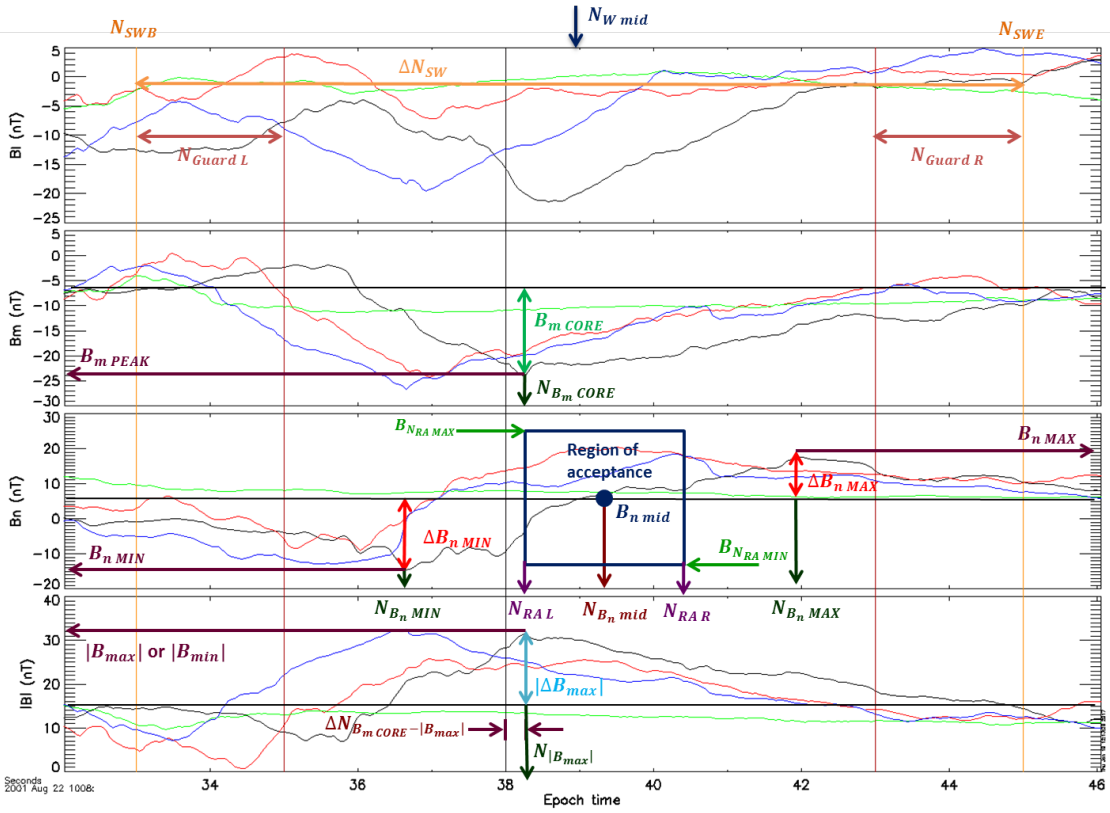

Figure 4.7: Second of two pictures representing the flux rope detection on 22 Aug 2001 of spacecraft 1 (black) where the multiple parameters used to define the detection criteria are shown.

Right averaged background $\left(\overline{\mathbf{B_{right\ BG}}}\right)$**:**Averaged value of the magnetic field data for the region contained inside the right side of the big window (small window region excluded).

$$\overline{B_{right\ BG}} = \frac{1}{N_{BWE} - N_{SWE}} \sum_{i=N_{SWE}}^{N_{BWE}} B_i \tag{4.8}$$

Variance of the right background $\left(\mathbf{var}\left(\overline{\mathbf{B_{right\ BG}}}\right)\right)$**:**Second central moment of the magnetic field data contained inside the right side of the big window.

$$var\left(\overline{B_{right\ BG}}\right) = \frac{1}{N_{BWE} - N_{SWE}} \sum_{i=N_{SWE}}^{N_{BWE}} \left(B_i - \overline{B_{right\ BG}}\right)^2 \tag{4.9}$$

Total averaged background$\left(\overline{\mathbf{B_{total\ BG}}}\right)$**:** Averaged value of the magnetic field data for the whole region contained inside the big window (small window region excluded)

$$\overline{B_{total\ BG}} = \frac{\overline{B_{right\ BG}} + \overline{B_{left\ BG}}}{2} \tag{4.10}$$

$\mathbf{N_{B_n\,MAX}}$: Sample of the time instant where the maximum value of the B_n component is reached inside the small window.

$$N_{B_n\,MAX} = argmax_N B_n\,(N) \tag{4.11}$$

$\mathbf{\Delta B_{n\,MAX}}$: Difference of magnitude between the value of B_n at the instant indicated by $N_{B_n\,MAX}$ and the background value. This can be referred to left, right or total averaged background.

$$\Delta B_{n\,MAX} = B_n\,(N_{B_n\,MAX}) - \overline{B_{n\,BG}} \tag{4.12}$$

$\mathbf{N_{B_n\,MIN}}$: Sample of the time instant where the minimum value of the B_n component is reached inside the small window.

$$N_{B_n\,MIN} = argmin_N B_n\,(N) \tag{4.13}$$

$\mathbf{\Delta B_{n\,MIN}}$: Difference of magnitude between the value of B_n at the instant indicated by $N_{B_n\,MIN}$ and the background value. This can be referred to left, right or total averaged background.

$$\Delta B_{n\,MIN} = B_n\,(N_{B_n\,MIN}) - \overline{B_{n\,BG}} \tag{4.14}$$

$\mathbf{\Delta B_{n\,MAX-MIN}}$: Difference in absolute value between the values of B_n at the instants indicated by $N_{B_n\,MIN}$ and $N_{B_n\,MAX}$.

$$\Delta B_{n\,MAX-MIN} = |\Delta B_{n\,MIN} - \Delta B_{n\,MAX}| \tag{4.15}$$

$\mathbf{\Delta N_{B_n\,MAX-MIN}}$: Number of samples separating the points of where the maximum and minimum value for B_n is reached.

$$\Delta N_{B_n\,MAX-MIN} = |N_{B_n\,MIN} - N_{B_n\,MAX}| \tag{4.16}$$

Central $\mathbf{B_n}$ point ($\mathbf{N_{B_n\,mid}}$): Sample correspondent to the time instant located exactly in the middle point between the indexes that correspond to the maximum and minimum values of B_n.

$$\Delta N_{B_n\,mid} = min\,(N_{B_n\,MIN}, N_{B_n\,MAX}) + \Delta N_{B_n\,MAX-MIN} \tag{4.17}$$

Value of $\mathbf{B_n}$ at the central $\mathbf{B_n}$ point ($\mathbf{B_n}$): value of the signal B_n to the instant corresponding to the sample $N_{B_n\,mid}$.

$$B_n\,(N_{B_n\,mid}) \tag{4.18}$$

$\mathbf{N_{B_n\,mid}}$: Sample corresponding to the time instant where a peak correspondent to a minimum or a maximum in the B_m component with the biggest difference in magnitude to the background value is registered.

$$N_{B_m\,CORE} = argmax_N \left(B_m\,(N) - \overline{B_{m\,BG}}\right) \tag{4.19}$$

Core field of $\mathbf{B_m}$ ($\mathbf{B_{m\,CORE}}$): Biggest difference in magnitude between the maximum or minimum value of the B_m component and the background value of B_m. Left, right or total background values could be used for this definition.

$$B_{m\,CORE} = max\left(B_{m\,max}\,(N) - \overline{B_{m\,BG}}, B_{m\,min}\,(N) - \overline{B_{m\,BG}}\right) \tag{4.20}$$

$\mathbf{N_{|B_{max}|}}$: Sample of the time instant where the maximum or the minimum value of the magnetic field value $|B|$ with the biggest difference to the background value of $|B|$ is registered.

$$N_{|B_{max}|} = argmax_N\left(|B\,(N)| - \overline{|B_{BG}|}\right) \tag{4.21}$$

$|\mathbf{\Delta B_{max}}|$: Difference between the maximum $|\Delta B_{max}|$ or minimum $|\Delta B_{min}|$ value of the magnetic field total magnitude and the background value of $|B|$. background can be referred to as left, right or total.

$$|\Delta B_{max}| = max\left(|B_{max}| - \left|\overline{B_{BG}}\right|, |B_{min}| - \left|\overline{B_{BG}}\right|\right) \tag{4.22}$$

$\mathbf{\Delta B_{m\,CORE-|B_{max}|}}$: Number of samples between the points where the core field $B_{m\,CORE}$ and the maximum variation of the total magnitude $|\Delta B_{max}|$ are registered.

$$\Delta B_{m\,CORE-|B_{max}|} = \left|N_{B_m\,CORE} - N_{|B_{max}|}\right| \tag{4.23}$$

Guard distance right ($\mathbf{N_{Guard\,R}}$) and left ($\mathbf{N_{Guard\,L}}$): Certain number of samples distanced towards the inside from the right and left side of the small window. It corresponds to one eight of the small window size. It will be later used to introduce some additional reliability.

$$N_{Guard\,L} = N_{SWB} + \frac{\Delta N_{SW}}{8} \tag{4.24}$$

$$N_{Guard\,R} = N_{SWE} - \frac{\Delta N_{SW}}{8} \tag{4.25}$$

Region of acceptance of $\mathbf{B_n}$: Region centered in $N_{B_n\,mid}$ including an interval of values of N and B_n around the background value. Will help to introduce some conditions for additional reliability.

$$B_{n_{RA\,MAX}} = B_n\,(N_{B_n\,MAX}) - \frac{\Delta B_{n\,MAX-MIN}}{8} \tag{4.26}$$

$$B_{n_{RA\,MIN}} = B_n\,(N_{B_n\,MIN}) + \frac{\Delta B_{n\,MAX-MIN}}{8} \tag{4.27}$$

$$N_{RA\,L} = N_{B_n\,mid} - \frac{\Delta B_{n\,MAX-MIN}}{8} \tag{4.28}$$

$$N_{RA\,R} = N_{B_n\,mid} + \frac{\Delta B_{n\,MAX-MIN}}{8} \tag{4.29}$$

4.3.2.2 Modelling of the conditions

The parameters defined above are used to define the detection criteria and build up the automatic detection algorithm for the flux rope detection. The criteria should try to detect the patterns on the magnetic field components which were previously commented in section 4.2.1, although it should include some degree of tolerance in the shape of the components. This is justified, as the data representing an event will never present such ideal and clean signals as were considered by defining the conditions for the flux rope detection. The more realistic detection criteria is then implemented as different adaptations of the conditions commented in section 4.2.1.

Detection of the bipolar $\mathbf{B_n}$ signature: The characteristic signature of the B_n component is the first criterion to be verified in each position of the analysis window. The left and right sides of the big analysis window will be used to check the properties of the background, while the small window will be used to check the data in the surroundings of the central point of the windows. The verification of this criterion will be realized by the following conditions:

- **Background value before and after is around a constant value.** It is almost impossible, that the values of the background on the left side and on the right side are equal. In reality $\Delta B_{n\,BG} = \left|\overline{B_{n\,right\,BG}} - \overline{B_{n\,right\,BG}}\right| \neq 0$, so a certain threshold of acceptance ϵ_{B_n} has to be introduced to consider the background value of B_n to be constant when $\overline{\Delta B_{n\,BG}} < \epsilon_{B_n}$.

- **The variance of the left and right background magnetic field is small compared to the** $mathbf{B_n}$ **bipolar signature.** The variance of the background values of B_n contained inside the left and right big window sides should present a variance below a reasonable threshold. The condition will be implemented as $var\left(B_{n\,BG}\right) < K^2_{n\,var} \cdot \left(max\left(\left|\Delta B_{n\,MAX}\right|, \left|\Delta B_{n\,MIN}\right|\right)\right)^2$, it can be rearranged and then the quotient between the variance and the square of the maximum amplitude registered between background and B_n inside the small window could be called *normalized variance*, defined as $\widehat{var(B_{n\,BG})} = \frac{var(B_{n\,BG})}{\left(max(|\Delta B_{n\,MAX}|,|\Delta B_{n\,MIN}|)\right)^2} < K^2_{n\,var}$. From this definition a restriction related to the maximum amplitude of the bipolar Bn signature can be implemented. Summarizing, the condition $\widehat{var(B_{n\,BG})} < K^2_{n\,var}$ should be accomplished, where the background refers to either right or left background (should be fulfilled for both separately), and $0 < K_{n\,var} < 1$. This condition together with the previous one should be enough to ensure a proper shape of the background part of the signals contained inside the big window.

- **The difference between the maximum and minimum value of** $mathbf{B_n}$ **and the total average background is much bigger than the difference between right and left background.** As previously commented, a certain value of $\Delta B_{n\,BG} > 0$ will always be present. It would be coherent to ensure that the difference between $\Delta B_{n\,MAX-MIN}$ is bigger in magnitude compared to $\Delta B_{n\,BG}$. The condition is implemented as $\Delta B_{n\,MAX-MIN} > K_{\Delta B_{n\,BG}} \cdot \Delta B_{n\,BG}$ where $K_{\Delta B_{n\,BG}} > 1$ is a constant value.

- **The maximum value of $\mathbf{B_n}$ is considerably bigger than the total average of the background.** This condition will ensure that the maximum value of B_n located inside of the small window presents a considerable difference in magnitude referred to the mean background value outside of the small window. This criterion is implemented as $\Delta B_{n\,MAX} > K_{\Delta B_n}$ where $\Delta B_{n\,MAX}$ is referred to the total averaged background $K_{\Delta B_n} > 0$ is a constant value.

- **The minimum value of $\mathbf{B_n}$ is considerably smaller than the total average of the background.** Same condition as the previous but for the minimum of B_n inside the small window. This criterion is implemented as $\Delta B_{n\,MIN} < -K_{\Delta B_n}$ where $\Delta B_{n\,MIN}$ is once again calculated referred to the total background mean. This condition together with the previous one and the third condition $\Delta B_{n\,MAX-MIN} > K_{\Delta B_n} \cdot \Delta B_{n\,BG}$ should ensure that a clear bipolar variation of the B_n component around the background value is registered in case of detection.

- **The indexes correspondent to the maximum and minimum values of $\mathbf{B_n}$ should not be close to the limits of the small window.** This condition is implemented to avoid the undesirable situation where a maximum or a minimum is detected very close to the limits of the small window and the signal continues to increase or decrease outside of the small window. The condition is designed based on the left $N_{Guard\,L}$ and right $N_{Guard\,L}$ guard distances, and is modelled with the following condition.

$$N_{Guard\,R} > N_{B_n\,MIN}, N_{B_n\,MAX} > N_{Guard\,L} \tag{4.30}$$

- **The indexes correspondent to the maximum and minimum values of $\mathbf{B_n}$ should not be close to the center of the small window.** This condition has the purpose to ensure that the bipolar variation of B_n will not be either shifted to one side of the small window or be too compressed in comparison with the window size. In the former, the detection will be registered a few steps after as the window moves and the signal is more centered in the small window, while in the latter; the detection should be registered later in the analysis, when a smaller window covers again this region of the data. The condition is in this case defined based on the small window size Δ_{BSW} and central point of the windows $N_{W\,mid}$.

$$N_{B_n\,MIN} < N_{W\,mid} - \frac{\Delta N_{SW}}{8} \tag{4.31}$$

$$N_{B_n\,MAX} < N_{W\,mid} + \frac{\Delta N_{SW}}{8} \tag{4.32}$$

- **The value of the $\mathbf{B_n}$ component at the equidistant point from $\mathbf{B_{n\,MAX}}$ and $\mathbf{B_{n\,MIN}}$ is around the background value.** This is the last condition for the detection of the B_n bipolar signature, and it is intended for ensuring that the signal presents a certain degree of symmetry around $N_{B_n\,mid}$. The value of the signal at B_n ($N_{B_n\,mid}$) should ideally present the same value as the background, although in reality this would

never happen. The value for $B_n\,(N_{B_n\,mid})$ will then be considered as acceptable if it is contained inside the region of acceptance given by the condition.

$$B_{n_{RA\,MIN}} < B_n\,(N_{B_n\,mid}) < B_{n_{RA\,MAX}} \tag{4.33}$$

The simultaneous fulfillment of those previous conditions should assure the achievement of a proper shape for the magnetic field B_n component, which is the first of the criterions designed for a proper detection of a flux rope. The definition of this first criterion included a big amount of conditions, since the shape of the magnetic field for this component is much more complicated to define as the others will be. The detection algorithm will only continue to the next step if and only if all of the conditions shown previously are matched and the first detection criterion is fulfilled, otherwise the algorithm will skip this region of data and the windows will move to the next iteration.

Detection of the characteristic peak on the $\mathbf{B_m}$ component. This is the second detection criterion to be met. The values for the background will be analyzed by the big window, while the characteristic shape of the signal will be sought inside of the small window. The criterion will be accomplished when the following conditions are matched:

- **Background value of $\mathbf{B_m}$ before and after is around a constant value.** Same as for the first criterion of detection, also for the B_m component the difference between the averaged background magnetic fields at the left and the right side big windows have to remain smaller than a certain value. Again a certain threshold of acceptance ϵ_{B_m} has to be introduced to consider the background value of B_m to be constant when $\overline{\Delta B_{m\,BG}} < \epsilon_{B_m}$.

- **The variance of the left and right background magnetic field is small compared to the maximum variation of $\mathbf{B_m}$.** Once again, the variance of the background values of Bm contained inside the left and right big window sides should present a variance below a reasonable threshold. The condition will be implemented as $B_{m\,BG} < K^2_{m\,var} \cdot (B_{m\,CORE})^2$, and re-defined as $\widehat{var(B_{m\,BG})} = \frac{var(B_{m\,BG})}{(B_{m\,CORE})^2} < K^2_{m\,var}$. From this definition a restriction related to the magnitude of the Core field $B_{m\,CORE}$ can be implemented. Summarizing, the condition $\widehat{var(B_{m\,BG})} < K^2_{m\,var}$ should be accomplished, where the background refers to either right or left background (must be fulfilled for both separately), and $0 < K_{n\,var} < 1$. The combination of this condition with the previous one assures a proper definition for the background of the signal inside the big window.

- **A clearly defined maximum or a minimum value in the $mathbf{B_m}$ component exists inside the small window region.** The signature of the B_m component should either present a maximum or a minimum value inside of the small window, whose variation from the background value $B_{m\,BG}$ is higher than a certain threshold. Any other local maximum or minimum outside of the small window cannot present a higher variation to the background value than this value. This difference in magnitude represents the core field of a flux rope $B_{m\,CORE}$ and the index representing this position

$N_{B_{m\,CORE}}$ will be considered as the time instant where the flux rope is identified.

$$|B_{m\,CORE}| > K_{m\,CORE} \tag{4.34}$$

- **The peak corresponding to the core field in the $mathbf{B}_m$ component must be located inside the region delimited by the bipolar $mathbf{B}_n$ variation.** In an ideal scenario, the peak corresponding to $B_{m\,CORE}$ should be located exactly in $N_{B_{n\,mid}}$, the sample where the two points of the bipolar variation are equidistant, although in reality this will most likely not happen. The condition introduced to model this situation in a more realistic scenario consists on considering the instant where the peak in B_m is detected $B_{m\,CORE}$ contained between the region delimited by the indexes $N_{B_{n\,MAX}}$and $N_{B_{n\,MIN}}$.

$$N_{B_n\,MAX} > N_{B_m\,CORE} > N_{B_n\,MIN} \quad if \quad N_{B_n\,MAX} > N_{B_n\,MAX} \tag{4.35}$$

$$N_{B_n\,MAX} < N_{B_m\,CORE} < N_{B_n\,MIN} \quad if \quad N_{B_n\,MAX} < N_{B_n\,MAX} \tag{4.36}$$

These four conditions should secure the adequate shape of the B_m component as was previously explained in section 4.2.1. The former two conditions should force the background values of the magnetic field contained inside the big window to stay around a constant value for the time just before and after the flux rope is detected. On the other hand, the two latter conditions consider the existence of a big peak on the B_m component occurring simultaneously with the bipolar variation of the B_n component, and going straightforward back again to the background value. For subsequent analysis, it is also important to separate the detections which present a maximum from those presenting a minimum in B_m, as they will represent positive $B_{m\,CORE} > 0$ or negative

$$B_{m\,CORE} > 0$$

values of the core field respectively. When all the previous conditions match, then the second criterion for detection is also fulfilled and the detection algorithm goes to its last step.

Detection of a maximum or a minimum in the |B| signature. This is the third and last detection criterion to be met. The big window will analyze the behavior of the data correspondent to the background value, while the small window will check for the proper signal shape. The following conditions model this third criterion.

- **Background value of |B| before and after is around a constant value.** Once again the condition for the difference between left and right averaged background values. A certain threshold of acceptance $\epsilon_{|B|}$ is introduced to consider the background value of $|B|$ to be constant when $\overline{\Delta\,|B_{BG}|} < \epsilon_{|B|}$.
- **The variance of the left and right background magnetic field is small compared to the maximum variation of |B|.** One more time the variance condition for the background. The condition will be implemented as $var\,(|B_{BG}|) < K^2_{|B|\,var} \cdot |\Delta B_{max}|^2$, and re-defined as $\widehat{var(|B_{BG}|)} = \frac{var(|B_{BG}|)}{|\Delta B_{max}|^2} < K^2_{|B|\,var}$. The variance restriction is so

connected with the maximum difference on the magnetic field absolute value $|\Delta B_{max}|$. Summarizing, the condition $\widehat{var(|B_{BG}|)} < K^2_{|B|\,var}$ should be accomplished, where the background refers to either right or left background (must be fulfilled for both separately), and $0 < K_{|B|\,var} < 1$.

- **A clearly defined maximum or a minimum value in |B| exists inside the small window region.** The absolute value of the magnetic field should either present a maximum or a minimum value inside of the small window region, whose variation from the background value $|B_{BG}|$ is higher than a certain threshold. Any other local maximum or minimum outside of the small window should not present a higher variation to the background value than this value. This difference in $|B|$ is a consequence of the combined effect of the patterns previously detected in B_n and B_m and it is detected at sample $N_{|B_{max}|}$.

$$|B_{BG}| > K_{|B|} \tag{4.37}$$

- **The instant corresponding to the peak of |B| component must be synchronized with the instant defining the core field.** Since the maximum in $|B|$ is defined by the combined effect of B_n and B_m (and of course B_l) , the peak corresponding to $|\Delta B_{max}|$ should ideally coincide with $N_{B_{n\,mid}}$, where the flux rope's core field $B_{m\,CORE}$ is ideally detected. Nevertheless, in reality this will never happen so precisely, and some misalignment between $N_{B_{m\,CORE}}$ and $N_{|B_{max}|}$ has to be assumed $\Delta N_{miss} = \left|N_{B_{m\,CORE}} - N_{|B_{max}|}\right| \neq 0$. The condition introduced to model this situation in a more realistic scenario consists on considering the instant where $|\Delta B_{max}|$ is detected $N_{|B_{max}|}$, to be close to $N_{B_{m\,CORE}}$ for a defined threshold which is defined as $N_{max\,miss} = \frac{\Delta N_{B_n\,MAX-MIN}}{4}$.

$$\Delta N_{B_{m\,CORE-|B_{max}|}} = \Delta N_{miss} < N_{max\,miss} \tag{4.38}$$

The four conditions modeling this third detection criterion present lot of similarities respect to the ones modeling the second, since both intend to find a peak in the corresponding signal. The two former conditions are common to all three criterions, whose purpose is the definition of a flat constant background value of the signals before and after the characteristic patterns of the flux rope appear. The two latter intend to clearly define a peak on the signal which goes from the background value to an absolute peak value and goes back again to the background, as well as somehow synchronize the instants at which the second and third criterion are fulfilled.

When all three detection criterion are fulfilled for the data contained inside the analysis windows in a certain iteration of the detection algorithm, then a flux rope is considered to be detected and identified in the instant corresponding to $N_{B_{m\,CORE}}$. The verification of the three criterion is realized sequentially, so if at any moment one criterion is not matched, then the analysis for that data is finished and the algorithm shifts the windows to its next position. The non-accomplishment of one single condition will lead to a criterion not being fulfilled, and consequently to the conclusion that any flux rope is located among that data.

The detection criteria will be adjusted empirically taking references from some known flux rope detections which were already shown in other previous works. *[Borg et. al. 2012;*

Teh et. al. 2013][11, 12]. The adjustment of the detection criteria will be realized by defining the values for thresholds and parameters included in the conditions that model the three detection criteria. Those parameters will be adjusted by try and error, until the flux ropes which were identified in these previous works will be detected by the detection algorithm developed for this work. In figures 4.8 and 4.9 is shown how the same flux rope is detected in both situations, although in figure 4.8, the signal measured by spacecraft 3 (green signal) of the magnetic field is a bit ahead of time to the others (around 10 s), while in the source[11] all of the four signals where simultaneously detected. Despite this fact is evident, that the detection algorithm matches perfectly this already known flux ropes.

The whole collection of thresholds and parameters are so determined and the detection algorithm is finally complete, the final values for each parameter are contained in table 4.3.

Window scale	$\epsilon_{\mathbf{\lvert B\rvert}}$ (nT)	$\epsilon_{\mathbf{B_n}}$ (nT)	$\epsilon_{\mathbf{B_m}}$ (nT)	$\mathbf{K_{n\ var}}$	$\mathbf{K_{m\ var}}$	$\mathbf{K_{\lvert B\rvert\ var}}$	$\mathbf{K_n}$ (nT)	$\mathbf{K_{m\ CORE}}$ (nT)	$\mathbf{K_{\lvert B\rvert}}$ (nT)
1	7	7	7	0.4	0.4	0.4	7	8	8
2	7	7	7	0.4	0.4	0.4	7	8	8
3	6	6	7	0.4	0.4	0.4	6	7	7
4	5	5	5	0.4	0.4	0.4	3	3	7
4	4	4	4	0.4	0.4	0.4	2	3	3
6	3	3	3	0.4	0.4	0.4	2	2	2
7	2	2	2	0.4	0.4	0.4	2	2	2
8	2	2	2	0.4	0.4	0.4	1	1	1

Table 4.3: Table containing the parameters defining the conditions of the detection algorithm. Values given in nT, K_{var} non-dimensional.

At this point, the algorithm is completely built, defined and adjusted and only the analysis of the data remains. All the signals correspondent to the events indicated at the beginning of this chapter in table 4.1 have to be now processed by the detection algorithm, and so are the flux ropes (or at least some of them) contained among this data detected.

The next section of this work will consist on the statistical analysis of the whole database of flux rope detections that were registered after all events were analyzed. Once a flux rope is detected, the time instant corresponding to the existence of this is known. Using this instant, the values obtained from CIS can also be accessed to obtain knowledge about the velocity of the Ions at the instant corresponding to the flux rope detection, which will be necessary for the development of further statistical analysis.

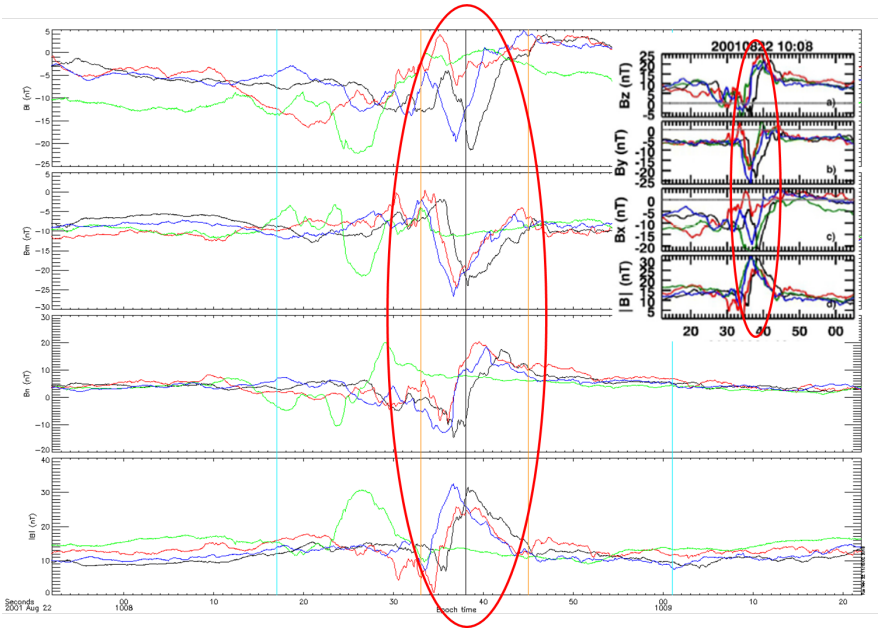

Figure 4.8: Comparison of the flux rope detection on 22 Aug 2001 of spacecraft 1 with the same detection from a previous study[11].

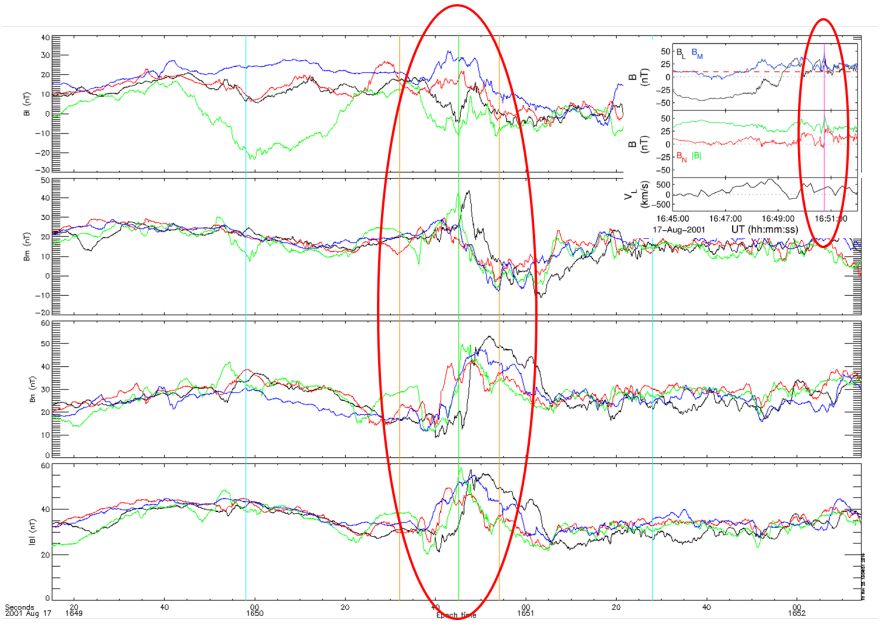

Figure 4.9: Comparison of the flux rope detection on 17 Aug 2001 of spacecraft 3 with the same detection from a previous study[12].

5 Statistical Study

The list of events presented in Chapter 4 was analyzed using the methodology described previously in section 4.3. The selected events are listed below in Table 5.1. In order to avoid falsified statistics, multiple spacecraft detections will be considered as a single flux rope event. The right column shows how much flux ropes were found in each event, while the numbers in brackets represent the total number including multiple detections.

Event Date	**Number of flux rope detections**
17 Aug 2001	1
22 Aug 2001	6 (8)
27 Aug 2001	2
12 Sep 2001	1
1 Oct 2001	2
8 Oct 2001	2
11 Oct 2001	2
8 Oct 2001	1
11 Oct 2001	2
14 Aug 2002	1
14 Aug 2002	1
28 Aug 2002	5
13 Sept 2002	1
18 Sept 2002	1
2 Oct 2003	5
9 Oct 2003	1 (2)
29 July 2003	1 (4)
24 Aug 2003	2
19 Sept 2003	3(6)
4 Oct 2003	1
19 Aug 2004	1
28 Aug 2005	10(11)

Table 5.1: List of all multiple X-line reconnection events analyzed and its correspondent number of Flux ropes detected.

The statistical analysis of flux ropes is the core section of this work. The main objective would be the study of those detected flux ropes for a better understanding of its nature. The analysis consists of different statistical studies:

Spatial location of the flux ropes relative to the X-line.

Location on the earthward or tailward side of the X-line and direction of rotation of the flux rope's magnetic field.

Factors that influence the polarity of the core field related to a flux rope $B_{m\,CORE}$:

- Relationship between the Hall field in the vicinity of the X-line and the Background magnetic field of the B_m component of the flux rope.
- The relationship between the Core field of the flux Rope $Bm\,CORE$ and this previously mentioned Hall field shown on the Background B_m.
- Influence of the existing guide field on an event over $Bm\,CORE$

A database of flux ropes including all its properties was generated while all events were analyzed with the detection algorithm. Table 5.1 shows the date and time of all registered detections. The spacecraft number which registered the detection is shown, while multiple spacecraft detections are marked as *MSC*. In total there are 62 registers, which are reduced to 52 due to suppression of multiple spacecraft detection.

Detection number	**Flux rope time**	**Cluster spacecraft**	Δt [s]	ΔB_n [nT]	$\Delta B_{m\,CORE}$ [nT]
1	2001-08-17 | 16:50:44:947	3	6.2899160	38.676338	29.270420
2	2001-08-22 | 10:08:38:214	1	5.0844307	31.311666	18.037344
3	2001-08-22 | 10:08:26:484	3(MSC)	5.0844307	31.311666	18.037344
4	2001-08-22 | 10:08:36:653	4(MSC)	5.0844307	31.311666	18.037344
5	2001-08-22 | 09:52:15:358	2	3.2112193	9.0240002	5.5521703
6	2001-08-22 | 10:04:20:335	2	3.1220188	9.3430004	7.0385642
7	2001-08-22 | 09:43:47:539	1	1.4718089	5.6919994	3.0399632
8	2001-08-22 | 09:42:48:622	3	1.6502100	25.500999	20.425009
9	2001-08-22 | 09:56:13:300	1	1.2934078	21.881001	18.777462
10	2001-08-27 | 04:03:09:721	4	6.7792029	14.674999	5.5052280
11	2001-08-27 | 04:02:23:828	1	2.7503345	8.2979994	3.8965206
12	2001-09-12 | 13:15:14:445	3	24.797707	33.991776	18.376936
13	2001-10-01 | 09:54:55:146	4	2.4976277	8.8969994	4.9841447
14	2001-10-01 | 09:40:02:824	2	0.75820839	7.4349999	4.2165709
15	2001-10-08 | 13:02:37:196	4	2.9436688	11.231000	7.9503698
16	2001-10-08 | 13:11:32:498	2	0.84741986	4.5159998	2.6445026
17	2001-10-11 | 03:27:58:185	2	3.6126845	11.941999	9.3286114
18	2001-10-11 | 03:28:51:885	3	2.5868607	6.0710001	7.7108417
19	2002-08-14 | 03:12:52:307	3	0.84741569	2.7391696	1.7447004
20	2002-08-14 | 04:09:28:359	4	5.7534246	8.7449045	8.9480667
21	2002-08-14 | 04:13:17:292	2	2.4530106	6.6778779	5.4256115
22	2002-08-28 | 10:15:24:383	3	53.208618	25.540361	20.567232
23	2002-09-13 | 18:13:55:678	3	1.9624084	4.8854847	5.1746855
24	2002-09-18 | 13:53:13:410	3	18.704803	14.730455	19.087109

25	2002-09-18 | 13:36:29:162	2	9.0758963	22.155777	14.516999
26	2002-09-18 | 13:24:55:393	2	3.3505998	8.3842688	6.2952347
27	2002-09-18 | 13:37:02:180	1	2.3096366	5.3687849	4.8283424
28	2002-09-18 | 13:36:46:500	2	1.8216852	9.0740728	3.4677429
29	2002-10-02 | 21:32:28:907	1	1.9624362	10.868000	4.6863632
30	2002-10-26 | 09:31:16:161	4	5.3088479	10.809498	4.6359549
31	2003-10-02 | 00:51:41:402	2	7.6267695	19.077999	8.7845030
32	2003-10-02 | 00:58:32:534	2	4.2370944	11.145000	3.8197041
33	2003-10-02 | 00:29:40:409	1	2.2300496	8.3090000	4.2483902
34	2003-10-02 | 01:02:24:414	1	2.4084535	6.6409998	6.7761316
35	2003-10-02 | 01:03:48:264	2	0.44600987	2.6090000	2.1019340
36	2003-10-09 | 02:29:05:907	2	8.2734938	14.375500	11.099549
37	2003-10-09 | 02:29:05:149	4(MSC)	8.2734938	14.375500	11.099549
38	2003-07-29 | 18:26:19:135	1	18.356651	26.302250	19.369665
39	2003-07-29 | 18:26:19:670	2(MSC)	18.356651	26.302250	19.369665
40	2003-07-29 | 18:26:19:358	3(MSC)	18.356651	26.302250	19.369665
41	2003-07-29 | 18:26:18:585	4(MSC)	18.356651	26.302250	19.369665
42	2003-08-24 | 18:42:49:526	4	1.0258087	8.5799999	6.5049429
43	2003-08-24 | 18:44:29:386	3	0.57980490	8.7010002	4.0395894
44	2003-09-19 | 23:45:27:530	1	12.622189	18.254749	17.443525
45	2003-09-19 | 23:45:27:619	2	12.622189	18.254749	17.443525
46	2003-09-19 | 23:45:27:128	3	12.622189	18.254749	17.443525
47	2003-09-19 | 23:45:27:262	4	12.622189	18.254749	17.443525
48	2003-09-19 | 23:48:09:120	2	1.5164468	6.6550002	2.9285934
49	2003-09-19 | 23:31:18:409	4	0.93662894	8.1980000	8.6219978
50	2003-10-04 | 06:28:18:998	1	7.5821142	16.023552	5.8188500
51	2004-08-19 | 18:09:18:782	1	7.3591099	11.659414	9.1916943
52	2005-08-28 | 23:46:30:400	1	37.509594	24.096849	28.157543
53	2005-08-28 | 23:54:12:226	2	10.079867	32.626884	18.587519
54	2005-08-29 | 00:01:02:308	1	4.1925111	17.236973	9.6233015
55	2005-08-29 | 00:02:24:642	2	3.4342911	9.3451233	3.1963947
56	2005-08-28 | 23:40:15:705	4	4.9953327	19.072775	6.8500152
57	2005-08-28 | 23:47:31:133	1	2.8544755	18.048285	9.5965462
58	2005-08-28 | 23:50:04:530	1	2.6314697	12.749804	14.892418
59	2005-08-28 | 23:40:35:642	2	1.3826365	7.1665740	3.6528001
60	2005-08-28 | 23:55:25:436	1	1.7394462	8.4055843	7.2493906
61	2005-08-28 | 23:40:35:642	2	1.3826365	7.1665740	3.2845469
62	2005-08-28 | 23:55:53:579	1	0.84742260	5.1555996	1.5317354

Table 5.2: Some Flux Rope important properties and instant of detection.

The database of flux ropes contains all the necessary information for the statistics. Several statistical studies will be carried on, those are the following:

Histogram for flux rope length: Characterization of the flux ropes by means of its

duration in seconds.

Superposed Epoch Analysis: Normalized representation of similar types of flux ropes superposed.

Length-size correlation: The relationship between length *(s)* and size *(nT)* of the flux rope will be analyzed.

$\mathbf{B_n}$ Component- $\mathbf{V_{HIA}}$ and $\mathbf{V_{H^+}}$correlation: B_n and the particle velocities will be examined for correlation.

$\mathbf{B_n}$, $\mathbf{V_{HIA}}$ and $\mathbf{V_{H^+}}$ vs. $\mathbf{B_l}$ maps (Guide and no-Guide Field $\mathbf{B_m}$) with $\mathbf{B_{m\,CORE}}$: Position map of all flux ropes relative to its nearest X-line. The two cases with and without guide field of the B_b component are considered, $B_{m\,CORE}$ polarity is also shown.

Distance vs. $\mathbf{B_l}$ map (Guide and no Guide Field $\mathbf{B_m}$) with $\mathbf{B_{mCORE}}$: Position map of all flux ropes relative to its nearest X-line where measured data from X-line is available. The polarity $B_{m\,CORE}$ is also represented.

$\mathbf{B_n}$, $\mathbf{V_{HIA}}$ and $\mathbf{V_{H^+}}$ vs. $\mathbf{B_l}$ maps with polarity change of $\mathbf{B_n}$: Position map of all flux ropes relative to its nearest X-line, B_n polarity and amplitude is also shown, additional study switching amplitude for length.

Distance vs. $\mathbf{B_l}$ map with Polarity change of $\mathbf{B_n}$: Position map of all flux ropes relative to its nearest X-line where measured data from X-line is available. $B_{m\,CORE}$ polarity and amplitude is also shown. An additional study switching amplitude for length will also be realized.

Each of those statistics focuses on the analysis of one different aspect of the flux rope's nature. The motivation and purpose of each statistical study will be subsequently explained in each correspondent subsection.

5.1 Histogram for flux rope length

As a first study, the collection of 52 flux ropes identified on the 31 multiple X-line reconnection events are classified in terms of duration. The criteria to determine whether the combined lectures of B_m , B_n and $|B|$, were considered flux ropes or not, was not restrictive with the length of the flux rope. This means, flux ropes from different lengths could be found among this collection. The length of a flux rope is defined as the Δt between the maximum *(minimum)* and the minimum *(maximum)* of B_n. Later in this work will be analyzed that the length of a flux rope and its size, defined as the peak-to-peak value in magnitude of the B_n component are up to some degree correlated. How the length is distributed among the detected flux ropes is represented in the histograms shown in figures 5.1 and 5.2.

The histograms of Figures 5.1 and 5.2 show that most of the detected flux ropes present

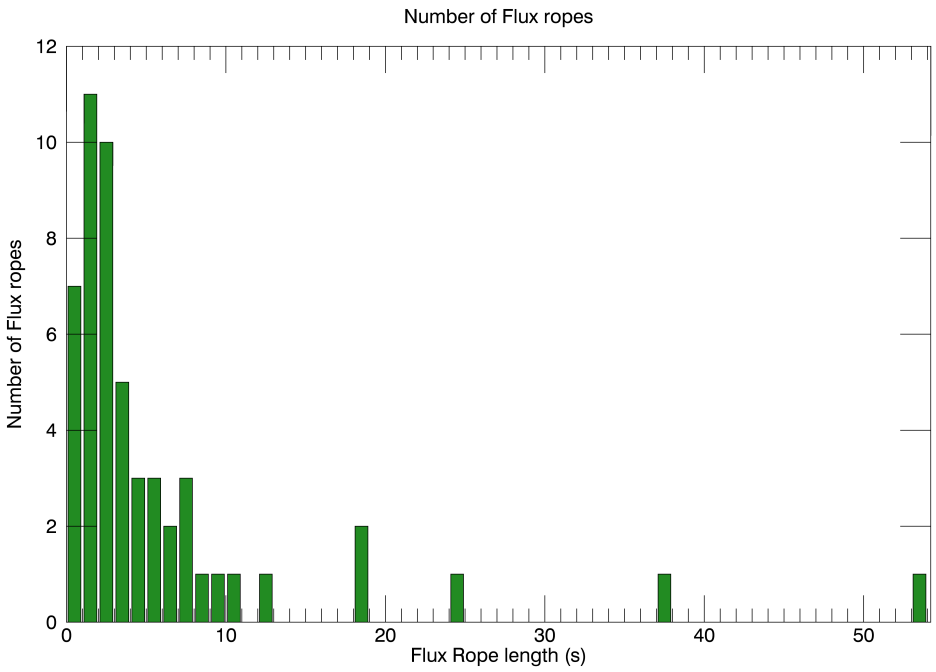

Figure 5.1: Histogram representing the number of flux ropes detected for a determined duration in seconds.

a duration shorter than 25 seconds, being only two detections above this value. The concentration of flux ropes is specially high for durations below 10 seconds, where 75 % of the detections are characterized by a short duration below six seconds. The maximum number of detections is registered for very short durations between one and three seconds.

In light of these results it can be interpreted, the detection algorithm is much more restrictive with the magnetic field patterns which characterize big flux ropes than for the small scale. Big scale flux ropes with lengths of $\approx R_E$ are characterized by a more turbulent nature than the small ones. Due to this more turbulent nature, the magnetic field components for the former may contain high magnitude fluctuations, which may easily violate some of the conditions for flux rope detection implemented in the detection algorithm. On the other hand, small scale flux ropes characterized by lengths much smaller than R_E, usually contain fluctuations of lower magnitude, since its nature is not as much turbulent as it is for big flux ropes. This less turbulent nature of the small flux ropes makes it easier to match the designed conditions of flux rope detection. The criteria used for the automatic detection of the flux ropes were previously explained in section 4.3.2.2.

The order of magnitude in terms of duration is important for the better understanding of these results. Even though the results where up to now differentiated as *short*, *very short*, *big*

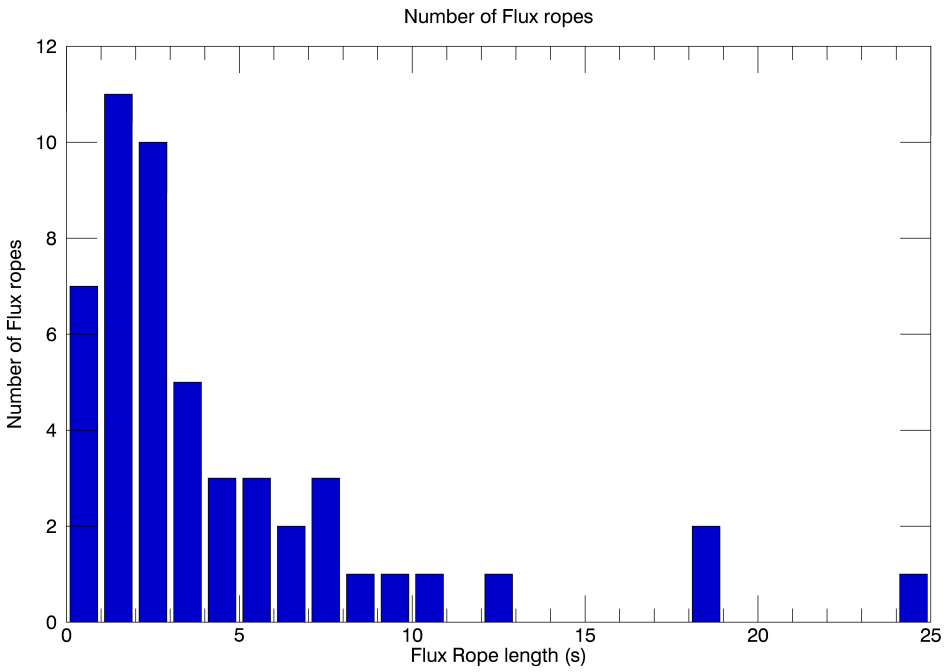

Figure 5.2: Histogram representing the number of flux ropes detected for a determined duration in seconds. The region of higher flux rope concentration is shown here.

or *small*, actually all of the registered flux rope detections have a short duration compared with other structures like flux ropes correspondent to the plasmoids *[Baumjohann; Treumann, 1996]*[3] commented in section 2.4. As previously explained, such structures are originated during multiple X-line reconnection events on the tailward side of the magnetotail, when reconnected magnetic field lines form an enclosure, this was previously shown in Chapter 2 Figure 2.11. The size of such structures extends to the order of $\approx R_E$ or even more, presenting durations during a spacecraft crossing some orders of magnitude above the values that were registered for the flux ropes in this analysis.

This work should focus on the study of the nature and properties correspondent to small scale flux ropes. In view of the results shown in figures 5.1 and 5.2 was concluded that the vast majority of flux ropes detected correspond to this family of small scale flux ropes, this is why they are referred in relative terms of duration as *short* or *long*, regardless of having all of them a brief duration. The fact that the majority of detections correspond to small scale flux ropes is a very interesting result from this first statistical study. It is also an indicator of the good performance of the detection algorithm for the flux rope structures on which this study is oriented.

5.2 Superposed epoch analysis

While in the previous section, all flux ropes were classified in terms of duration, here the focus will be the topology of those structures.

This section is intended to present the characterization of the flux ropes selected in the database. There are many parameters that are characteristic of the flux ropes: shape of the magnetic field components, magnetic pressure, plasma pressure or plasma β parameter, among others. Particularly for this study, only the shape of the magnetic field components B_z (B_n), B_y (B_m), and $|B|$ are used, according to the model[**?**] discussed in section 4.2.1.
A superposed epoch analysis is a proper method to represent each different types of flux rope referring to the shape of its magnetic field components. There are mainly four different types of flux rope typologies among the selected events in the database, those are:

Case 1: B_z (B_n) component oscillation showing a minimum and then a maximum from less positive to more positive values and a maximum in B_y (B_m).

Case 2: B_z (B_n) component oscillation showing a minimum and then a maximum from less positive to more positive values and a minimum in B_y (B_m).

Case 3: B_z (B_n) component oscillation showing a maximum and then a minimum from more positive to less positive values and a maximum in B_y (B_m).

Case 4: B_z (B_n) component oscillation showing a maximum and then a minimum from more positive to less positive values and a minimum in B_y (B_m).

All of them show a maximum on the $|B|$ component, as expected based on the model [**?**]. The interpretation related to each typology was previously explained in Chapter 2, when the model was presented.

It is important to highlight, that due to the different duration of flux ropes, a normalization of the data is indispensable. For the normalization, half the duration of the peak-to-peak variation on the $B_z(B_n)$ component is used $c_{norm} = \frac{|\tau_{B_n\,min} - \tau_{B_n\,min}|}{2}$, so that the separation of the peak-to peak is represented by a non-dimensional unit $\frac{s}{s}$. The same parameter c_{norm} will be used to normalize the amplitude of the flux ropes, referring to the amplitude as the difference in magnitude *(nT)* between the minimum and the maximum value of the B_n component $|B_{n\,min} - B_{n\,min}|$, so that the flux ropes are only scaled, without distorting its shape. Finally, the background magnetic field is suppressed in each component, so that all flux ropes are biased to be around 0 as shown in the following set of equations:

$$B_{n\,BIAS} = B_n - \overline{B_{n\,total\,BG}} \tag{5.1}$$

$$B_{m\,BIAS} = B_m - \overline{B_{m\,total\,BG}} \tag{5.2}$$

$$|B_{BIAS}| = |B| - \overline{|B_{total\,BG}|} \tag{5.3}$$

The superposed epoch analysis for the different flux rope typologies are shown below, where the maximum and minimum values on the B_n component where fixed to -1 and 1 respectively. Another superposed epoch analysis where B_m is fixed as reference at 0 value can be found at the end of this work in Appendix D.

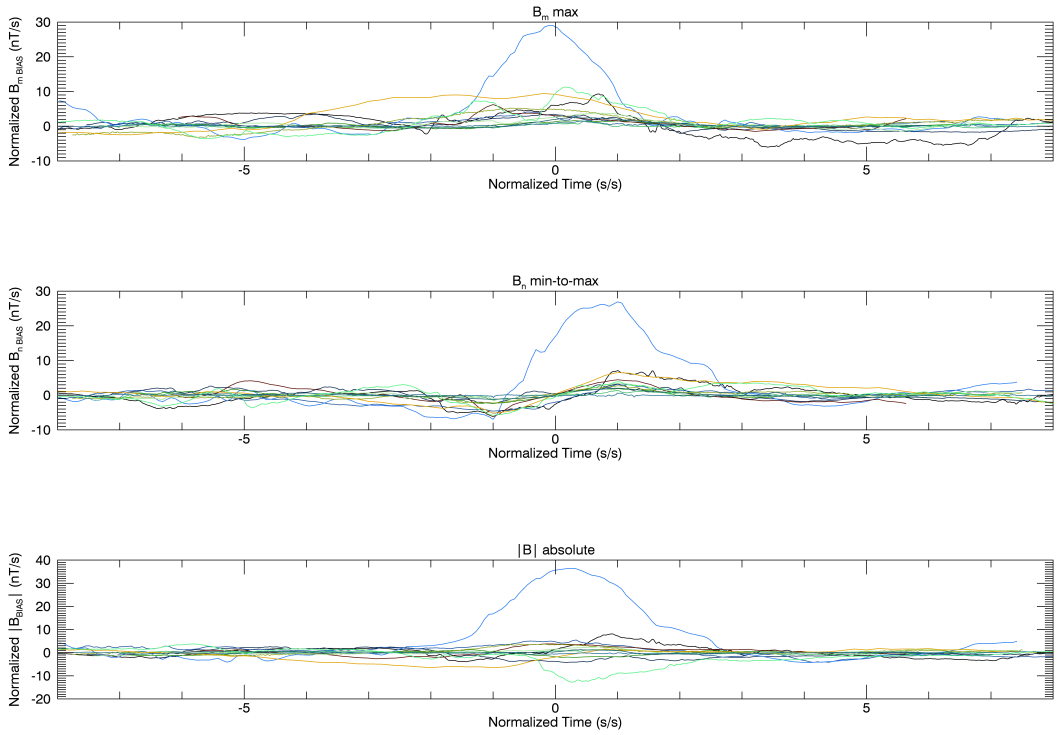

(a) Case 1 - Full range

Figure 5.3: First of 2 figures representing **case 1**.

Figures 5.3a and figure 5.3b show a superposed epoch analysis for the flux ropes as described in *case 1*, this means, a minimum then a maximum in the B_n component, and a maximum in the B_m component. As can be seen in Figure 5.3a the represented ropes have a shape on its components which is coherent with the model commented in section in section 4.2.1. All of them show an oscillation on the B_n lecture from a minimum to a maximum and have a maximum on the B_m component in between the oscillation of B_n as expected. The scaling in Figure 5.3a is adjusted to the biggest flux rope, existing one with much bigger amplitude than the rest. For a better overview of the main block of flux ropes registered for this case, a scale adjustment was realized and shown in Figure 5.3b. In this last mentioned figure, a remarkable similarity between most of the B_n components from the different flux ropes for this case can be appreciated.

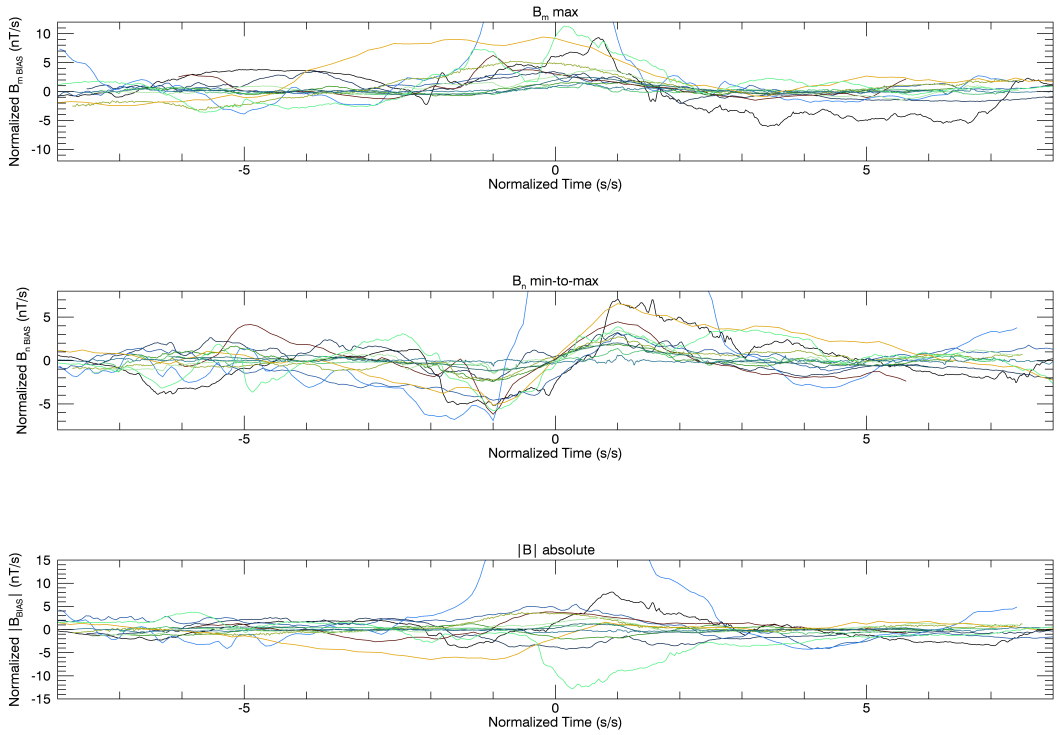

(b) Case 1 - Reduced range

Figure 5.3: Second of 2 figures representing **case 1**. The range of values in figure 5.3b is zoomed referring to figure 5.3a

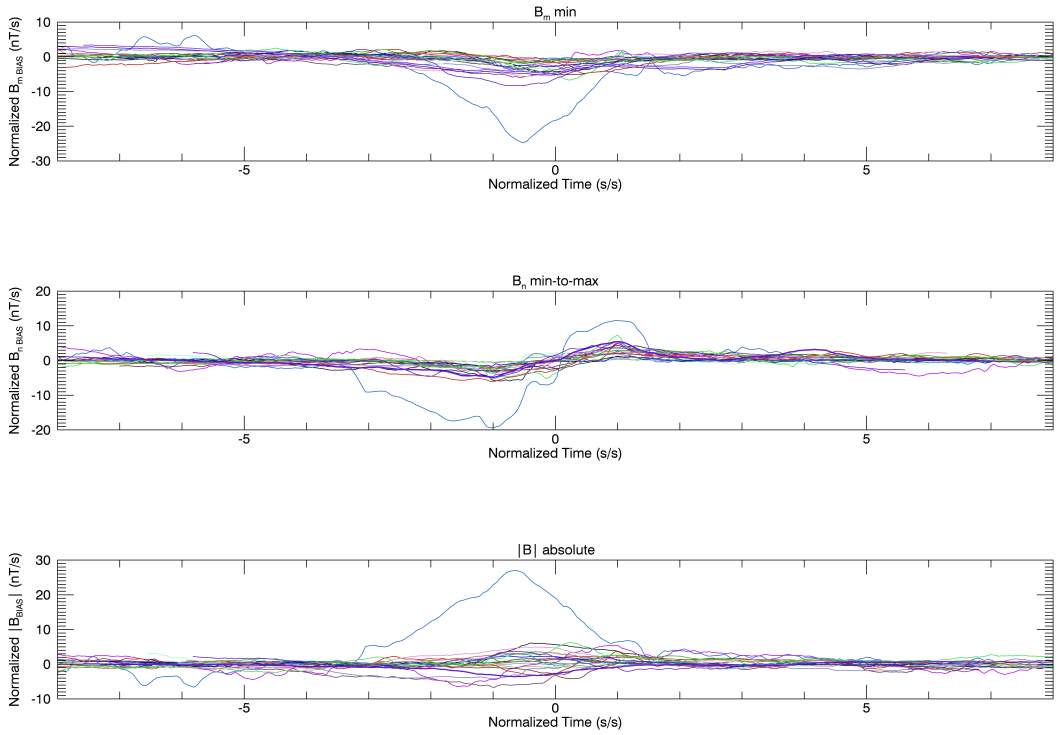

(a) Case 2 - Full range

Figure 5.4: First of 2 figures representing **case 2**.

In figures 5.4a and 5.4b, a superposed epoch analysis of the typology referred previously in this section as *case 2* is shown. As occurred also on the superposed epoch of *case 1*, there is one flux rope with much bigger amplitude of the peak-to-peak Bn component, than the rest, for this reason, a scale adjustment was realized in Figure 5.4b in order to achieve a better representation of the remaining flux ropes, which have similar proportions. The flux ropes this group comprises have its magnetic field components clearly defined and coherent according to the model followed. In almost each one of the represented flux ropes, a bipolar variation on the B_n component from a minimum to a maximum value can be clearly appreciated, while local minima are also represented in the B_m component relatively clear. The shape of the $|B|$ component is not as clear as should be expected, but still is possible to recognize peaks of local maxima between the duration of the bipolar variation of the ${}_{B}n$ component. All together it could be said, that the flux ropes comprehended in this group have a good degree of coherency with what was expected to be encountered.

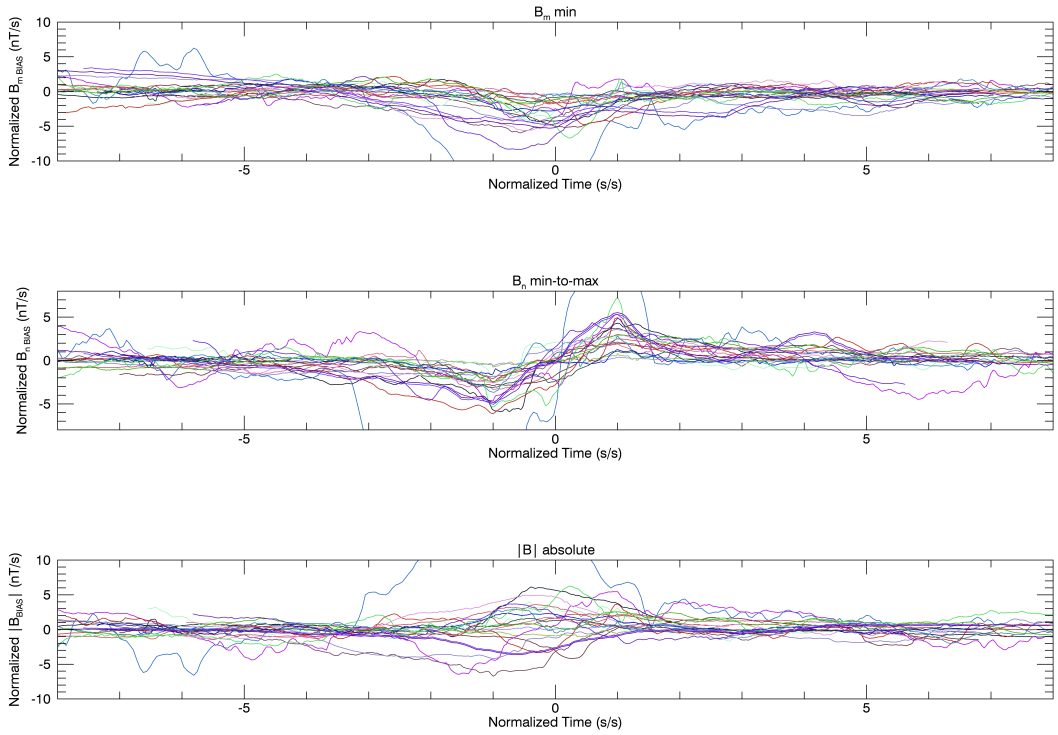

(b) Case 2 - Reduced range

Figure 5.4: Second of 2 figures representing **case 2**. The range of values in figure 5.4b is zoomed referring to figure 5.4a

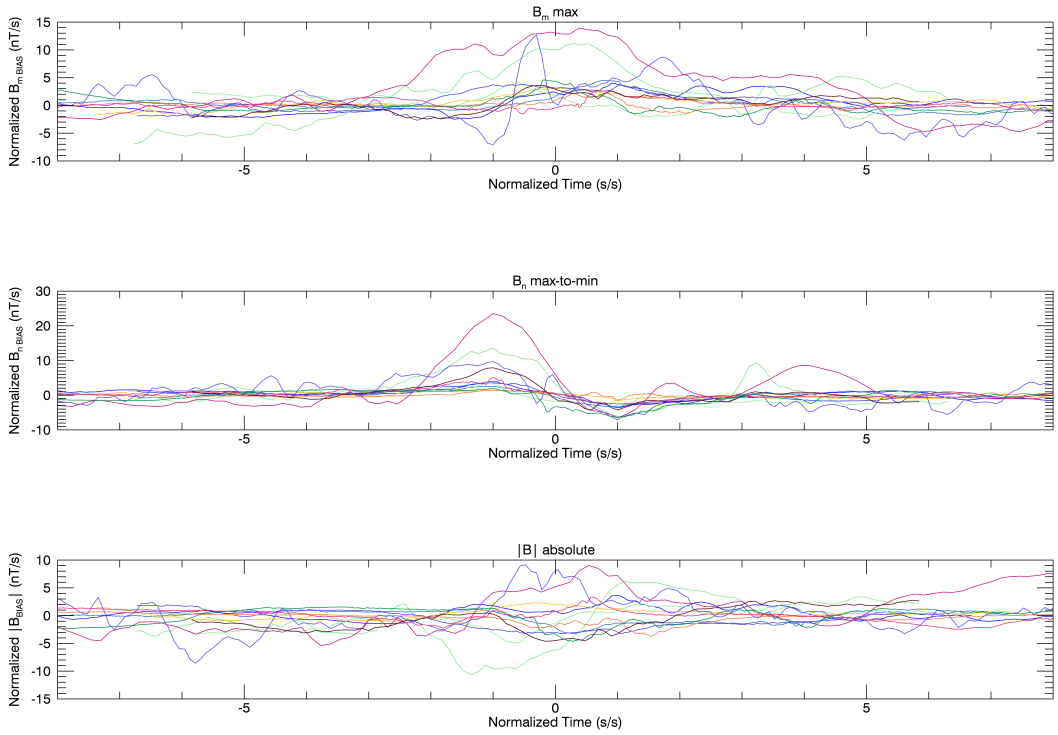

(a) Case 2 - Full range

Figure 5.5: First of 2 figures representing **case 3**.

The above shown figures 5.5a and 5.5b represent the superposed epoch analysis of the flux ropes referred to as *case 3*. Same as happened in the previous superposed epoch analysis, there are some registers that distance a bit on the proportions compared to the rest. For this reason, a scale adjustment was realized one more time and shown in figure 5.5b, the three flux ropes represented which have bigger magnitude than the rest can be clearly appreciated in Figure 5.5a.Even though the magnetic field components are coherent with the model, there exist some anomalies in the shape of some of the registers which should not be ignored. While for the flux ropes seen in Figure 5.5b the components show a relatively good approach to the patterns that were expected, for the ones excluded from Figure 5.5a there are some curious patterns. Among these anomalies one can notice much bigger amplitude of one side of the oscillation of the Bn component than from the other, or some weird oscillations on the B_m component, despite this not so "ideal" shapes, the detections are fulfilling the requirements the detection algorithm is imposing, so they would still be considered as flux rope detections in this work. The criteria imposed and implemented for the development of the detection algorithm was previously explained in detail in section 4.3.2.2.

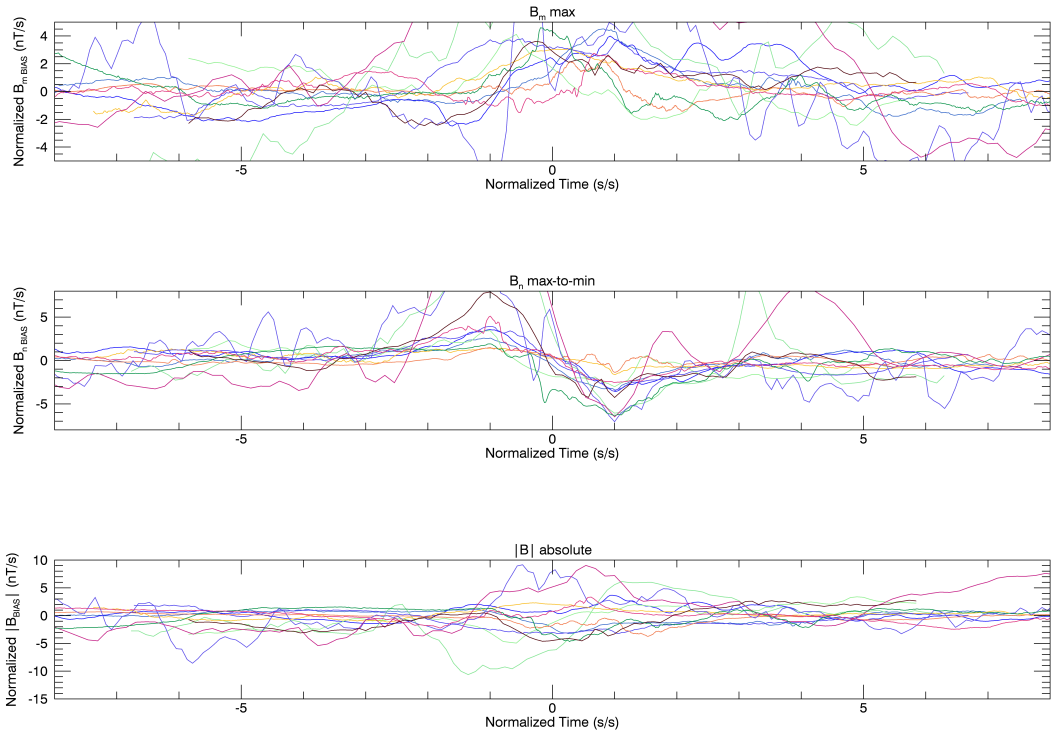

(b) Case 3 - Reduced range

Figure 5.5: Second of 2 figures representing **case 3**. The range of values in figure 5.5b is zoomed referring to figure 5.5a

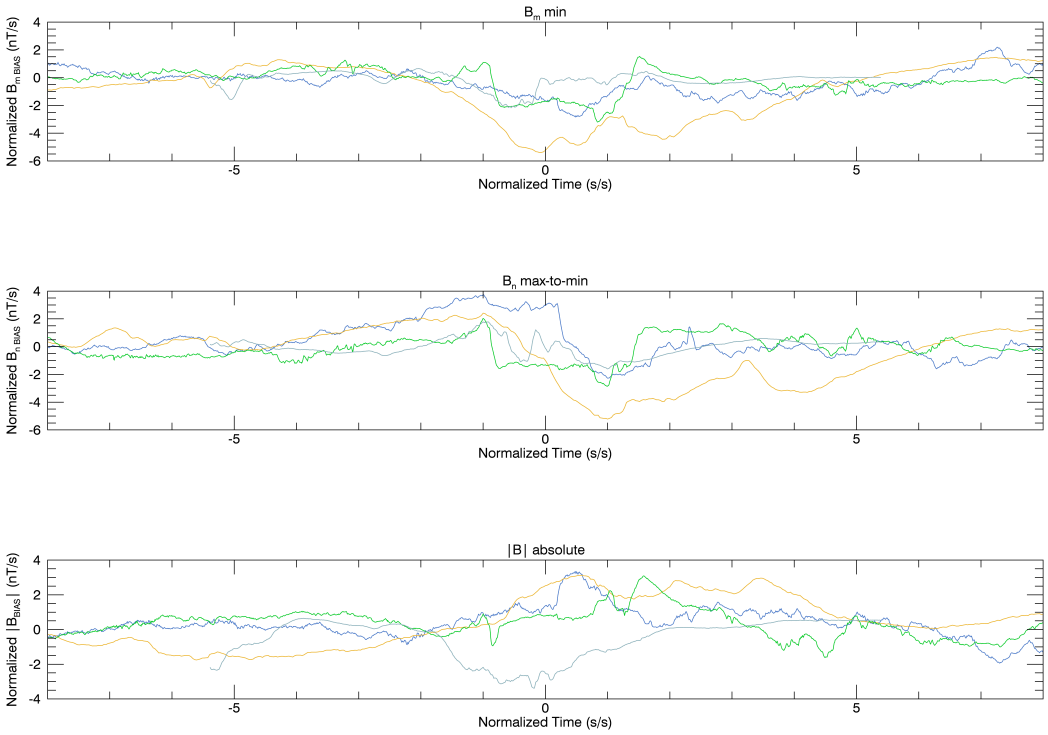

Figure 5.6: Figure representing **case 4**.

The last of the four superposed epoch analysis represent the flux ropes of the group which was previously named as *Case 4*. There are only 4 detections contained in this group, and all of them have similar proportions, so no scale adjustment will be needed here, the results of the superposed epoch for this case can be seen in Figure 5.6. This group of flux ropes is showing at the same time good coherency with the model and some degree of uncertainty. Excluding the green signal, the bipolar variation on the B_n components and the minimum in the B_m are relatively well defined. However, the green signature is showing an especially weird variation of the B_n component, with a hole-like shape comprehending the duration of the bipolar variation, while a similar hole of constant value is shown in the B_m component. This could lead to the question of this is really a flux rope, or just another type of magnetic structure, nevertheless it was previously assumed, that all detections registered processed by the detection algorithm will be in first approach treated as flux ropes for the purpose of this thesis.

5.3 Amplitude and duration of the flux ropes

In this section duration and amplitude of the flux ropes will be examined together based on the 2D-model for flux rope detection used to develop the detection algorithm. Duration is understood as the peak-to-peak time difference on the B_n magnetic field component, while

amplitude refers to the peak-to-peak difference in magnitude of the same component. Based on the shape and structure that should characterize the magnetic field components of a flux rope, it seems coherent to think, there will be a correlation between duration and amplitude (duration in seconds and amplitude in nT respectively) on the B_n signature of the flux rope.

Plotting the values of both parameters in a scatterplot will show whether this tendency is real or not, and give some interesting information for a better understanding of the nature of these structures, the result is shown in figures 5.7 and 5.8.

Figure 5.7 shows the values of duration and amplitude of all flux ropes. The minimum quadratic linear regression line is calculated related to this data, and can be appreciated, that a linear correlation does not fit well for the whole sample of data. However, it appears to exist a pattern close to linear correlation for the very short time structures, becoming more damped as duration continue increasing and adopting for long duration values a behavior closer to logarithmic than linear, but in any case, increasing figure 5.8 is showing the scatterplot for flux ropes with durations shorter than 6 seconds, and its corresponding linear regression line. Most of the flux ropes among the database used for this work have duration lower than 6 seconds; this can be corroborated with the histogram previously shown in figure 5.2. For this range of durations, the linear regression line shows a pattern that fits much better with a linear correlation between both parameters, verifying what was previously foreseen in figure 5.7.

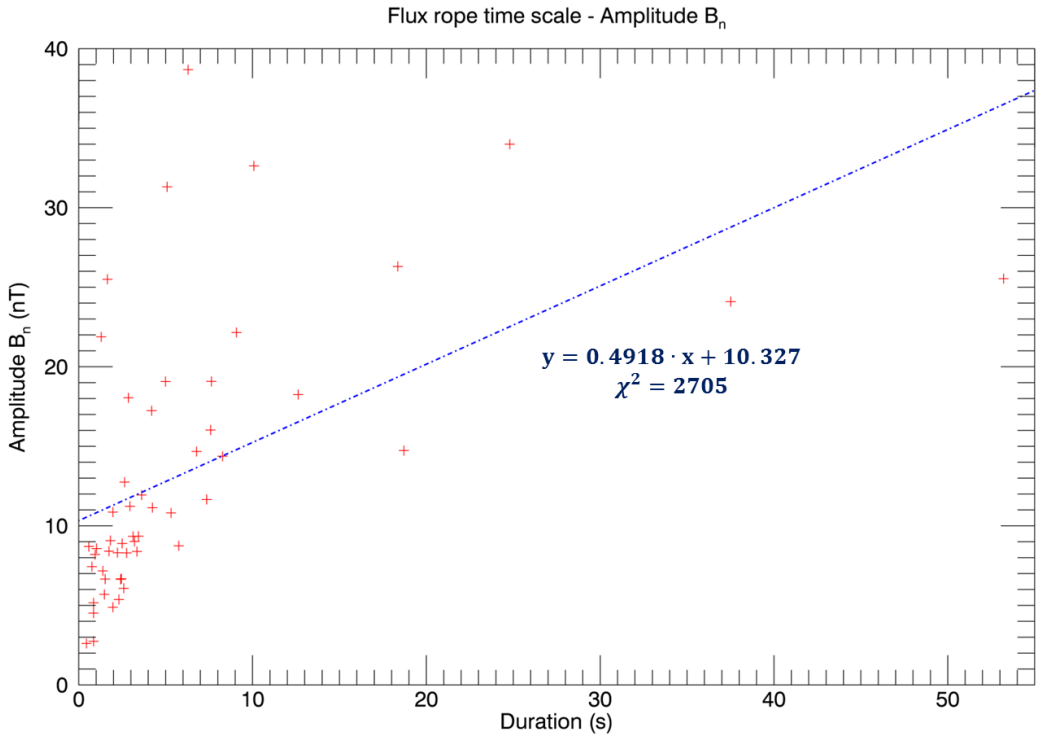

Figure 5.7: Scatterplot representing duration *(s)* and amplitude *(nT)*. Correlation between the two parameters can be appreciated.

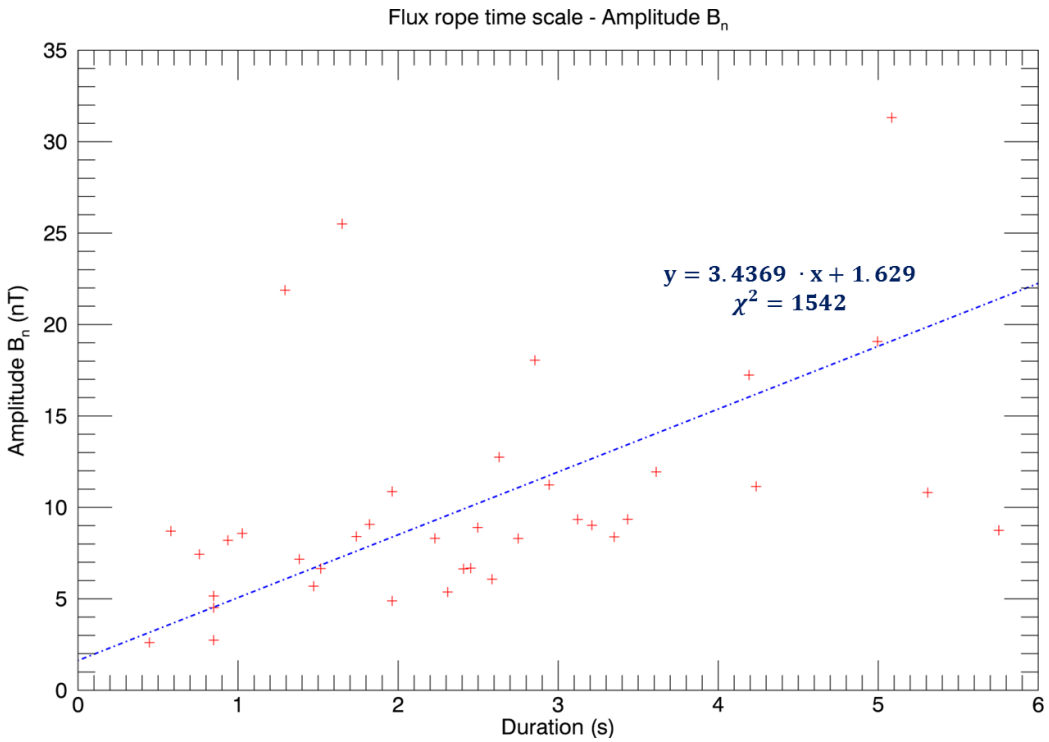

Figure 5.8: Scatterplot representing duration *(s)* and amplitude *(nT)*. Only data below 6 seconds is evaluated.

Just as shown in Figure 5.2 of the previous section, not many long duration flux ropes were detected, therefore would be complicated to make a solid conclusion of the correlation between duration and amplitude for this range of values. However, plenty of small scale detections are available, so it would make sense to focus particularly on this data for this section. A relatively solid conclusion about the correlation between length and size of the flux rope structures can be determined, at least for this range of durations.

5.4 Dependency between B_n and $V_{l\,HIA}$-$V_{l\,H^+}$

From the list of events which were used for this statistical study, only a part of them include information about the velocity and instant regarding an X-line, which means, the distance between the flux rope and the X-line cannot be directly calculated for each single flux rope detection. An alternative method for representing the spatial distribution of flux ropes, when any of the previously mentioned information is available, could be the use of the parameters B_n, $V_{l\,H^+}$ $V_{l\,HIA}$. B_n and V_l are equal zero in the center point of the X-line and they become more positive while directing earthwards (positive direction of magnetic field lines and plasma outflow) while more negative when tailwards (negative direction). This is based on the phenomena occurring during the formation of an X-line, which is shown in 5.9. The whole description of the X-line formation process was explained in section 2.2.1 of Chapter 2.

LMN Coordinates are achieved through a minimum variance analysis of the spacecraft data in GSE coordinates, as was previously explained in section 4.2.2, the positive L direction is directed earthwards, while the negative does it tailwards, positive N is south-north oriented.

The B_n component of the magnetic field could be used as a good indicator for representing the relative location of flux ropes in the vicinity of an X-line. The flux rope is either located earthwards for positive background values of B_n or tailwards for negative B_n values of the background magnetic field. This assumption is based on the typology of the magnetic field lines at the earthward (south-north directed) and tailward side (opposite direction) of an X-line after magnetic reconnection occurs, as clearly shown in figure 5.9.

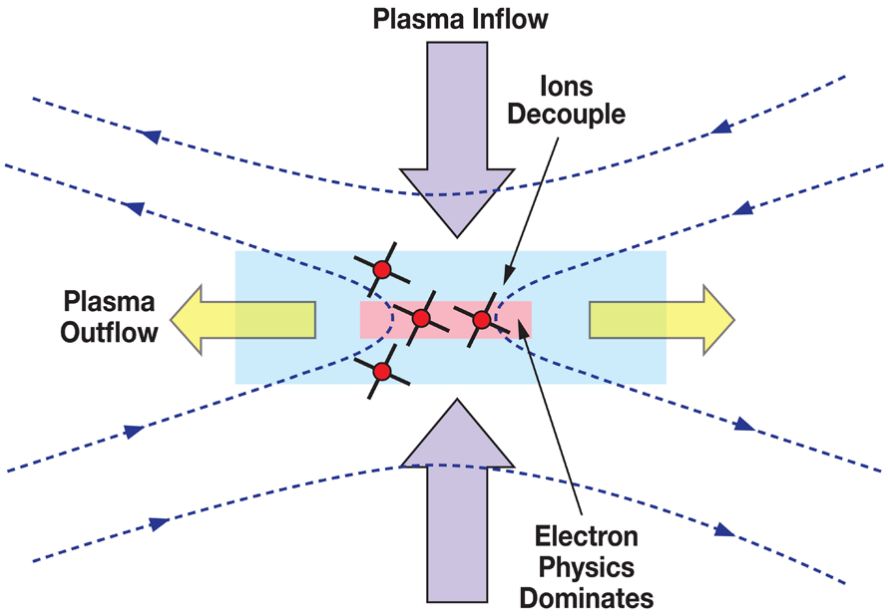

Figure 5.9: Magnetic typology in the vicinity of the X-line after magnetic reconnection[29].

When magnetic reconnection on the magnetotail near the current sheet occurs, the B_n component is zero in the center of the X-line, and the *frozen-in* condition of the magnetic tubes is violated, mixing up different plasmas and generating outflow streams (earthward and tailward), as shown in Figure 5.9. Therefore, B_n can be used as an indicator of how far is the flux rope relative to the position of X-line. It will tend to zero if the flux rope is really close to the X-line, and bigger in magnitude with larger distance. The sign of the background B_n component will indicate if it is on the earthward (positive) or tailward (negative) side of the X-line. A detailed explanation about X-lines and the frozen-in condition and its violation while magnetic reconnection occurs was previously given in Chapter 2.

Regarding the previously mentioned outflow streams,the V_l component would also represent the position of a flux rope relative to the neighboring X-line in a similar way than did the background value of B_n, being V_l also zero in the center of the X-line as previously commented. The measurements of velocities obtained through the CIS (Cluster Ion Spectrometer) gave information about protons H^+ and all ion families *HIA* being those referred as $V_{l\,H^+}$ and

$V_{l\,HIA}$ respectively.

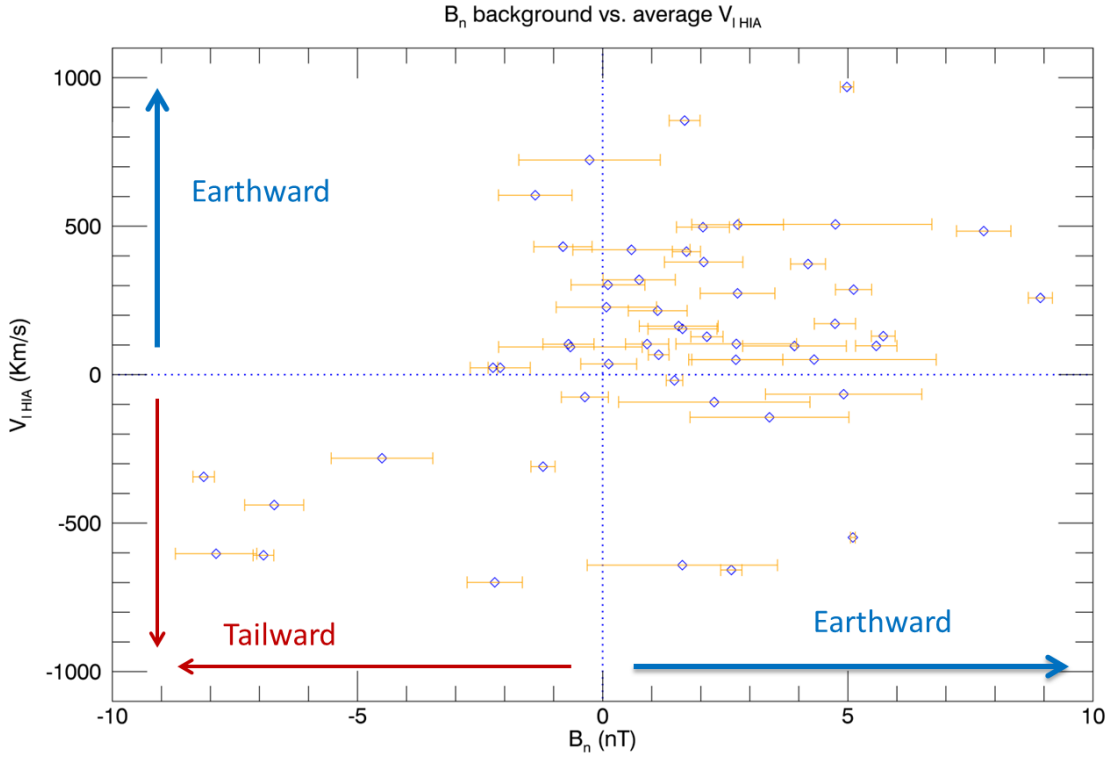

Figure 5.10: Scatterplot showing B_n background and average $V_{l\,HIA}$ for every flux rope detection.

At the center of the X-line, where magnetic reconnection occurs, the particles have zero velocity in L direction (frozen-in-plasma). There exists an inflow of particles through the upper lower side of the X-line, and an outflow on the left-right side, being this left-right side (theoretically) aligned with the L direction. Particles will then have higher velocities as they get far away from the X-line, being so an indicator of how far is a flux rope located relative from the neighboring X-line.

So far the validity of B_n and V_l as indicators of the X-line's positions was justified. Furthermore, as both parameters should give a representation of the same reality, they should be exchangeable and it should be able to refer to one or the other without uncertainty.In order to use them indistinctly it should be checked the existence of a considerable degree of correlation between both parameters.

Figures 5.10 and 5.11 show the scatterplot of B_n and $V_{l\,HIA}$ and $V_{l\,H^+}$ respectively. The background values of the magnetic field component B_n and the average value of V_l are represented with diamonds, the error bars represent the characteristics minimum and maximum values of the B_n component. The blue *(red)* arrows indicate an earthward *(tailward)* position characterized by the value of the parameters B_n and V_l.

In Figure 5.10, B_n and $V_{l\,HIA}$ present some degree of correlation among them. Higher

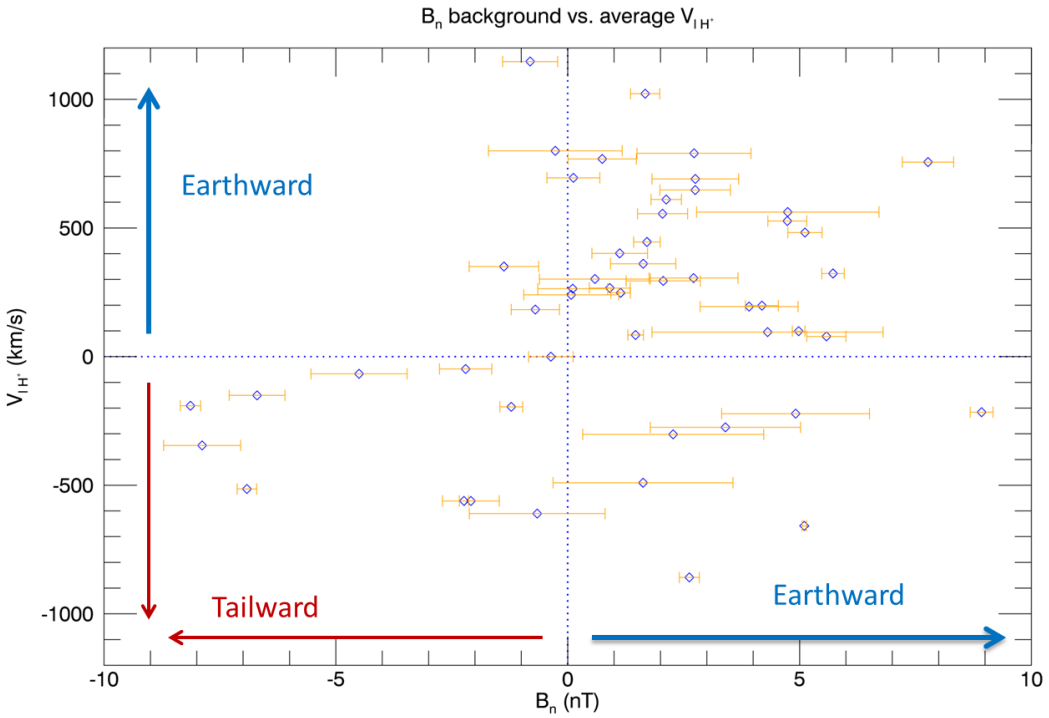

Figure 5.11: Scatterplot showing B_n background and average $V_{l\,H+}$ for every flux rope detection.

positive (negative) values of one parameter lead to higher positive (negative) values of the other parameter and same for lower values. Although the correlation is not absolutely clear and some scattering of the values can be appreciated, it will be concluded it correlates well enough, so that the use of both parameters indistinctly as an auxiliary indicator of the relative distance to the X-line is justified.

Figure 5.11 shows also a certain degree of correlation between B_n and $V_{l\,H+}$, although as happened in Figure 5.10, some scattering of the data can also be appreciated here. The results from Figure 5.10 and Figure 5.11 leave some margin to interpretations, but still it seems coherent to conclude based on the results, that all three parameters; B_n,$V_{l\,HIA}$ and $V_{l\,H+}$present a certain degree of correlation and could be used as distance indicators for further analysis.

There is however a minority of values which are not showing correlation or appear in a estrange quadrant, especially on the lower-right quadrant (positive values of B_n and negative values of V_l), but also some of them on the upper left (negative values of B_n and positive values of V_l). One of the possible explanations could be that some of these outlying structures are not really flux ropes, but another type of magnetic structures formed with similar magnetic field patterns originated during multiple X-line reconnection events, like a plasmoid. Another possibility could be they are just flux ropes moving on the opposite direction as it should be expected, which may be an interesting result. These outliers represent anyway a minor proportion compared to the whole collection of flux ropes, thus correlation will be assumed

for further analysis, although it is still important to mention this fact.

5.5 Spatial distribution of flux ropes

In this section, several spatial distribution maps will be represented. The intention behind this analysis will be to have an overview of the position where the flux ropes lay relative to its closest X-line, which would be assumed to be the source of its existence. There exist several parameters that could be used for this representation.

First and most obvious would be the distance, which can be easily calculated using the data available of the X-lines from the tables[4] in Appendix A. The procedure is really simple, if there is a register of the time instant when the spacecraft detects the X-line and same for the instant when the flux rope is detected, then the passing of the time between those two instants will represent the time difference between the moment that the spacecraft encountered the flux rope and the X-line. The spacecraft can either first detect the X-line and afterwards the flux rope or just the other way around, the time difference between both instants is $\Delta_t = |t\,(X-line) - t_{FR}|$, the sequence in which they are encountered will be given by $seq = sign\,(t\,(X-line) - t_{FR})$ being positive if first the X-line is encountered and negative for the other way around.This information can now be combined with the velocity at which the X-line is moving in the L direction $V_{l_{X-line}}$ to straightaway calculate the distance by means of the simple calculation $d_{FR} = \frac{seq \cdot \Delta t}{V_{l_{X-line}}}$, the velocity of the X-line is also available in Table **??** in LMN coordinates. Note also that for the case when two or more X-lines are detected in the same event, only the X-line which is closest to the analyzed flux rope will be considered, this is mathematically expressed in equation 5.4, where N represents the number of X-lines registered in the same event.

$$\Delta_t = min\,(\Delta_{t_i}) \qquad\qquad i = 1, 2, \cdots, N \tag{5.4}$$

Very important here is to correctly interpret the signs of time difference, velocity and distance. From this point, it will be considered that the velocity of the spacecraft is more than an order of magnitude lower than the velocities related to the movement of the X-lines, so that the spacecraft remains still during the time comprised between both encounters.

A positive value of seq will mean, the X-line is encountered after the flux rope is detected, which must necessarily mean that the X-line moves towards the spacecraft after the moment (and of course before) the flux rope detection is registered. If this happens on the earthward side of the X-line, then the X-line should move direction earthward to fulfill the frame of conditions established for this scenario, in this case seq would have a positive value and so will do $V_{l_{X-line}}$, finally resulting in a positive value of d_{FR}. Next scenario will have also apositive value of, but a negative value of $V_{l_{X-line}}$, which means that the X-line is moving tailwards, resulting in a negative value of d_{FR}. This two scenarios represent a situation where the spacecraft stands on the path of the X-line, and furthermore it is located on the side of the X-line where the flux rope lays.

On the other hand, a negative value of *seq* will mean, the spacecraft encounters first the X-line and then the flux rope, which has to necessarily mean, that the spacecraft lays on the opposite side of the X-line than the flux rope does. Now a positive value of $V_{l_{X-line}}$ is

registered, meaning the X-line is moving to the earth, this will lead to a negative value of d_{FR}, the flux rope will be here located at the tailward side of the X-line. As last scenario, $V_{l_{X-line}}$ is negative, leading to a positive value of d_{FR} which means that the flux rope lies on the earthward side of the X-line. This two scenarios represent the situation where the spacecraft stands on the path of the X-line, but the flux rope is on the other side of the X-line, which is consistent with the given interpretation of the *seq* negative sign.

All the four previously mentioned scenarios are coherent with the L direction given from the LMN coordinate system, so positive and negative values of d_{FR} will represent distances on the earthward and tailward side to the X-line respectively. A representation of this four possible scenarios can be observed in figure 5.12, here the purple triangle represents the spacecraft, while the red circle represents the flux rope. In Scenarios 1 and 2, the Spacecraft encounters first the flux rope and then the X-line, resulting in a positive value of seq. For scenarios 3 and 4 the spacecraft crosses the path of the X-line and then encounters the flux rope, so here $seq < 0$. The direction of the movement velocity $V_{l\,X-line}$ of the X-lines is shown in orange. The relative distance of the flux rope d_{FR} is shown in red..

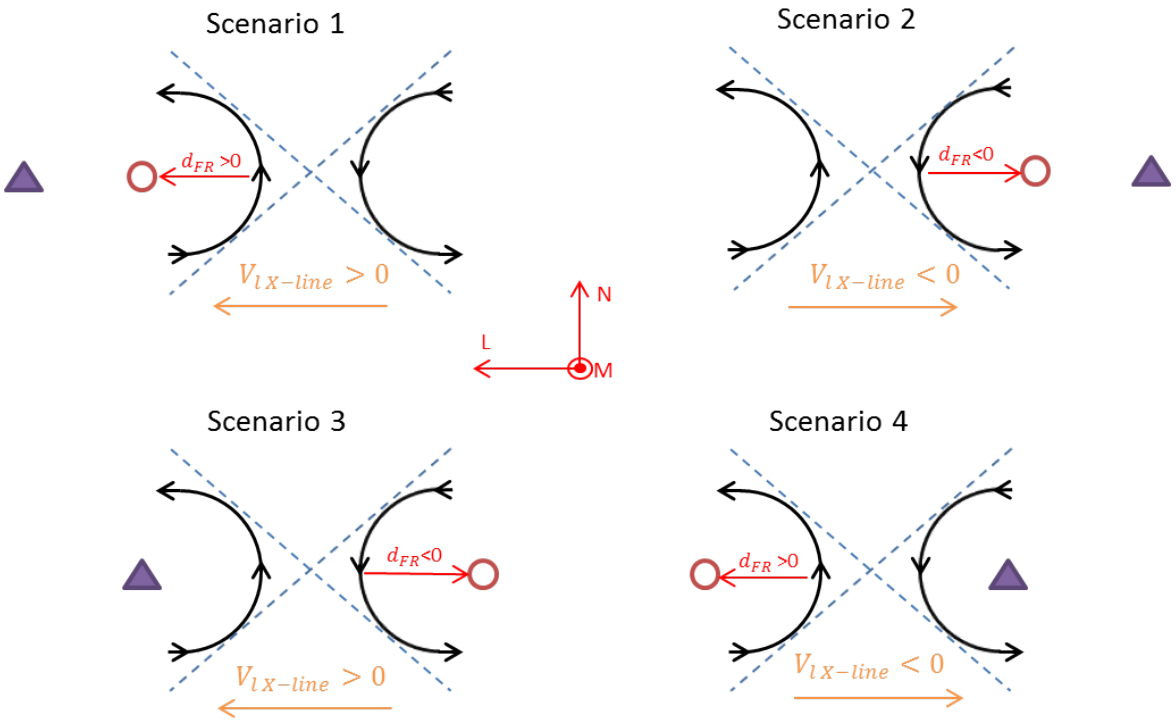

Figure 5.12: Four possible scenarios between spacecraft and X-line.

So far, the procedure to obtain the relative distance of flux ropes to its closest X-line was explained. However there are some events where no information of the X-lines is available, making impossible to calculate the distance for the flux ropes regarding those events. This will reduce the number of flux ropes available for the analysis, possibly resulting in a too reduced amount of data for a solid statistical study.

As an alternative option to solve this problem, some auxiliary parameters could be used as substitute of the distance values in order to avoid the lack of information from the X-lines. In the section 5.4 was already explained and justified, how and why the B_n component of the magnetic field as well as the V_l velocity of the ions could be good indicators of the relative distance to the X-line in the L direction.

At this point, there are enough resources to represent the position of the flux ropes relative to the X-line on the earthward or tailward side, however an indicator of distance from the neutral sheet to the separatrix is also needed to complement the spatial distribution map. For this purpose, the B_l background value can be used. Flux ropes will be located close to the current sheet, when the B_l component is almost zero (the magnetic field line is in that point almost purely B_n) and will take bigger values in magnitude when it gets close to the separatrix. Magnetic field lines are closed from the southern to the northern pole of the earth, presenting more positive values of B_l when close to the northern separatrix and more negative when close to the southern. The direction of the magnetic field lines at the earthward and tailward side of an X-line after reconnection as well as the separatrix typology were previously shown in Figure 5.9.

Putting all this together, a spatial distribution map of the flux ropes can be represented. Both maps, using distances and the auxiliary parameters V_l or B_n on the horizontal axis and B_l on the vertical will be represented to analyze some interesting properties about the nature of the flux ropes.This will lead to a 4 quadrant map, which can be interpreted as the four regions delimited by the tailward and earthward side of the X-line and the current sheet. These maps could be used to study the nature and properties of flux ropes regarding the position.

5.5.1 Flux rope rotation direction

One of the most characteristic properties of flux ropes is the rotation of the B_n component. This can be either right handed or left handed, and together with the core field B_m they form a helical magnetic field structure along the M axis, all this was previously explained with detail in Chapter 2. The direction of rotation is interpreted based on the oscillation registered in the B_n component combined with the relative motion between the spacecraft and the flux rope, whether a maximum is first encountered and then a minimum or the other way around.

Using distances in first instance and the parameters B_n and V_l as auxiliary indicators in second, the position of the flux ropes relative to the closest X-line in the L direction is represented and shown in Figures 5.13 and 5.14 respectively. The vertical axis representing the B_l background value indicates how far the flux ropes are located from the current sheet, being thus an indicator of the distance to the current sheet in the N direction of the LMN coordinate System, and so complementing the 2-D map of relative positions.

From this first map, there is clear evidence that most flux ropes are found on the earthward side of an X-line and only few of them appear to be on the tailward side. The blue or red color of the circles representing the flux ropes indicates which typology had the polarity of the B_n component, being a maximum and then a minimum encountered for red and the other way around for blue. Most likely, the *scenarios 1 and 2* from Figure 5.12 commented in the previous section are the ones who represent the great majority of flux rope encountered by a

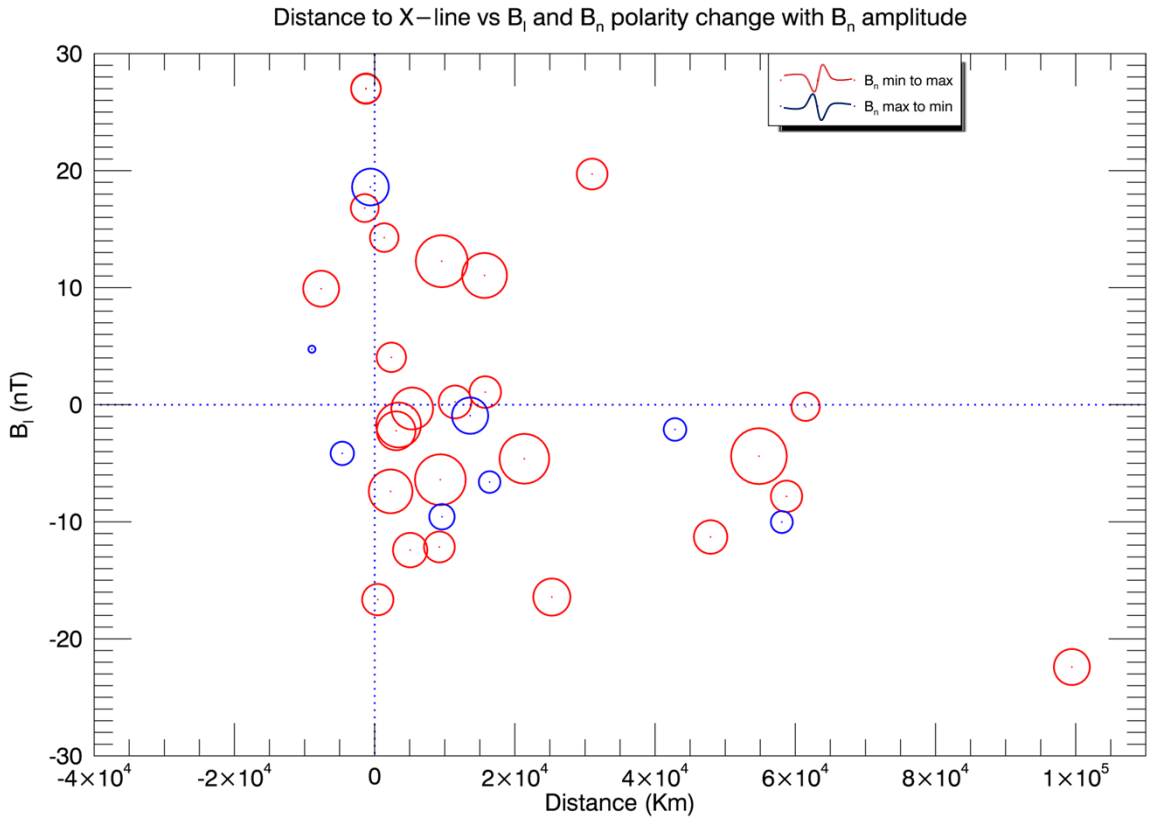

Figure 5.13: Spatial distribution map of the flux ropes' amplitude of B_n using distances.

spacecraft. There, the magnetic field component B_n shows a minimum and then a maximum for crossings on the earthward side, meaning the flux rope is moving to the earth across the spacecraft and a maximum and then a minimum for detections occurring on the tailward side, meaning the flux rope moves tailwards across the spacecraft. The fundamentals regarding these conclusions about the meaning of the oscillation typology where explained previously in detail in section 2.4.

It could be interpreted from Figure 5.13 that the vast majority of the detected flux ropes are located on the earthward side of the X-line and move earthwards directed (red). There are a few cases when flux rope is located on the tailward side of the X-line, however they all are very close to the X-line, and the direction of movement is not clearly tailwards directed (blue).

Regarding the amplitude of the peak-to-peak B_n component, it seems like flux ropes with bigger amplitude of the B_n max-to-min polarity are located in regions both, close to the X-line and close to the current sheet. However there are also flux ropes with small amplitudes located in these regions, and also some big amplitude flux ropes far from the X-line, so any clear evidence of this correlation can be stated.

There is however an interesting result represented by the blue flux ropes shown in the lower left quadrant of Figure 5.13. Those detections are registered as flux ropes which are

detected on the earthward side of the X-line and move towards it. This motion opposes to what was expected, since flux ropes are meant to move away from the X-line due to the ion outflow, which leads to an interesting result to consider from this analysis.

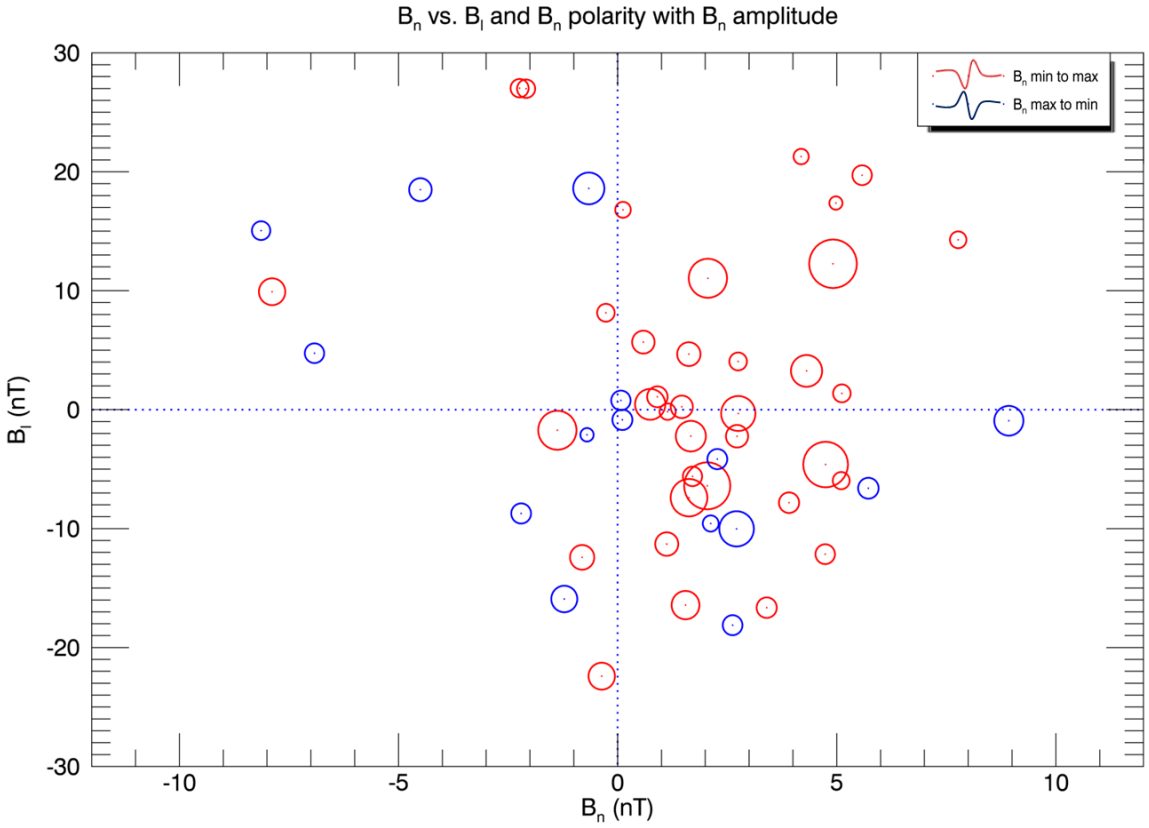

Figure 5.14: Spatial distribution map of the flux ropes' amplitude of B_n using the auxiliary parameter B_n.

In this second representation, the parameter B_n is used as indicator of distance in the L direction. Also V_l could be used as auxiliary parameter for distance. The figures showing this analysis can be found in Appendix D, and only the spatial map using B_n will be shown here in Figure 5.14 to avoid information redundancy, due to the fact that both maps, using B_n and V_l give very similar results for this analysis. From the spatial distribution of Figure 5.14, similar results as the ones concluded from Figure 5.13 can be noticed. There is again a vast majority of flux ropes which are located on the earthward side of the X-line, here represented with a positive value of the B_n component, and same as before, most of them are moving earthwards directed, crossing the spacecraft on its way and registering a minimum to maximum pattern on the B_n component (red). Although in this case, there is a higher number of flux rope detections on the tailward side of the X-line than the ones shown in Figure 5.13. Most of them are also moving tailwards, with the spacecraft registering a maximum to a minimum (blue) on the B_n component during crossing with the flux rope. Regarding the amplitude of the peak to peak B_n, the results are here a bit unclear. It seems to be some tendency for

bigger amplitudes to be located close to the current sheet and close to the X-line, but the results are not representative enough to make a solid statement about this.

It is important to mention, that for the maps which make use of auxiliary parameters, the number of available flux ropes for the statistics is much higher than for the statistics based on the distance calculated using available X-line data. For this reason, both types of maps are important for the analysis, and as evidence of this, a conclusion about the flux ropes located on the tailward side could for this case only be interpreted from the map based on the parameter B_n shown 5.14.

The same scenario which was detected in the previous analysis of Figure 5.13 is also noticeable in Figure 5.14, where blue flux rope detections are again registered in the lower right quadrant. The amplitude of those flux ropes are considerably smaller than for the rest of detections moving earthwards. The fact that this situation is observed in both analysis is a very interesting result. The possible sources that could originate such a phenomena will be discussed in the following section, after the flux rope length is analyzed.

5.5.2 Flux rope length

Another interesting point of analysis would be the length of the flux ropes, and how is it influenced depending on the position that they occupy relative to its closest X-line. For this analysis, the same types of spatial distributions shown in the previous Figures 5.13 and 5.14 are used, but in this case, the length of the flux ropes has to be somehow represented. The corresponding flux rope length can be easily calculated as $l_{FR} = |t_{max} - t_{min}| \cdot v_{FR}$, where $|t_{max} - t_{min}|$represents time difference between the maximum and the minimum on the signature of the B_n component or vice versa, v_{FR} refers to the relative velocity between the spacecraft and the Flux rope, which will be considered as the ion outflow velocity in the L direction.The same map using the auxiliary parameter B_n as shown in FR pol aux will be used here, as it was selected previously as the one with the best spatial distribution of flux ropes regarding its rotation direction and position from all the available distribution maps using auxiliary parameters. The spatial distribution maps for this analysis are shown in figures 5.15 and 5.16 as well as 5.17 and 5.18.

For the two spatial distribution maps shown in Figures 5.15 using distances and 5.16 using the auxiliary parameter B_n, the length of the flux rope is calculated using the velocity $V_{l\,HIA}$ as flux rope velocity relative to the spacecraft, then length is normalized and represented in the figures by the size of the circle.

For this case where the lengths are related to $V_{l\,HIA}$, it appears not to be a certainly clear relationship between the length and the position of the flux ropes relative to the X-line. However it can be appreciated in both figures, that some big flux ropes are encountered for regions close to the vicinity of the X-line, while far away mostly all flux ropes are smaller. About the distance from the current sheet, it is also unclear which influence this could have on the length of the flux ropes. It seems at least on Figure 5.16 that bigger flux ropes tend to appear closer to the current sheet, although there are also some big flux ropes in regions separated from the current sheet, characterized with higher values of B.The relationship between position and flux rope length is unclear being the realization of further analysis necessary to contrast whether this relationship is real or not.

Once again, a family of blue flux ropes can be observed in the lower left quadrant of

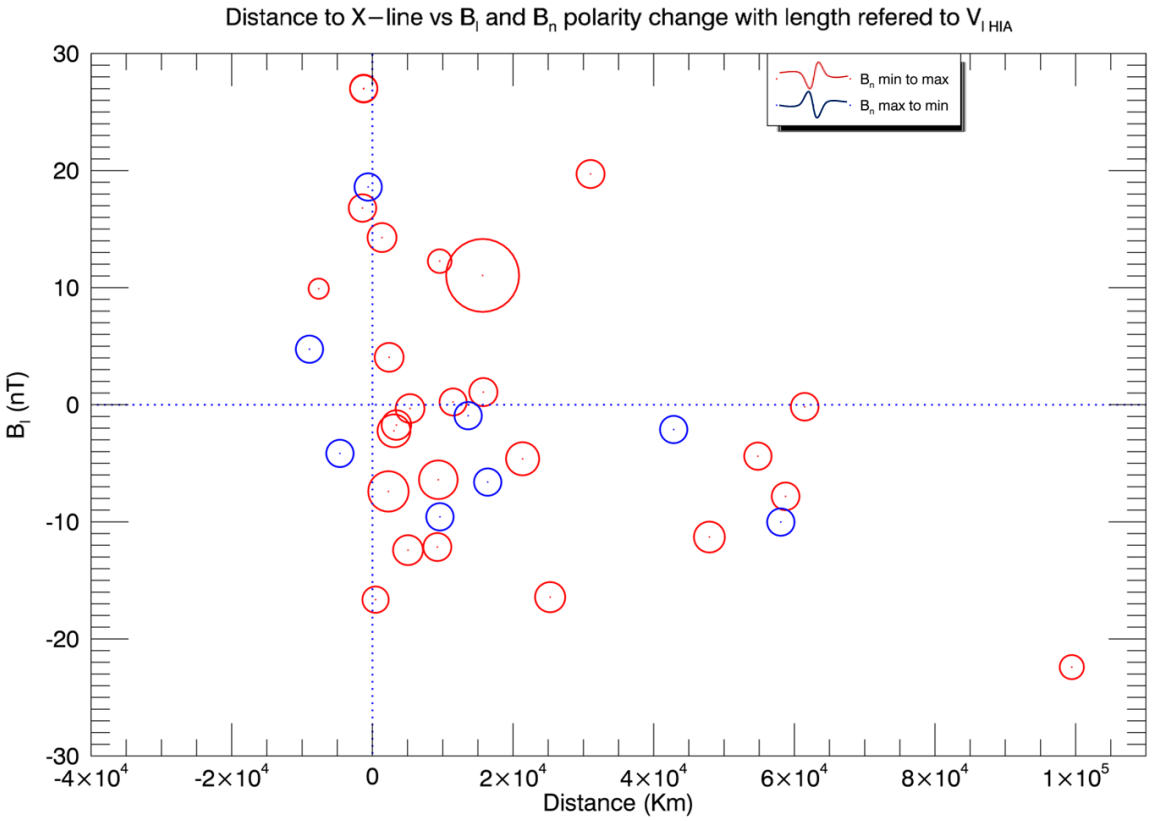

Figure 5.15: Spatial distribution map of the flux ropes' length referred to $V_{l\,HIA}$ using distances.

Figures 5.15 and 5.16, which as was already commented, represent flux ropes located in the earthward side of the X-line whose motion is directed to the X-line, opposed to the direction of the ion outflow. The length of those flux ropes is considerably smaller than the rest of 'expected' red detections. This is consistent with the lower amplitude they were presenting from the study realized in the previous section.

One more time, the two spatial distribution maps using distances and the auxiliary parameter B_n are represented in Figures 5.17 and 5.18, although in this case the lengths of the flux ropes are calculated by means of $V_{l\,H+}$ as relative speed between spacecraft and flux rope. Same as did before, lengths are normalized and then represented in the maps as the size of the circles, giving a good overview of the length distribution of the flux ropes in the space.

This time, lengths are related to $V_{l\,H+}$ and it shows a similar scenario than the previous analysis, but still with some differences. Both figures show again an uncertain pattern regarding how the length of the flux ropes are related to its position on the surroundings of the X-line, and also same than in the previous analysis, it seems that the biggest flux ropes tend to appear in the vicinity of the X-line, for low values of distance. In this case, some flux ropes of big lengths are located close to the X-line, although there are also lot of smaller flux

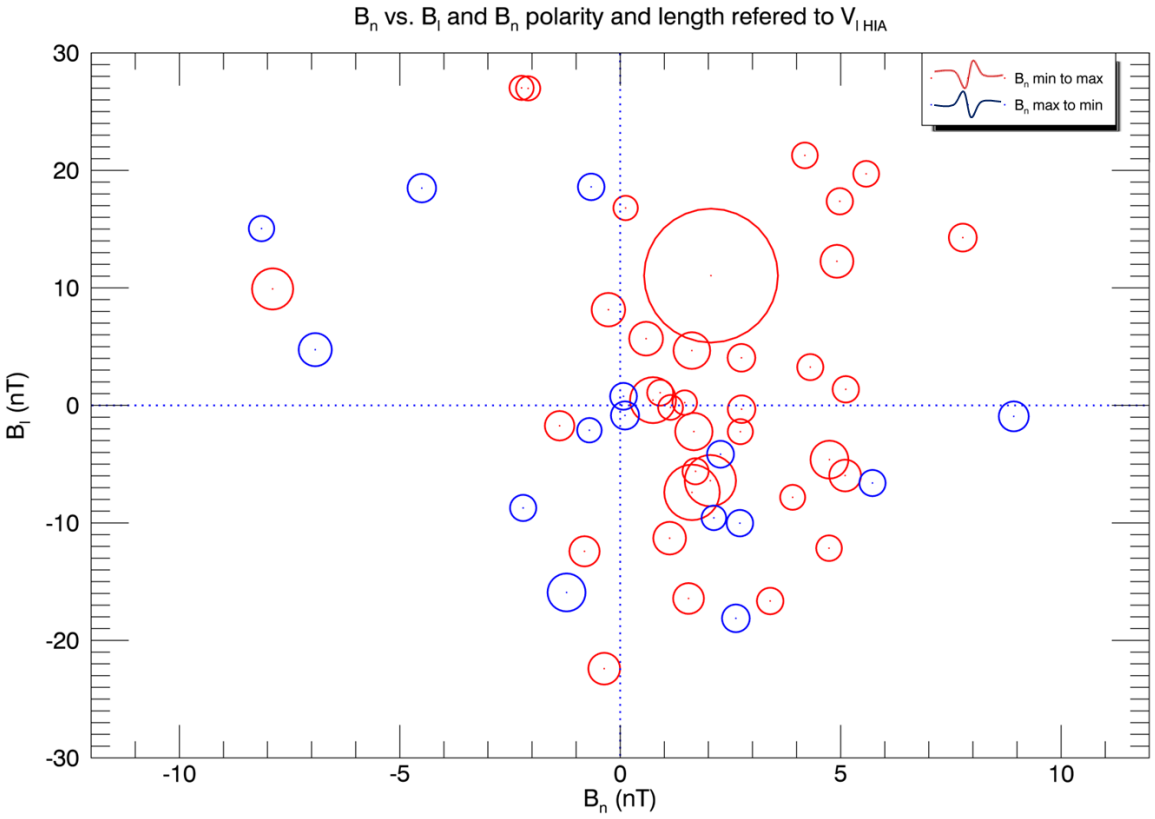

Figure 5.16: Spatial distribution map of the flux ropes' length referred to $V_{l\,HIA}$ using the auxiliary parameter B_n.

ropes which does not differ much from the ones located at higher distances from the X-line. The results shown in both analyses contain a big degree of uncertainty about this fact, and it would be courageous to ensure this relationship between length and distance from the X-line despite the conclusions extracted.

Again in this analysis is interesting to highlight, that in a similar way as for the previous length analysis referred to $V_{l\,HIA}$, the blue flux ropes detected in the lower left quadrant of Figures 5.17 and 5.18 also present a smaller length compared with the rest of flux rope detections located in this quadrant.

Referring to the influence of the distance to the current sheet or the lobes, once again it is complicated to make a solid conclusion based on the results regarding the flux rope's length. Specially in Figure 5.18 there are some big length flux ropes at distances where B_l is low, and also the smallest flux ropes seem to be placed at higher distances from the neutral sheet. This could mean that bigger flux ropes tend to be located closer to the current sheet, while smaller tend to be located closer to the lobes, although the analysis is not clearly enough representing this fact as to make a solid statement about it. The results shown for lengths calculated using $V_{l\,HIA}$, show a similar uncertain distribution regarding the influence of the distance from the current sheet as for this case using $V_{l\,H+}$. For this reason, it would be

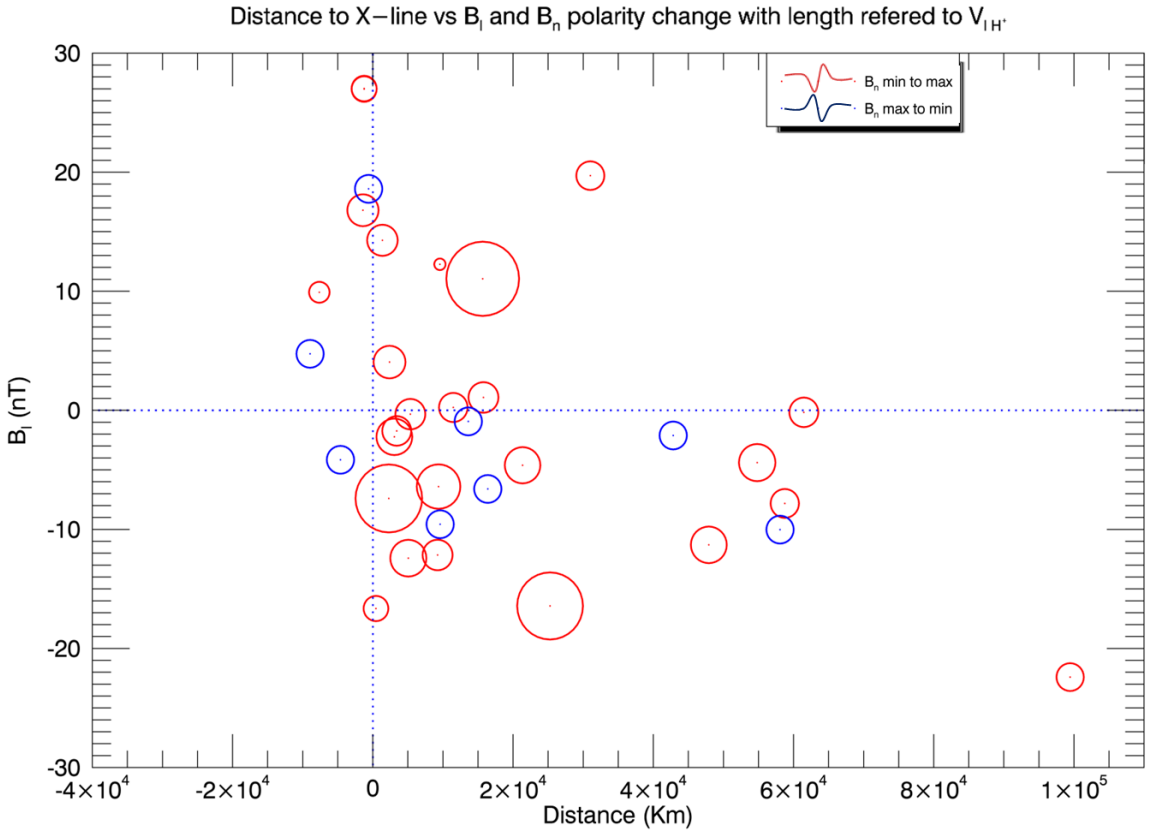

Figure 5.17: Spatial distribution map of the flux ropes' length referred to $V_{l\,H^+}$ using distances.

cautious to state that the relationship between the length and the distance from the current sheet to the lobes cannot be concluded considering the results obtained from these analyses, despite the points previously highlighted.

On the other hand, the results obtained from the length analysis of the flux ropes present very short lengths for those flux ropes located in the lower left quadrant are represented as blue detections. This result reinforces the idea that this family of flux ropes which oppose the direction of the ion outflow are small in size, while the analysis realized in the previous section 5.5.1 lead to the conclusion that they are also characterized by a small amplitude of the B_n component variation. The existence of these flux ropes whose motion opposes the ion outflow on the earthward side is a very interesting result, since similar results have been registered in several studies based on fully-kinetic simulations *[Nakamura et.al, 2016]*[9]. The cause for this unnatural motion could be that the flux ropes are being driven by an enhancement of the currents generating the Hall effect shown in the next section in Figure 5.19. The lower left quadrant of this figure corresponds to the lower right quadrant of the previous analysis, and as can be seen, the hall field has a negative polarity for that region. The Hall field in that quadrant could be enhanced during periods of negative guide field, thus generating an enhancement of the electron stream and maybe originating the displacement of the flux ropes

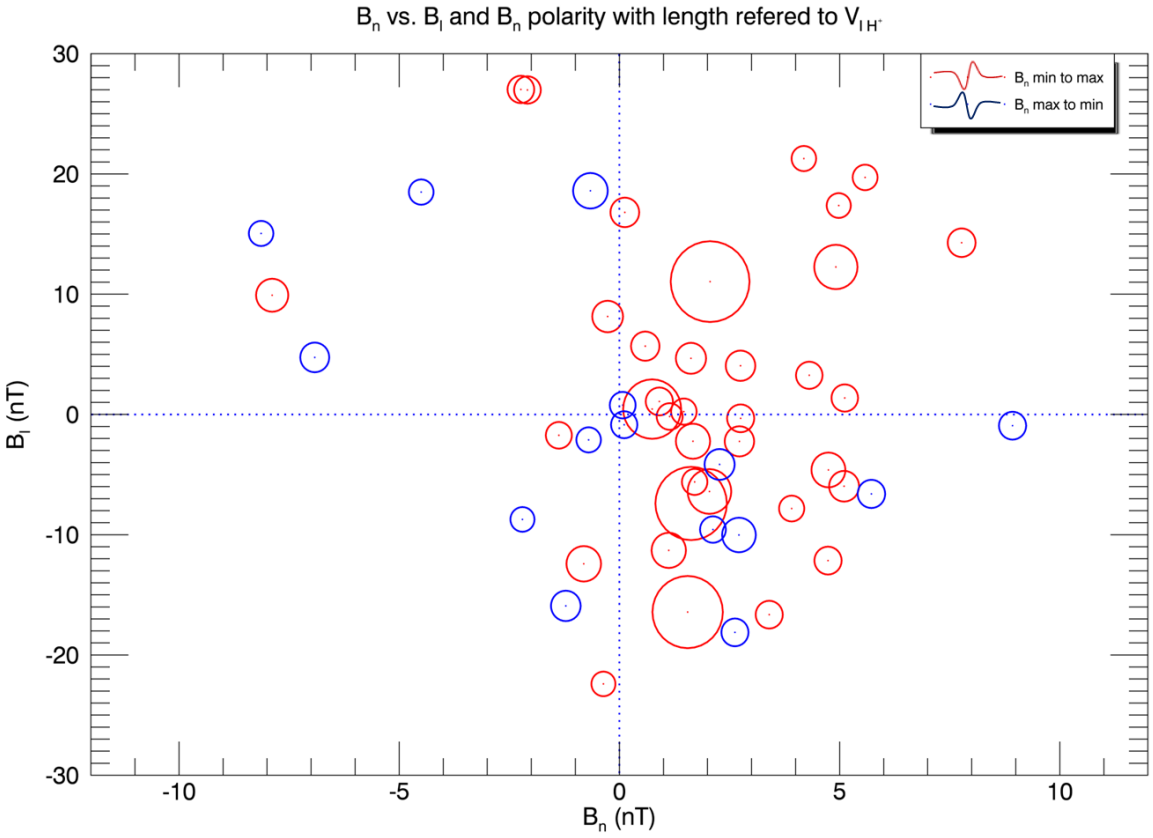

Figure 5.18: Spatial distribution map of the flux ropes' length referred to $V_{l\,H^+}$ using the auxiliary parameter B_n.

as previously commented.

5.5.3 Flux rope Core field and Hall field

When magnetic reconnection occurs, the magnetic field lines merge and an X-line is created. In the vicinity of the X-line a certain typology of magnetic field is created, the so called quadrupolar Hall-field pattern, the formation and mechanisms that drive this phenomenon where explained previously in section 2.5 of Chapter 2. The structure of the quadrupolar hall field pattern in the vicinity of a X-line is shown in Figure 5.19.

Hall magnetic field is one of the sources that could drive the background value of the B_m as well as the polarity of a flux rope's Core field $B_{m\,CORE}$. The guide field associated to an event could also influence the direction of the $B_{m\,CORE}$ and determine its polarity. The guide field is referred as the magnetic field ground floor level existing in an event before the magnetic reconnection take place. Definitions of guide field, background values, Core field and other important parameters regarding the magnetic field components where previously explained in Chapter 4.

To examine the aforementioned possible factors which may influence $B_{m\,CORE}$ polarity,

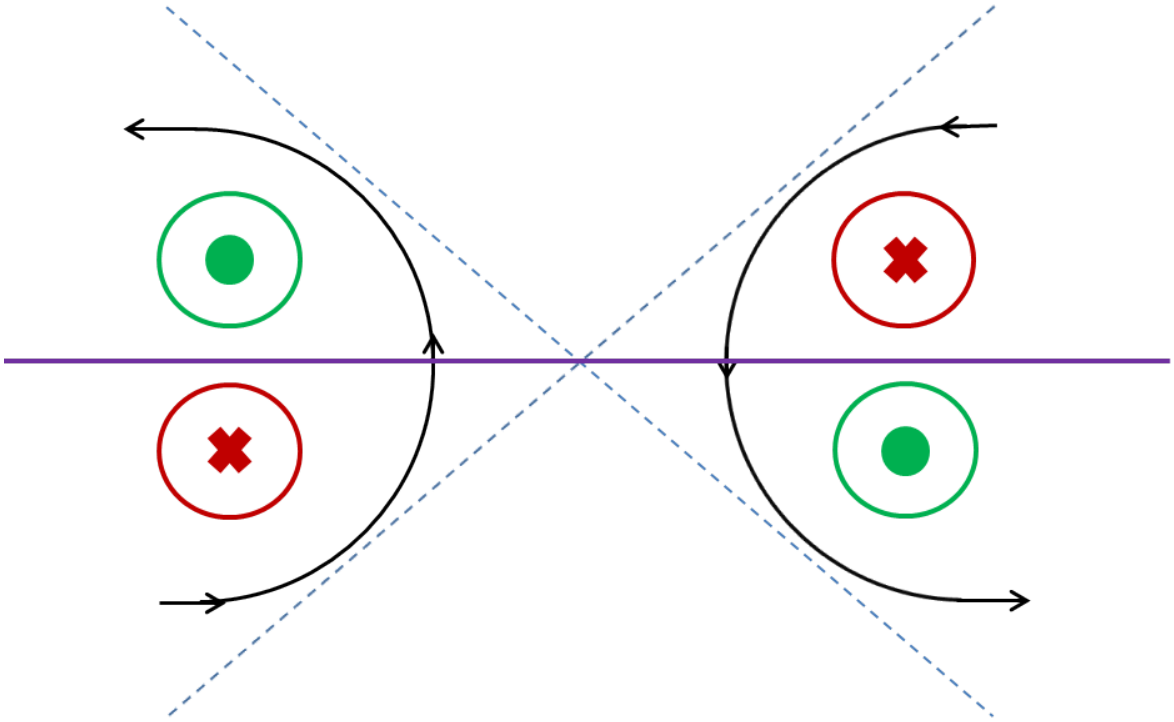

Figure 5.19: Pattern of the hall field generated in the vicinity of the X-line after magnetic reconnection.

a new analysis using once again the distances from the X-line, and auxiliary parameters such as B_n or V_l will be realized. However, in this case the analysis will be focused on the B_m component instead of the B_n component like was done in the previous section. The first instance of this analysis is shown in figures 5.20 and 5.21. here $V_{l\,HIA}$ and B_l background represent distance in the L and N directions respectively. The color of the circles represents the polarity of the $B_{m\,BG}$ value where the value of the Guide field is included. The size of the circle indicates the amplitude of the difference between $B_{m\,CORE}$ and $B_{m\,BG}$, while in figure 5.21 the symbols represent parallelism (diamond) or anti-parallelism (cross) between $B_{m\,CORE}$ and $B_{m\,BG}$ polarities.

The scenario shown in Figure 5.20 does not show a clear trend for the background value of B_m. Values are spread in all four quadrants without any noticeable pattern, and far for being close to resemble the Hall field pattern which is looked for. Under these circumstances, this analysis will be underestimated for the study of the hall field pattern related to the flux ropes' B_m background. The only conclusion that perhaps could be made would be the apparent existence of bigger background magnetic fields for distances which are closer to the flux rope. However, there is not a clear pattern in order to make a solid conclusion about this fact, so the result will be compared with other maps before making a statement about this.

For the representation using an auxiliary parameter of the distance, a map using $V_{l\,HIA}$ as auxiliary parameter is represented for this analysis and shown in Figure 5.21. The rest of maps created using the rest of auxiliary parameters are shown in the appendix at the end

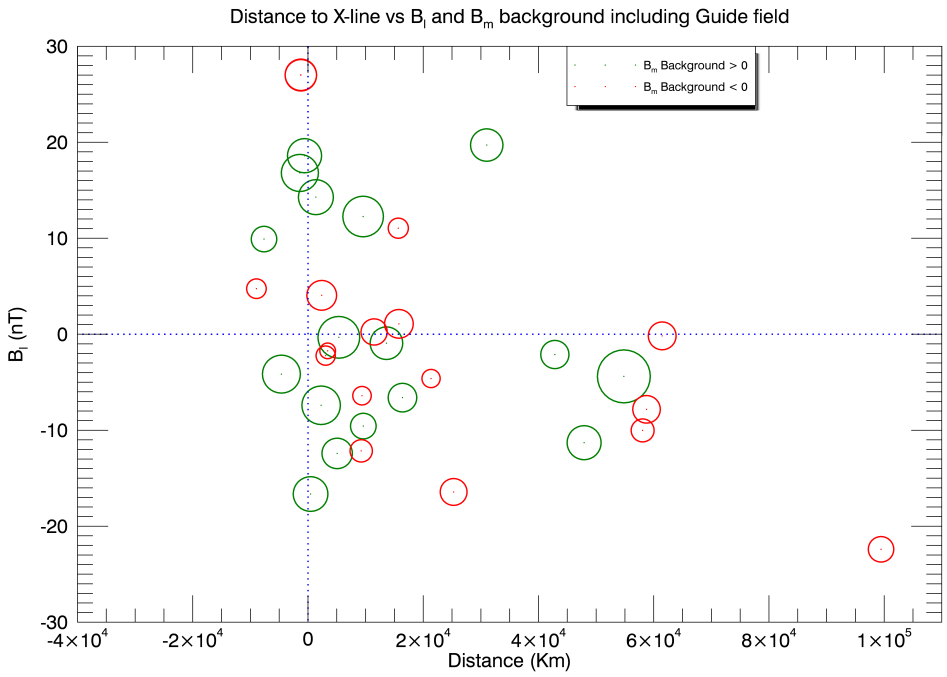

Figure 5.20: Spatial distribution map of the flux ropes' $B_{m\,BG}$ (Guide field included) and $B_{m\,CORE}$ polarities using distances.

of this work. From the spatial distribution of Figure 5.21 it can be appreciated, that the polarity of the flux ropes' B_m Background is somehow resembling the hall field pattern shown in Figure 5.19. There is a clear defined pattern of the hall field for 3 of 4 quadrants, although the pattern is not completed due to mixed values of the B_m background polarities appearing on the upper right quadrant of Figure 5.21 (correspondent to the upper left quadrant of 5.19).

Another important point of special importance in this section is the polarity of the $B_{m\,CORE}$ magnetic field component and what could originate it. For this purpose, the relationship between $B_{m\,CORE}$ and $B_{m\,BG}$ polarities was subjected to study. The idea is to determine whether $B_{m\,CORE}$ and $B_{m\,BG}$ are parallel (same polarity, represented with a diamond) or anti-parallel (opposite polarity, represented with a cross) in order to show if there is a connection between $B_{m\,BG}$ polarity and the polarity of the $B_{m\,CORE}$ although in light of the results shown in Figure 5.21, any clear evidence of an influence of the $B_{m\,BG}$ polarity over the polarity of $B_{m\,CORE}$ is appreciated.

Last before closuring the analysis of these two maps, also mention that there is in Figure 5.21 any clear pattern regarding the magnitude of the B_m background. It seems to exist some degree of dependency between the distance to the current sheet and the magnitude of B_m

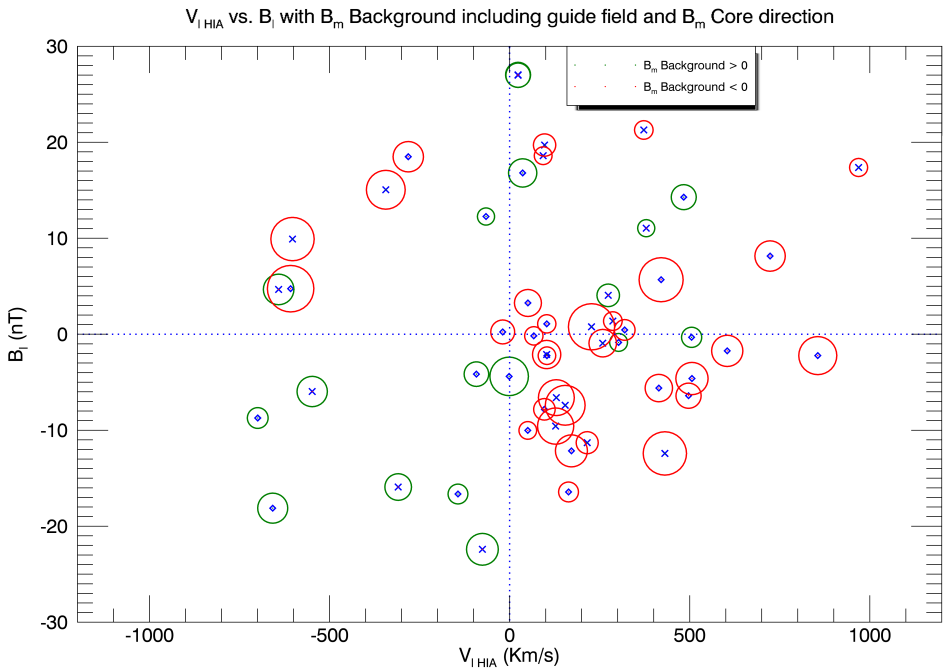

Figure 5.21: Spatial distribution map of the flux ropes' $B_{m\,BG}$ (Guide field included) and $B_{m\,CORE}$ polarities using the auxiliary parameter $V_{l\,HIA}$.

background, since there are some flux ropes sowing higher values of the background magnetic field for distances closer to the current sheet, although the distribution is not clear enough to conclude a solid statement about this fact.

Considering the results obtained from the previous analyses,any solid conclusions about the Hall field nature of B_m background or the correlation between $B_{m\,BG}$ and $B_{m\,CORE}$ polarity can be drawn. However, for the case of the Hall field pattern of $B_{m\,BG}$, the result was close to resemble the pattern it was looked for, only failing to fulfill it on the upper-right quadrant of figure 5.21. Based on this result it was thought, that maybe the existing guide field had too much influence over the background value of the B_m component, thus distorting the Hall field pattern.

A new analysis of the scenarios shown in figures 5.20 and 5.21 will be realized once again, although now the guide field existing at the beginning of each event will be subtracted to the B_m background value of each flux rope, resulting in the pure background value of the B_m component. Using these 'true' background values, both analyses using distances and the auxiliary parameter of distance V_{lHIA} will be again realized to check if the Hall field pattern fits with the values of B_m background in this case and also to examine if there is dependency between the polarity of these background values and the polarity of $B_{m\,CORE}$.

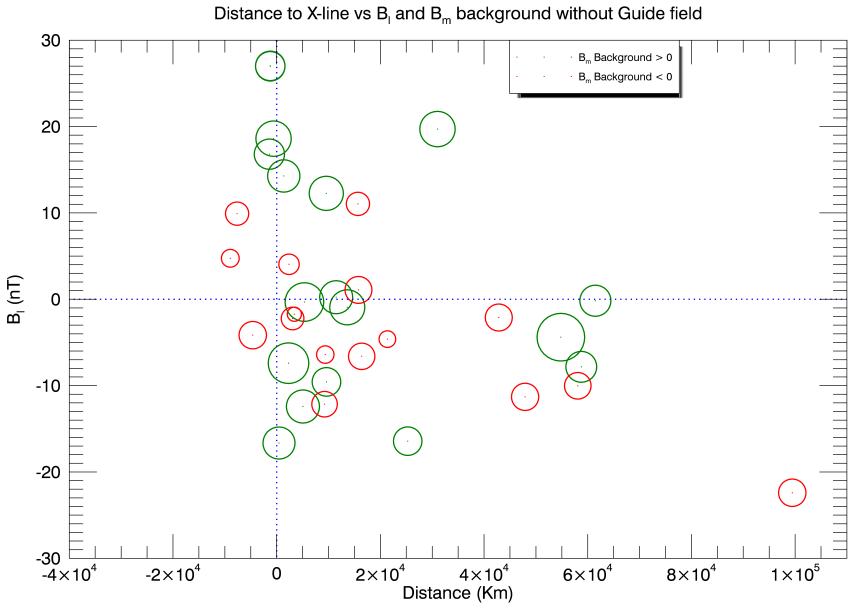

Figure 5.22: Spatial distribution map of the flux ropes' $B_{m\,BG}$ (Guide field substracted) and $B_{m\,CORE}$ polarities using distances.

From the first analysis shown in Figure 5.22 using the calculated distances, a similar result to the previous one including the guide field is obtained and important conclusions regarding hall field behavior of background can be drawn. Once again, the biggest values of B_m background seem to appear located close to the X-line, although the distribution is still a bit uncertain to make a solid statement about this, since there are also some flux ropes with high background values located at distant positions.

On the other hand, the analysis in Figure 5.23 using $V_{l\,HIA}$ as distance indicator is clearly showing the hall field pattern for values of B_m background. Here can be seen that all four quadrants follow in rough outlines the hall field pattern which was shown in 5.19, so it can be concluded, that the polarity of the pure value of the background B_m component is strongly driven from the Hall field related to the nature of an X-line originated due to magnetic reconnection.

So far, the dependency between the Hall field and the true background value of the B_m component was confirmed, although the factors that influence the polarity of the $B_{m\,CORE}$ are still uncertain. In the same way as was represented in Figure 5.21 aux, the relationship between the polarities of B_m background and $B_{m\,CORE}$ are shown in Figure 5.23, where a diamond represents the case when both components are parallel (both have the same polarity), and a cross when components are anti-parallel (opposite polarity). Based on the results shown in Figure 5.23 regarding the dependency between $B_{m\,BG}$ and $B_{m\,CORE}$, a certain degree of dependency between $B_{m\,BG}$, which at the same time is following the Hall field pattern, and

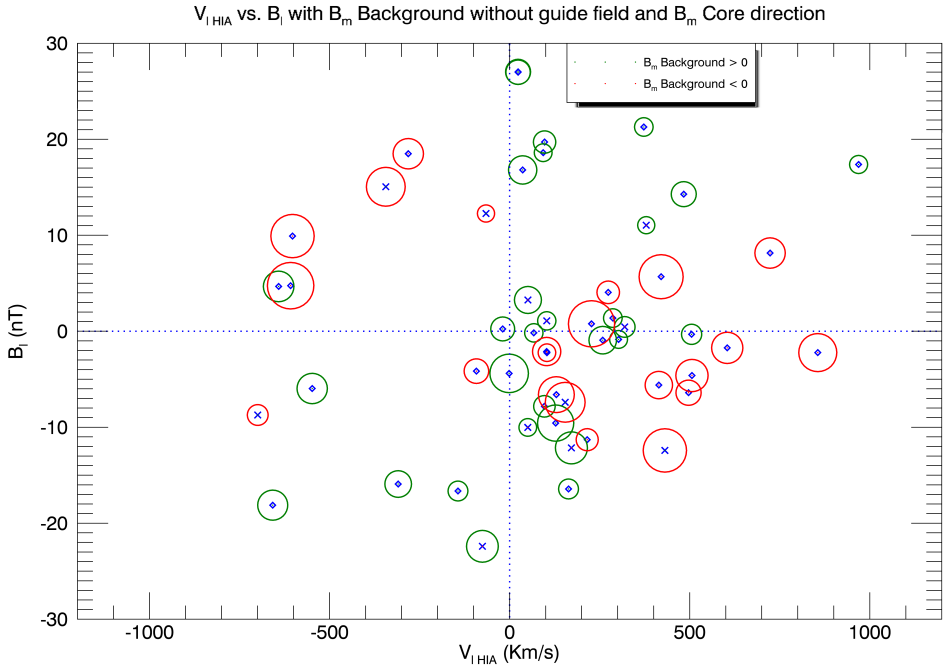

Figure 5.23: Spatial distribution map of the flux ropes' $B_{m\,BG}$ (Guide field substracted) and $B_{m\,CORE}$ polarities using the auxiliary parameter $V_{l\,HIA}$.

$B_{m\,CORE}$ can be observed. Being more accurate, 40 of all the represented flux ropes are showing a parallelism of both components, which means that a 77% of the flux ropes shown in 5.23 are showing dependency between Hall field and $B_{m\,CORE}$. Considering this results it could be concluded that the Hall field is once again a factor of great influence not only in the background value of B_m but also in the polarity of $B_{m\,CORE}$.

The $B_{m\,CORE}$ could also be influenced by the polarity of the guide field, so an analysis regarding this fact would also be necessary. For the purpose of this analysis, the events are filtered depending on the magnitude of its guide field, and only events with big guide fields were considered, referring as big guide field events in this case for guide fields of magnitudes bigger than 6 nT, the definition of guide field was previously commented in section flux rope detection. The results of this analysis can be seen in figure 5.24. Here $V_{l\,HIA}$ and B_l background represent distance in the L and N directions respectively. The color of the circles represents the polarity of the guide field. The size of the circle indicates the magnitude of the guide field, while the symbols represent parallelism (diamond) or anti-parallelism (cross) between $B_{m\,CORE}$ and guide field polarities.

Based on the results of shown in figure 5.24, there is no clear evidence of strong influence of the polarity of B_m over the polarity of $B_{m\,CORE}$ for higher guide field values. However,

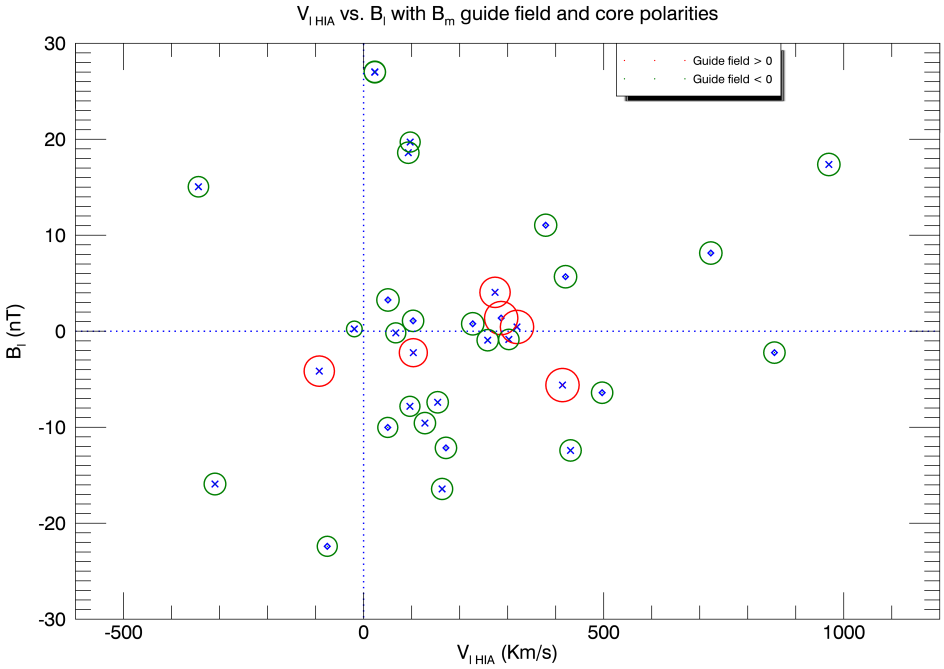

Figure 5.24: Spatial distribution map of the flux ropes' Guide field and $B_{m\,CORE}$ polarities using the auxiliary parameter $V_{l\,HIA}$.

the graphic shows around a 50% of flux ropes whose $B_{m\,CORE}$ lays parallel to the direction of the guide field, so even when it would not be possible to state that $B_{m\,CORE}$ is mainly driven by the guide field, it does seem to have some degree of influence over the polarity of $B_{m\,CORE}$. Moreover, if the results shown in Figures 5.24 and 5.23 are compared, it can be noticed that some of the flux ropes whose $B_{m\,CORE}$ polarity was not coherent with the Hall field pattern are coherent with the polarity of the Hall field, this fact is shown in Figures 5.25a and 5.25b.

Finally, considering the combined results shown in Figures 5.25a and 5.25b it could be stated that the polarity of $B_{m\,CORE}$ is influenced by a combined effect of mainly the Hall field, but also the guide field for cases where a big guide field is present. The combination of these two effects leads to 46 of 52 cases, which means almost a 90% of the studied flux ropes, where the polarity of $B_{m\,CORE}$ is parallel to the combined effect of both, Hall field, which at the same time determines the background polarity of B_m, and the strong existing guide field.

Briefly summarizing, in this section the $B_{m\,CORE}$ and the background value of B_m regarding the flux ropes where analyzed with the purpose of understanding which mechanisms could drive the polarity of these two parameters. It was first demonstrated that after

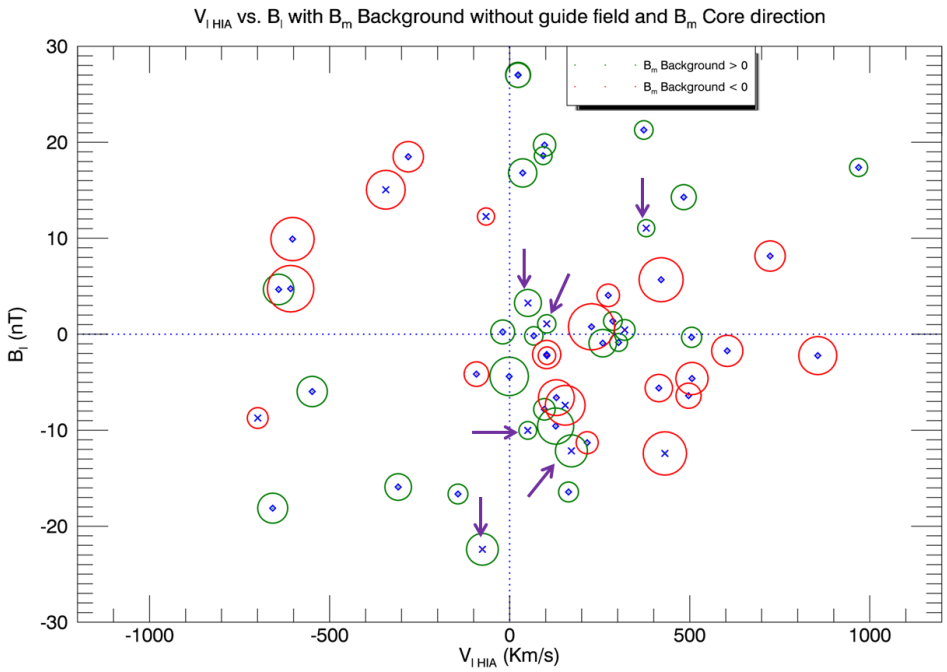

(a) B_m background analysis from figure 5.23

Figure 5.25: Figure 1 of 2 spotting the flux ropes whose $B_{m\,CORE}$ polarity is parallel to the guide field, but not to the Hall field.

withholding the guide field from the total B_m value, the true value of the background B_m was parallel to the polarity of the hall field pattern, meaning the background was behaving mainly driven from this effect. Secondly was proven that the polarity of $B_{m\,CORE}$ is highly influenced by the combined effect of the Hall field and guide field polarities for cases where high guide fields existed, although the combined mechanism of both and the dominance of one effect over the other for the determination of the $B_{m\,CORE}$ polarity could not be stated.

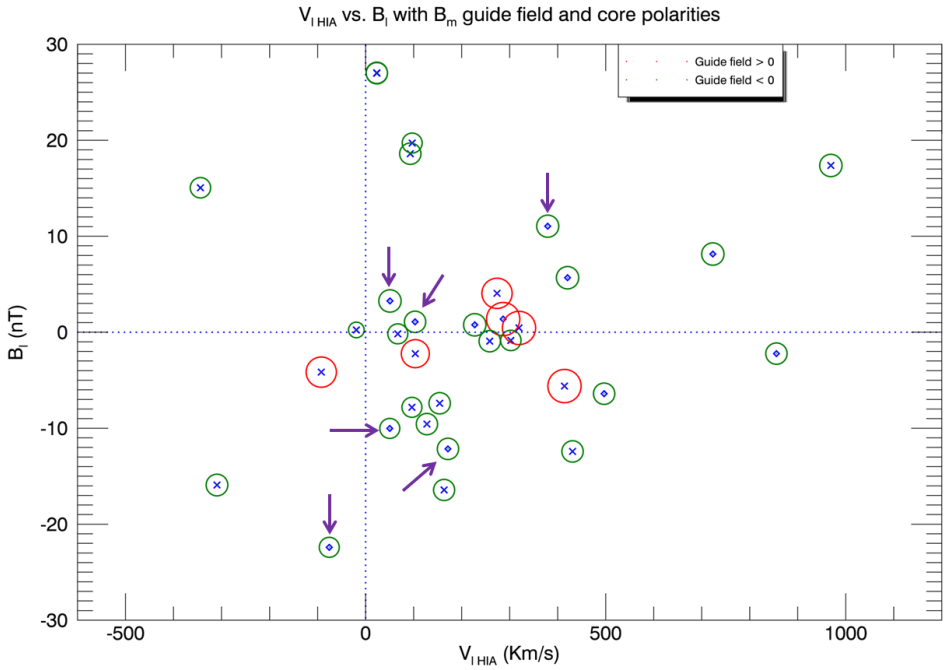

(b) Guide field analysis from figure 5.24

Figure 5.25: Figure 2 of 2 spotting the flux ropes whose $B_{m\,CORE}$ polarity is parallel to the guide field, but not to the Hall field.

6 Conclusions

This work consisted on the detection and statistical analysis of small scale flux ropes detected in the plasma sheet on the earth magnetotail. A list of magnetic reconnection events with multiple X-line formation from the early years of the cluster mission, 2001 to 2005 was examined in search of the existence of flux ropes. The Cluster mission is characterized by a high elliptical polar orbit and four spacecraft that fly in a tetrahedral configuration. The inter-spacecraft distance is adjusted corresponding to the objectives of the mission to focus on higher scale or smaller scale structures. All of the events analyzed during this work correspond to periods of magnetotail crossing close to the current sheet.

The data corresponding to this time lapse was downloaded from the Cluster Science Archive, previous registration. The measurements used for this work were the magnetic field vector correspondent to the *FGM* experiment, and the velocity of the ions, obtained from the plasma particle distributions measured by the *CIS* experiment. Both instruments of *CIS*; *CODIF* and *HIA* were used, although *CIS* from cluster 2 is not available since it stopped functioning short after launch.

6.1 Summary

The detection of those structures was performed by the implementation of an automatic search algorithm. The data correspondent to each of the pre-selected events was scanned by an analysis in time domain executed on different time scales. The search criteria of the detection algorithm determines its performance, and it was developed based on known models of flux rope *[Borg et.al, 2012]*[11]. The flux ropes in this model are characterized by characteristic patterns that the vector magnetic field signatures show in each axis. Those patterns should be measured by a spacecraft during a crossing between the spacecraft and a flux rope, so the detection algorithm should be able to recognize those patterns in order to properly register that time instant as flux rope detection. Only data from the *FGM* was needed for the flux rope detection. The algorithm was adjusted based on flux rope detections already known from other studies *[Borg et.al, 2012; Teh et. al, 2013]*[11, 12], which were taken as reference. After visual inspection of the automatic detections and a long period of trial and error, the flux ropes shown in those studies were also detected by the automatic search and the vast majority of remaining flux rope detections were considered to possess an acceptable quality. Many parameters and several conditions were defined in order to model the detection criteria based on adjustable key values. A multi-scale analysis method in time domain was implemented to analyze the data in different time scales, making the detection of different scale structures much easier. Two different windows, one contained inside the other were defined to realize the analysis. Those windows will shift its position for each iteration of the detection algorithm in such a way that all data is analyzed at the end of the automatic search. The windows will then reduce its dimension (the number of samples contained) and

repeat the procedure again, so that smaller scale structures are detected in this iteration. This procedure last for 8 different time scales, and so a database of multi-scale flux ropes is conformed.

The collection of flux ropes detected served as database for the statistical analysis. Data corresponding to the velocity of the ions from the measurements of both *CIS* instruments; *CODIF* and *HIA* was used. Two different types of analyses were realized depending if the relative distance between a flux rope and its nearest X-line was available or not. For the cases were the distance was not possible to be calculated, auxiliary parameters like B_n or V_l were used and so a spatial distribution of all flux ropes in the vicinity of its nearest X-line could be represented.

From the multiple statistical analysis realized, several interesting conclusions regarding important aspects are obtained, while other aspects remain still unclear. The conclusions achieved through the analysis of the flux rope database are the following:

Most of the detected flux ropes have duration shorter than 10 seconds, with 75% of the detections presenting a duration below six seconds. The maximum number of detections is registered for durations between one and three seconds. This result is obtained from the histogram analysis.

The magnetic field signatures show the expected patterns. From the superposed epoch analysis, the quality of the detected signals was checked. Despite the existence of some detections where the pattern of the magnetic field signatures was not as clear as pretended, in general the patterns of the magnetic field vectors were resembling what was expected.

The vast majority of the flux ropes are detected on the Earthward side of the X-line with an Earthwards directed motion. This result is coherent with the situation that was expected to encounter. This result was obtained by analysis of the spatial distribution of flux ropes focusing on the characteristics of the B_n component during detection.

$\mathbf{B_{m\,CORE}}$, background and guide field polarities are connected. The Statistical analysis of the B_m component showed a very interesting result. The background value of B_m shown in the vicinity of the X-line a distribution very similar to the Hall field quadrupolar topology, which is characteristic of the X-line formation. After the guide field was suppressed, the Hall field pattern was even clearer; this lead to the conclusion that the background magnetic field polarity of the Bm component is strongly influenced by the Hall field in the vicinity of an X-line. A similar result was obtained regarding the polarity of the core field $B_{m\,CORE}$. Considering the separated effects of background and guide field of B_m in cases where a big guide field (considered big for values higher than 6 nT) was present, it was analyzed what could determine the polarity of the flux rope's core field. The polarity of the core field coincided with the polarity of one of those factors in most than 90% of the available results, so it was concluded that the polarity of $B_{m\,CORE}$ is strongly related to the polarity of the background magnetic field (which is at the same time strongly connected to the Hall field) and the polarity of the guide field.

Some flux ropes experience a motion opposing what should be expected. From

the distribution maps of the B_n and the B_m component, also the dependency of parameters like flux rope duration, length or background magnetic field magnitude with the distance to the neutral sheet and the separatrix where analyzed. Despite of not finding any clear evidence based on these statistics of how these factors could be influenced by the position relative to the X-line, a very interesting result was extracted from this analysis. There exist a family of flux ropes whose polarity on the oscillation of the B_n component does not correspond with what it should be expected for the quadrant where are detected. Those flux ropes are located in the lower right quadrant of Figure 5.16, correspondent to the southern hemisphere of the X-line's earthward side and they are characterized by a very short duration and a small amplitude on the B_n oscillation. In this regions, flux ropes should be expected to be encountered traveling to the Earth, away from the X-line, registering a minimum and then a maximum in the B_n component during a crossing, which is represented in the statistics as a red flux rope. However, many detections registering first a maximum and then a minimum represented as blue flux ropes where found in this region, which should mean those flux ropes are traveling not away from the X-line but towards it, opposing the direction of the ion outflow originated due to magnetic reconnection. Several studies regarding fully kinetic simulations of magnetic reconnection *[Nakamura. et. al, 2016]*[9] have already considered the possible existence of such structures, although the sources which could originate them are still uncertain. It may be possible, the motion of these flux ropes is driven due to an enhancement of the currents related to the Hall field, which could be enhanced in this region during a period of negative guide field. In any case, this is a very interesting result that could open new directions for future research which may surely clarify the mechanisms that originate the existence of such structures.

6.2 Outlook

The analysis realized during this work was focused on the detection of some known characteristic patterns of the magnetic field signatures. For this purpose, an analysis in time-domain was realized and the automatic search algorithm was configured to detect this patterns. Nevertheless, the results obtained for some of the flux ropes included lots of small scale oscillations superposed to the big traces of the signals, which lead to some unclear patterns in some of the detections, even when the conditions for detection were properly fulfilled.

Future perspectives of this work or similar studies should consider this fact and make a selective analysis of the data. One of the possibilities could be to realize a frequency selective filtering of the data by means of a filter bank, so that the multiple frequencies contained in the signal are split in different signals, for example using the wavelet transformation. Such a procedure could lead to much cleaner signals and with much better defined magnetic field patterns than the ones examined in this work.

The same time analysis could be then realized to this new signals, and even smaller scale structures could be found there, which could eventually be contained into bigger structures. Such situation cannot be detected with the former method, as only the bigger structure will be detected. Of course, this is only an idea and the method should be proved in order to determine its validity and viability, but it seems to be a proper and interesting path to move on, which maybe could solve some of the uncertainties found during this work.

Another improvement could be the definition of a flux rope model which considers the

flux rope as a 3 dimensional structure, and not like an in-plane 2 dimensional structure. This approach would be more realistic and may also produce better results when trying to compare the results obtained from real measurements with the results obtained from simulations*[Nakamura. et. al, 2016]*[9].

In any case, the result regarding the flux ropes from the analysis of section 5.5.1 moving in the opposite direction to what it should be expected is probably the most interesting result obtained from this work, since the existence of these structures was already predicted in simulations *[Nakamura. et. al, 2016]*[9] and this could be an evidence for its existence. A deep analysis of these specific type of structures could be a very interesting topic in which future studies based on the results of this work may be focused on.

Bibliography

[1] C.P. Escoubet, C.T. Russell, R. Schmidt *The Cluster and Phoenix Missions.* Kluwer Academic Publishers, 1997. ISBN 0-7923-4411-1

[2] R. Relindis: *Reconnection Events in the Near-Earth Magnetotail using Cluster data.* Graz University of technology. October 2010.

[3] W. Baumjohann, R.A. Treumann: *Basic Space Plasma Physics.* Imperial College Press, 1996. ISBN 1-86094-017X

[4] A. Alexandrova. *Magnetotail: Temporal Evolution and spatial characteristics.* Karl Franzens University, Graz 2016.

[5] M.A.Shay, J.F.Drake, B.N.Rogers and R.E.Denton. *Alfvénic collisionless magnetic reconnection and the Hall term.* Journal of Geophysical Research. Vol 106. March 1, 2001.

[6] W. Daughton, J. Scudder, and H. Karimabadi. *Fully kinetic simulations of undriven magnetic reconnection with open boundary conditions.* AIP Physics of plasmas, 2006.

[7] W.Daughton, V.Roythershteyn, H.Karimabadi, L.Yin, B.J.Albright, B.Bergen and K.J. Bowers. *Role of electron physics in the development of turbulent magnetic reconnection in collisionless plasma.* Nature Physics, 2011.

[8] G. Lapenta, S.Markidis, M. V. Goldman and D. L. Newmann , *Secondary reconnection sites in reconnection-generated flux ropes and reconnection fronts.* Nature Physics, 2015.

[9] T.K.M. Nakamura, R. Nakamura, Y. Narita, W. Baumjohann and W. Daughton. *Multi-scale structures of turbulent magnetic reconnection.* AIP Physics of Plasmas, 2016.

[10] M.Hesse, M. G. Kivelson. *The Formation and Structure of Flux Ropes in the Magnetotail.* Geophysical Monopgraph 105, 1998.

[11] A. L. Borg, M. G. G. T. Taylor, and J. P. Eastwood. *Observations of magnetic flux ropes during magnetic reconnection in the Earth's magnetotail.* Annales Geophysicae, 2012.

[12] W.-L. Teh, R. Nakamura, H. Karimabadi, W. Baumjohann, and T. L. Zhang. *Correlation of core field polarity of magnetotail flux ropes with the IMF By: Reconnection guide field dependency* Journal of Geophysical Research: Space Physics, 2013.

[13] J. Birn, J.F. Drake, M A Shay, B N Rogers, R. E Denton, M Hesse M. Kuznetsov, Z.W. Ma, A. Bhattacharjee A Otto and P. L. Pritchett. *Geospace Environmental Modeling (GEM) Magnetic Reconnection Challenge.* Journal of Geophysical Research, Vol. 106, Nº. A3, Pages 3715-3719, March 1, 2001.

[14] T. Nagai. I. Shinohara, M. Fujimoto, M. Hoshino, Y. Saito, S. Machida, and T. Mukai. *Geotail observations of the Hall current system: Evidence of magnetic reconnection in the magnetotail.* Journal of Geophysical Research, Vol. 106, Nº. A11, Pages 25.929-29.949, November 1, 2001.

[15] T. Nagai. I. Shinohara, M. Fujimoto, S. Machida, R. Nakamura, and T. Mukai. *Structure of the Hall current system in the vicinity of the magnetic reconnection site.* Journal of Geophysical Research, Vol. 108, Nº. A10, Pages 1357, 2003.

[16] P. L. Pritchett. *Geospace Environment Modeling magnetic reconnection challenge: Simulations with a full particle electromagnetic code.* Journal of Geophysical Research, Vol. 106, Nº. A3, Pages 3783-3798, March 1, 2001.

[17] W. J.Hughes and D. G. Sibeck. *On the three dimensional structure of plasmoids, Geophys.* Res. Lett., 14, 636, 1987.

[18] J. A. Slavin, R. P. Lepping, J. Gjerloev, M. L. Goldstein, D. H. Fairfield, M. H. Acuna, A. Balogh, M. Dunlop, M. G. Kivelson, K. Khurana, A. Fazakerley, C. J. Owen, H. Reme, and J. M. Bosqued. *Cluster electric current density measurements within a magnetic flux rope in the plasma sheet.* Geophysical Research Letters, Vol. 30, N^{circ}. 7, 1362, April 2003.

[19] G. Paschmann and P. W. Daly *Analysis Methods for Multi-Spacecraft Data.* International Space Science Institute, 1998.

[20] E. G. Zweibel, M. Yamada, The Royal Society Publishing: perspectives on magnetic reconnection,2016. Visited 27/03/2017.
`http://rspa.royalsocietypublishing.org/content/472/2196/20160479`

[21] European Space Agency (ESA): Cluster mission multimedia gallery. Visited 27/03/2017.
`http://www.mssl.ucl.ac.uk/www_plasma/missions/cluster/about_cluster/images/cn83262.gif`

[22] Mullard Space Science Laboratory (MSSL): Cluster mission multimedia gallery. Visited 27/03/2017.
`http://sci.esa.int/cluster/`

[23] Cluster Science Archive (CSA). Visited 27/03/2017.
`http://www.cosmos.esa.int/web/csa/about-this-archive`

[24] Harris Geospatial Solutions: IDL. Visited 27/03/2017.
`http://www.exelisvis.co.uk/ProductsServices/IDL.aspx`

[25] Harris Geospatial Solutions: IDL reference guide. Visited 27/03/2017.
`https://www.harrisgeospatial.com/docs/HELP.html`

[26] Time History of Events and Macroscale Interactions During Substorms(THEMIS): TDAS/SPEEDAS Framework. Visited 27/03/2017.
`http://themis.ssl.berkeley.edu/software.shtml`

[27] Wiki.Robotz forum: Wikipedia images. Visited 27/03/2017.
`http://wiki.robotz.com/images/9/97/Ion_ayers.jpg`

[28] Wikimedia commons: Photo Gallery. Visited 27/03/2017.
`https://upload.wikimedia.org/wikipedia/commons/thumb/0/02/Van_Allen_radiation_belt.svg/338px-Van_Allen_radiation_belt.svg.png`

[29] National Aeronautics and Space Administration (NASA): Goddard Space Flight Center. Visited 27/03/2017.
`https://mms.gsfc.nasa.gov/science.html`

[30] University of Colorado Boulder: Laboratory for Atmospherics and Space Physics. Visited 27/03/2017.
`http://lasp.colorado.edu/home/mop/files/2012/04/EarthJup.jpg`

[31] Shamer Blog: Typepad. Visited 27/03/2017.
`http://shamer.typepad.com/.a/6a0120a871ff88970b014e89179f56970d-pi`

Appendix

A. Tables containing the X-line information.

This appendix contains the four tables with the information about the multiple X-line reconnection events studied in this work where X-line information was available[4].

TABLE 1

No	$Date$ $yyyymmdd$	$t_{begin} - t_{end}$ $hhmmss - hhmmss$	Δt_{MVA} $hhmmss - hhmmss$	C_{MVA}	λ_2/λ_3	$\mathbf{L} = (L_x, L_y, L_z)$	$\mathbf{M} = (M_x, M_y, M_z)$	$\mathbf{N} = (N_x, N_y, N_z)$
1	20010827	040030-041100	-	-	-	(1.00, 0.00, 0.00)	(0.00, 1.00, 0.00)	(0.00, 0.00, 1.00)
2	20010910	074800-080500	072706-081001	C2	2.5	(1.00, 0.08, 0.02)	(-0.07, 0.97, -0.21)	(-0.04, 0.21, 0.98)
3	20020814	030700-031400	024800-025800	C2	3.3	(0.92, 0.39, 0.01)	(-0.38, 0.89, 0.26)	(0.10, -0.24, 0.97)
4	20020818	172700-173600	164030-165822	C1	5.4	(1.00, 0.03, -0.09)	(-0.00, 0.95, 0.31)	(0.10, -0.31, 0.95)
5	20020828	095200-101100	094300-095200	C4	28.2	(0.98, 0.20, 0.02)	(-0.19, 0.93, -0.32)	(-0.08, 0.31, 0.95)
6	20020913	180700-182500	175000-180400	C3	21.0	(0.99, -0.13, 0.01)	(0.13, 0.98, 0.12)	(-0.03, -0.12, 0.99)
7	20020918	130200-132030	124200-124904	C3	3.5	(0.95, -0.30, 0.12)	(0.32, 0.92, -0.24)	(-0.04, 0.27, 0.96)
8	20030822	132100-133500	-	-	-	(1.00, 0.00, 0.00)	(0.00, 1.00, 0.00)	(0.00, 0.00, 1.00)
9	20040819	175800-181500	175718-180311	C1	6.2	(0.99, 0.11, 0.01)	(-0.11, 0.97, 0.20)	(0.01, -0.20, 0.98)
10	20050828	233600-235100	231549-232107	C3	14.2	(0.96, 0.28, -0.04)	(-0.28, 0.95, -0.11)	(0.01, 0.12, 0.99)
11	20010817	162300-163830	160823-162128	C3	16.0	(0.93, 0.35, 0.15)	(-0.38, 0.87, 0.32)	(-0.02, -0.35, 0.93)
12	20010817	163830-165000	160823-162128	C3	16.0	(0.93, 0.35, 0.15)	(-0.38, 0.87, 0.32)	(-0.02, -0.35, 0.93)
13	20010822	094000-095400	-	-	-	(1.00, 0.00, 0.00)	(0.00, 1.00, 0.00)	(0.00, 0.00, 1.00)
14	20010822	094500-100400	-	-	-	(1.00, 0.00, 0.00)	(0.00, 1.00, 0.00)	(0.00, 0.00, 1.00)
15	20010912	130100-130930	123650-123941	C4	72.1	(0.98, -0.19, -0.03)	(0.19, 0.98, 0.04)	(0.02, -0.05, 1.00)
16	20010912	130930-131500	123650-123941	C4	72.1	(0.98, -0.19, -0.03)	(0.19, 0.98, 0.04)	(0.02, -0.05, 1.00)
17	20020814	035900-040730	034610-035700	C3	23.7	(0.94, 0.34, 0.04)	(-0.35, 0.92, 0.17)	(0.02, -0.17, 0.98)
18	20020814	040730-042000	034610-035700	C3	23.7	(0.94, 0.34, 0.04)	(-0.35, 0.92, 0.17)	(0.02, -0.17, 0.98)
19	20020818	170300-170945	164030-165822	C1	5.4	(1.00, 0.03, -0.09)	(-0.00, 0.95, 0.31)	(0.10, -0.31, 0.95)
20	20020818	170945-171700	164030-165822	C1	5.4	(1.00, 0.03, -0.09)	(-0.00, 0.95, 0.31)	(0.10, -0.31, 0.95)
21	20020821	080500-081630	074300-074700	grad	-	(0.97, 0.10, -0.04)	(-0.10, 0.96, -0.16)	(0.06, 0.17, 0.98)
22	20020821	081330-081930	074300-074700	grad	-	(0.97, 0.10, -0.04)	(-0.10, 0.96, -0.16)	(0.06, 0.17, 0.98)
23	20021026	091630-092200	091052-091235	C4	1.3	(0.72, -0.69, -0.06)	(0.67, 0.72, -0.18)	(0.17, 0.09, 0.98)
24	20031004	062000-062700	061425-061711	C1	31.1	(0.98, -0.16, 0.14)	(0.19, 0.95, -0.23)	(-0.10, 0.25, 0.96)

Figure B.1: Table 1/4 containing the X-line information.

TABLE 2

No	*Date*	$t_{begin} - t_{end}$	t_{ci}	α	Δt_s	Δr_{14}	Δr_{24}	Δr_{34}	Δt_{14}	Δt_{24}	Δt_{34}	t_{R_1}	t_{R_2}	t_{R_3}	t_{R_4}
	yyyymmdd	*hhmmss – hhmmss*	*s*		*s*	*km*	*km*	*km*	*s*	*s*	*s*	*hhmmss*	*hhmmss*	*hhmmss*	*hhmmss*
1	20010827	040030-041100	3.5	3	10	1790	1990	1930	-5.6	-17.8	-2.0	040655	040643	040659	040701
2	20010910	074800-080500	4.0	3	12	1700	2000	1840	-42.6	-29.4	-41.8	075613	075626	075614	075656
3	20020814	030700-031400	5.0	3	15	4380	3270	4100	-8.6	-9.6	-3.2	030944	030943	030950	030953
4	20020818	172700-173600	11.3	1	11	3730	3740	3700	-5.4	-6.4	1.8	172903	172902	172910	172908
5	20020828	095200-101100	5.1	3	15	4460	3250	4150	-25.8	20.8	16.2	100321	100408	100403	100347
6	20020913	180700-182500	7.3	3	22	3710	4230	3420	5.6	13.6	-17.2	181537	181545	181514	181531
7	20020918	130200-132030	3.5	3	11	3680	4110	3460	-42.8	10.6	-46.0	131046	131140	131043	131129
8	20030822	132100-133500	2.0	1	2	220	230	240	-2.0	-2.2	-2.0	132540	132539	132540	132542
9	20040819	175800-181500	3.8	1	4	900	1300	950	-5.6	-4.8	-3.8	180246	180247	180248	180252
10	20050828	233600-235100	3.4	1	3	8490	8470	1090	153.2	69.2	31.0	234335	234211	234133	234102
11	20010817	162300-163830	2.9	2	6	1850	2000	1960	-2.0	5.0	8.6	163453	163500	163504	163455
12	20010817	163830-165000	2.5	2	5	1860	1990	1950	-9.8	-2.6	0.4	164439	164446	164449	164449
13	20010822	094000-095400	4.5	3	13	1790	2000	1940	11.0	20.6	13.6	094429	094439	094432	094418
14	20010822	094500-100400	7.2	3	22	1790	1990	1930	-15.8	-31.4	7.0	095210	095155	095233	095226
15	20010912	130100-130930	3.4	3	10	1850	2010	1910	-10.0	-10.8	-14.2	130612	130611	130608	130622
16	20010912	130930-131500	4.1	3	12	1850	2000	1910	-17.2	-5.8	3.2	131126	131137	131146	131143
17	20020814	035900-040730	6.1	3	18	4630	3210	4200	-37.8	-22.8	-3.4	040314	040329	040349	040352
18	20020814	040730-042000	6.1	3	18	4670	3200	4190	-40.8	-51.4	-40.4	041153	041142	041153	041233
19	20020818	170300-170945	5.0	3	15	3710	3800	3660	-21.2	-12.0	-6.4	170828	170837	170842	170849
20	20020818	170945-171700	4.4	3	13	3720	3790	3660	-31.4	-12.0	-5.0	171032	171051	171058	171103
21	20020821	080500-081630	4.1	5	21	5100	3290	4380	35.0	18.2	13.8	081323	081306	081301	081248
22	20020821	081330-081930	2.4	5	12	5100	3270	4380	-26.4	-11.4	6.6	081750	081805	081823	081816
23	20021026	091630-092200	2.4	3	7	4520	4920	3390	-79.2	-18.6	-5.4	091759	091900	091913	091919
24	20031004	062000-062700	3.3	1	3	220	240	240	1.0	0.8	1.4	062242	062242	062242	062241

Figure B.2: Table 2/4 containing the X-line information.

TABLE 3

No	*Date*	$t_{begin} - t_{end}$	$\|\mathbf{U}\|$	$\delta_{\|\mathbf{U}\|}$	U_L	U_M	U_N	k_L	k_M	k_N	X_{GSM}	Y_{GSM}	ϕ	$\|\phi - \phi_r\|$	u_r	δ_{u_r}	$-\nabla_r P$	dN/dt
	yyyymmdd	*hhmmss – hhmmss*	*km/s*	*km/s*	*km/s*	*km/s*	*km/s*				R_E	R_E	*deg*	*deg*	*km/s*	*km/s*		
1	20010827	040030-041100	103	±7	-33	-92	-33	-0.32	-0.89	-0.32	-19	-2	70	64	43	±3	< 0	< 0
2	20010910	074800-080500	35	±2	-32	-1	15	-0.91	-0.01	0.42	-19	2	-0	6	32	±2	< 0	-
3	20020814	030700-031400	309	±26	-235	-199	-30	-0.76	-0.64	-0.10	-18	-6	61	41	224	±19	-	-
4	20020818	172700-173600	380	±34	-164	-268	-214	-0.43	-0.71	-0.56	-17	-5	47	30	231	±21	< 0	-
5	20020828	095200-101100	57	±3	-23	51	-6	-0.41	0.90	-0.11	-19	-2	-52	59	27	±2	< 0	-
6	20020913	180700-182500	119	±7	-18	47	108	-0.15	0.40	0.91	-17	2	-67	60	19	±1	< 0	> 0
7	20020918	130200-132030	50	±3	-39	14	27	-0.78	0.29	0.55	-18	4	-44	31	39	±1	< 0	> 0
8	20030822	132100-133500	90	±21	-16	-58	-68	-0.18	-0.64	-0.75	-18	-4	74	62	28	±7	-	< 0
9	20040819	175800-181500	145	±17	-122	-73	27	-0.84	-0.50	0.18	-17	-6	38	20	136	±16	-	-
10	20050828	233600-235100	33	±2	-13	-1	-30	-0.41	-0.04	-0.91	-17	-4	34	20	14	±1	-	< 0
11	20010817	162300-163830	168	±14	-86	71	-126	-0.51	0.42	-0.75	-18	-5	-36	51	81	±10	< 0	< 0
12	20010817	163830-165000	162	±14	-154	51	-7	-0.95	0.32	-0.05	-18	-5	2	13	158	±14	> 0	-
13	20010822	094000-095400	95	±6	33	78	-43	0.35	0.82	-0.46	-19	-3	67	57	46	±3	> 0	> 0
14	20010822	094500-100400	47	±3	-22	-36	-19	-0.48	-0.78	-0.41	-19	-3	58	48	29	±2	< 0	< 0
15	20010912	130100-130930	127	±10	-108	-48	45	-0.85	-0.38	0.36	-19	3	14	23	108	±8	< 0	> 0
16	20010912	130930-131500	88	±6	-46	-4	-74	-0.53	-0.05	-0.85	-19	3	-9	0	48	±3	< 0	< 0
17	20020814	035900-040730	88	±5	-84	-12	-22	-0.96	-0.13	-0.25	-18	-6	25	6	83	±5	-	< 0
18	20020814	040730-042000	59	±3	-25	-49	22	-0.42	-0.83	0.37	-18	-6	84	65	25	±1	-	< 0
19	20020818	170300-170945	170	±11	-156	-60	-31	-0.92	-0.35	-0.18	-17	-5	18	2	167	±11	< 0	> 0
20	20020818	170945-171700	112	±7	-104	-21	-35	-0.93	-0.18	-0.31	-17	-5	6	10	106	±7	< 0	< 0
21	20020821	080500-081630	131	±8	129	19	-0	0.99	0.15	-0.00	-18	-4	14	1	128	±8	-	-
22	20020821	081330-081930	101	±6	-86	4	-53	-0.85	0.04	-0.52	-18	-4	9	5	88	±5	-	< 0
23	20021026	091630-092200	55	±3	-16	25	-46	-0.28	0.46	-0.84	-11	11	-86	41	19	±1	-	-
24	20031004	062000-062700	152	±49	-75	74	109	-0.50	0.49	0.72	-16	7	-58	33	110	±6	-	> 0

Statistical characteristics for the distributions of absolute values

maximum	380		235	268	214								231			
minimum	33		13	1	0								14			
median	102		61	49	32	0.52	0.41	0.41					65			
mean	120		76	57	50	0.61	0.43	0.45					83			
standard deviation	82		60	62	48.1	0.28	0.29	0.28					64			

Figure B.3: Table 3/4 containing the X-line information.

TABLE 4

No	*Date* *yyyymmdd*	$t_{begin} - t_{end}$ *hhmmss − hhmmss*	v_{out1}/v_{out2}	$\Delta t_1/\Delta t_2$	u *km/s*	δ_u	v_{in} *km/s*	$\delta_{v_{in}}$ $^o/_o$	$C_{v_{in}}$	B_L *nT*	B_L/B_0	v_{out} *km/s*	δv_{out} $^o/_o$	ξ	δ_ξ	ε	δ_ε
1	20010827	040030-041100	0.85	1.68	33	±2	106	5-10	1	18.5	0.7	693	5-10	0.05	±0.005	0.15	±0.016
2	20010910	074800-080500	0.63	0.17	32	±2	45	< 5	4	15.8	0.8	448	< 5	0.07	±0.005	0.10	±0.004
3	20020814	030700-031400	0.52	0.34	235	±20	-	-	-	-	-	863	< 5	0.27	±0.025	-	-
4	20020818	172700-173600	0.32	0.07	164	±15	251	5-10	1	7.6	0.4	951	5-10	0.17	±0.020	0.26	±0.028
5	20020828	095200-101100	0.73	1.46	23	±1	35	5-10	1	17.9	0.7	885	5-10	0.03	±0.002	0.04	±0.004
6	20020913	180700-182500	1.22	0.76	18	±1	59	5-10	1	12.5	0.5	734	5-10	0.02	±0.002	0.08	±0.009
7	20020918	130200-132030	0.94	1.25	39	±2	41	5-10	1	21.8	0.8	322	5-10	0.12	±0.011	0.13	±0.014
8	20030822	132100-133500	2.62	0.59	16	±4	131	5-10	4	33.8	0.9	1089	5-10	0.01	±0.004	0.12	±0.013
9	20040819	175800-181500	0.40	0.13	122	±14	127	< 5	4	16.0	0.6	616	< 5	0.20	±0.024	0.21	±0.009
10	20050828	233600-235100	0.85	0.05	13	±1	-	-	-	-	-	1205	5-10	0.01	±0.001	-	-
11	20010817	162300-163830	2.76	0.39	86	±7	78	5-10	3	39.6	0.8	913	5-10	0.09	±0.010	0.09	±0.009
12	20010817	163830-165000	2.52	7.79	154	±13	180	5-10	4	30.8	1.0	797	5-10	0.19	±0.022	0.23	±0.024
13	20010822	094000-095400	0.96	0.29	33	±2	42	5-10	3	6.7	0.3	982	5-10	0.03	±0.003	0.04	±0.005
14	20010822	094500-100400	0.82	0.32	22	±1	26	5-10	3	22.3	0.9	1127	5-10	0.02	±0.002	0.02	±0.002
15	20010912	130100-130930	0.22	0.52	108	±8	200	< 5	1	17.4	0.7	540	5-10	0.20	±0.022	0.37	±0.030
16	20010912	130930-131500	0.23	1.15	46	±3	42	5-10	1	20.6	0.9	948	10-20	0.05	±0.008	0.04	±0.007
17	20020814	035900-040730	1.46	2.81	84	±5	140	5-10	3	15.3	0.8	907	5-10	0.09	±0.009	0.15	±0.016
18	20020814	040730-042000	0.36	0.16	25	±1	-	-	-	-	-	1509	5-10	0.02	±0.002	-	-
19	20020818	170300-170945	0.91	2.29	156	±11	182	5-10	4	15.6	0.7	432	5-10	0.36	±0.037	0.42	±0.045
20	20020818	170945-171700	0.47	0.32	104	±6	185	5-10	1	15.0	0.8	508	5-10	0.21	±0.020	0.36	±0.039
21	20020821	080500-081630	1.01	2.19	129	±8	56	5-10	3	22.1	0.7	923	5-10	0.14	±0.014	0.06	±0.006
22	20020821	081330-081930	0.78	1.30	86	±5	124	20-50	4	26.7	1.0	1271	10-20	0.07	±0.011	0.10	±0.037
23	20021026	091630-092200	1.01	0.80	16	±1	64	5-10	4	23.0	0.8	632	5-10	0.02	±0.002	0.10	±0.011
24	20031004	062000-062700	0.89	0.69	75	±24	138	10-20	1	18.4	1.0	927	5-10	0.08	±0.027	0.15	±0.025

Statistical characteristics for the distributions

maximum	2.76	7.79	235		251					1509		0.36		0.42	
minimum	0.22	0.05	13		26					322		0.01		0.02	
median	0.85	0.64	61		106					896		0.08		0.12	
mean	0.98	1.15	76		107					843		0.11		0.15	
standard deviation	0.71	1.61	60		65					287		0.09		0.12	

Figure B.4: Table 4/4 containing the X-line information.

B. The Cluster Science Archive (CSA)

First of all, the data object of study has to be acquired. Data from the cluster mission will be used for the purpose of this study and it can be freely downloaded from the *Cluster Science Archive (CSA)* after registration. The *Cluster Science Archive (CSA)* is the long-term archive for ESA's Cluster mission and became publicly available in November 2013. It is provided and maintained alongside ESA's other solar system science archives at ESAC, located near Madrid, Spain. The archive provides online access to high-quality, validated, high-resolution data from the Cluster instruments together with auxiliary and support data products (e.g. orbit information). In addition, the CSA provides value-added capabilities such as data visualization services and VO support. The CSA services can be accessed either via its Java based Graphical User Interface or by using its Archive Inter-Operability interface (command line)[23]. This latter was the method used to acquire the desired data from Table 4.1 from the CSA, a script named *'cdf_Jose.pro'* was developed in IDL introducing this feature.

Figure B.5 is a capture of the *Graphical User Interface (GUI)* of the CSA. As can be seen there, the different fields allow an intuitive selection of the desired data, time range and mission. Finally, the desired data can be downloaded in *CEF (Cluster Exchange Format)* or *CDF (Common Data Format)*. The CEF-format is intended to be used for exchange of science data between instrument teams, while CDF is a product by NASA and Goddard Space Flight Center and it's free to all users, being the latter the format selected to acquire data in this thesis.

For this work only data from the Cluster mission was used, and the experiments whose data was acquired are the two ones highlighted in Figure B.5, to wit, the *Cluster Ion Spectrometer (CIS)* and the *Flux Gate Magnetometer (FGM)*. Both instruments where previously explained in detail in Chapter 3, so in this section the focus will be on the data selected from every experiment and not on the technology.

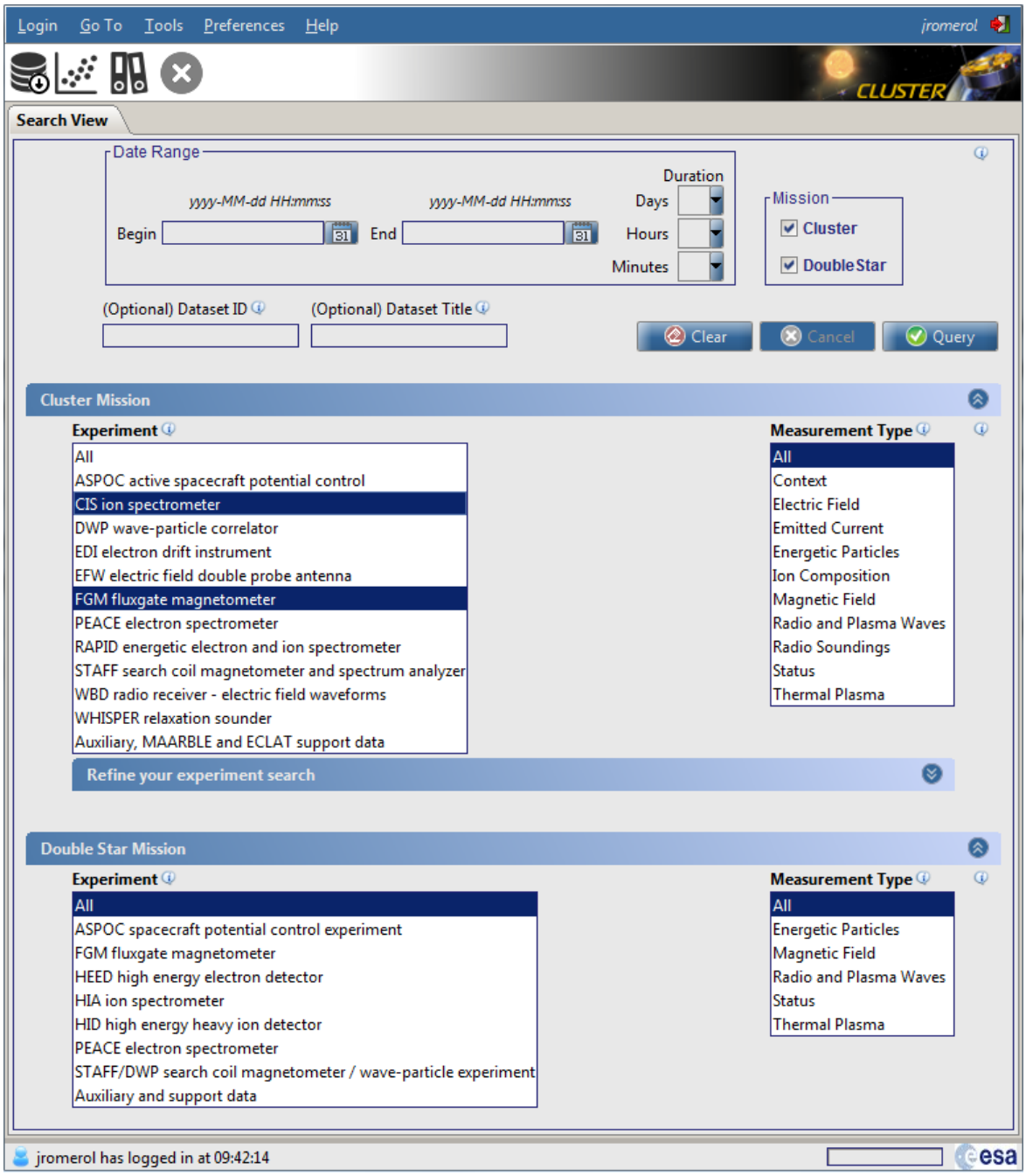

Figure B.5: Main screen of the Graphical User interface of the Cluster Science archive.

Cluster Ion Espectrometer (CIS)

The *Cluster Ion Spectrometer (CIS)* collects information about the properties of ionized particles. The measurements of the Ion velocities can be obtained for major ionized particles (H^+,He^+ and O^+) through *CODIF (Composition and distribution Function Analyser)* or for a particle beam (many ionized particles) through *HIA (Hot Ion Analyzer)*, further information about the working principle of both instruments was already discussed in Chapter 3.

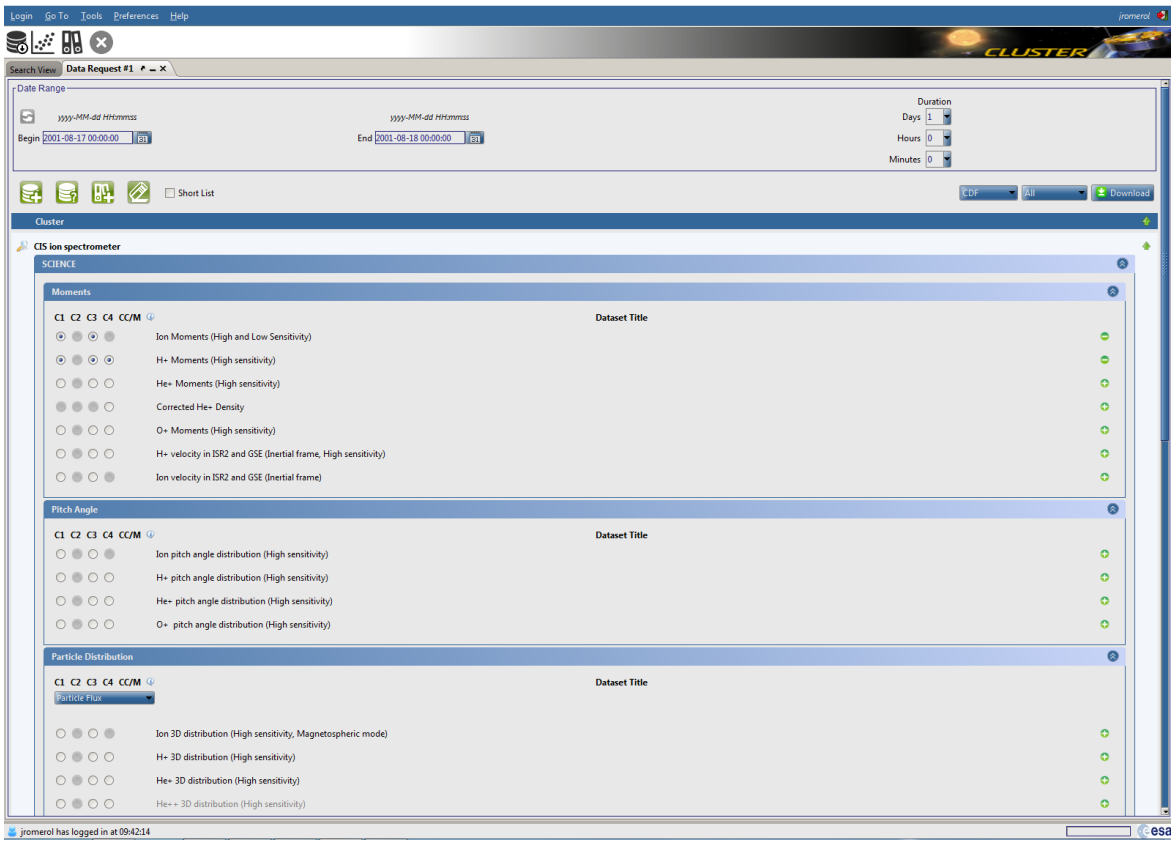

Figure B.6: List of *CIS* Experiment data on Graphical User interface of the Cluster Science archive.

Accessing the CSA and selecting the CIS experiment gives access to the whole list of different data available from CIS as shown in Figure B.6. For the purpose of this work, it will be needed to examine the velocities of the ions, which are given by the ion moments. The velocity of the hydrogen ions (H^+) is of special importance, as they are protons, the more basic positively charged particle, this is referred in the *GUI* as 'H^+ Moments'. Also the velocity of all ion families detected by HIA will be evaluated as an alternative parameter for the velocity of the ions through the spacecraft, this appears in the CIS measurements as 'Ion Moments'. The time resolution of these measurements equals the time of one spacecraft spin, being this 4 seconds.

The CDF file obtained from the HIA for cluster spacecraft 1 named *C1_CP_CIS-*

HIA_ONBOARD_MOMENTS contains the following information shown in Table B.1:

Variable name	**Description**
density	Proton particle density in cm^{-3}
pressure	Total pressure
pressure_tensor	Pressure tensor in GSE
temperature	Temperature in MK
temperature_par	Temperature parallel to B in MK
temperature_perp	Temperature perp. to B in MK
velocity_gse	Velocity in GSE in $\frac{km}{s}$
velocity_isr2	Velocity in ISR2 in $\frac{km}{s}$
cis_mode	CIS operational mode
delta_time	Half interval duration
sensitivity	Sensitivity (0:low, 1:High)
time_tags	Internal centered time tag

Table B.1: List of all variables included in the CDF file *C1_CP_CIS-HIA_ONBOARD_MOMENTS* from the *CIS HIA* 'Ion moments (High and low sensitivity)' analysis.

On the other hand, for CODIF of spacecraft 1, the CDF file named in this case *C1_CP_CIS-CODIF_HS_H1_MOMENTS* contains the variables shown in Table CODIF:

Variable name	**Description**
density	Proton particle density in cm^{-3}
pressure	Pressure tensor in GSE
T	Temperature in MK
T_par	Temperature parallel to B in MK
T_perp	Temperature perp. to B in MK
velocity	Velocity in GSE in $\frac{km}{s}$
duration	Half interval duration
time_tags	Acquisition interval center time

Table B.2: List of all variables included in the CDF file *C1_CP_CIS-CODIF_HS_H1_MOMENTS* from the I 'Ion moments (High and low sensitivity)' analysis.

The velocity of the ions is one if not the most important variable of the CIS instrument concerning this study. It is defined in both instruments in *GSE (Geocentric coordinate system)*, being the velocities defined for a single spacecraft in x,y and z directions of this system. The velocity of the Ions play not an important role in the process of flux rope detection, but it will be important for later statistical studies. For that reason, the 4 seconds sampling rate corresponding to the spin rate is acceptable in this case.

It is also patent from Figure B.6,that data from each spacecraft is not always available, in particular, CIS from cluster spacecraft 2 was damaged soon after the moment the satellites

were launched and it never worked, so no plasma data of cluster 2 is available for this experiment.

Flux Gate Magnetometer (FGM)

The FGM provides information about measured magnetic field. Each spacecraft has two tri-axial flux gate magnetometers with an on-board data processing unit, leading to measurement of magnetic field vector data. Detailed information about the functioning of the FGM was already given in Chapter 3.

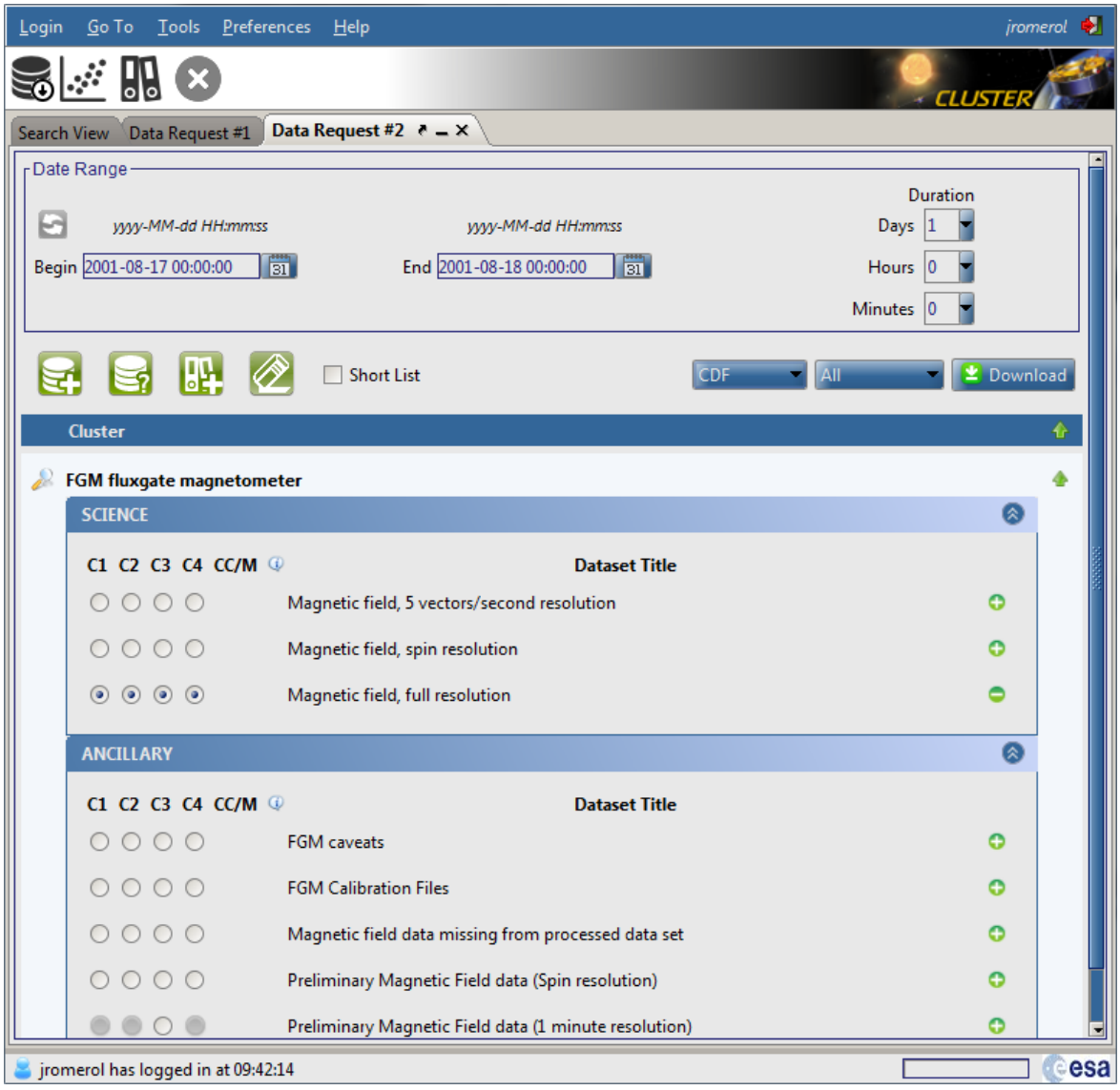

Figure B.7: List of FGM Experiment data on Graphical User interface of the Cluster Science archive.

As can be seen in Figure B.7, different resolutions are available for data from the FGM. Spin resolution refers to one measurement for spacecraft needs to spin completely, which is 4 seconds sampling rate, this is the same resolution that the CIS instrument hat. On the other hand, full resolution data has a sampling frequency of 22 Hz, correspondent to a sampling rate of 0.04461 sec.The use of full resolution data of the FGM is the most adequate for the purpose of this work, as the detection of small scale flux ropes is an indispensable issue and most of them would not be detected using spin resolution of 4 seconds sampling rate. The CDF file obtained from the FGM experiment for cluster spacecraft 1 named *C1_CP_FGM_FULL* contains the following information shown in Table FGM:

Variable name	**Description**
B_mag	Magnetic field magnitude given in nT, full resolution
B_vec_xyz_gse	Magnetic field vector in GSE given in nT, full resolution
sc_pos_xyz_gse	Spacecraft position in GSE
half_interval	Half averaging interval length
range	FGM instrument range, defined on full resolution time line
Time_tags	Interval centred time tag
tm	FGM telemtry mode (burst mode/normal mode) on full resolution time line

Table B.3: List of all variables included in the CDF file *C1_CP_FGM_FULL* from the FGM "magnetic field, full resolution" analysis.

Especially important for the intended study of flux ropes are the variables *B_vec_xyz_gse* and *B_mag*. The first of them includes the measurements of the magnetic field vector data in GSE with 22 kHz of sampling frequency, those three vector components of the magnetic field will be the main object of study for the detection of flux ropes, as they will be identified searching for a very specific pattern in the magnetic field components. The latter is the absolute value of the magnetic field for full resolution data, which is also an important parameter to consider for proper flux rope detection, it is related to the vector components as $|B| = \sqrt{B_x^2 + B_y^2 + B_z^2}$. Unlike from data from CIS, for FGM spin resolution will not have the required accuracy, this is why full resolution data is selected.

Accessing the CDF files, IDL and TDAS-SPEEDAS

As occurs in every work that includes the treatment and processing of data and signals, proper software will be necessary to handle the data obtained from the CSA. This work was realized using the commercial software *IDL (Interactive Data Language)*, a programming language used for data analysis, which is popular in particular areas of science, such as astronomy, atmospheric physics and medical imaging. Besides the wide range of possibilities which IDL already offers, the *TDAS (Themis Data Analysis Software)-SPEEDAS (Space Physics Environment Data Analysis Software)* libraries will be also included in IDL. TDAS-SPEEDAS is a user-developed software package based in IDL syntaxes which implements many useful functions for the management and analysis of the data in CDF format downloaded from the CSA.

Before starting to analyze the data, some modifications had to be done. The files down-

loaded from the CIS and FGM experiments are compact CDF files which include the variables shown in Tables B.1, B.2 and B.3. IDL can access the content of these variables through various specific commands to read CDF format, the ones used for this work are:

CDF_OPEN: It opens an existing Common Data Format (CDF) file, the CDF ID is stored in a new variable.

CDF_INQUIRE: This command returns global information about the Common Data Format file using the ID as input. Coding of the file, variables dimensions and number of variables among others are shown as output.

CDF_VARINQ: This function returns a structure containing information about the specified variable in a CDF file. Variable name, dimensions or data type (FLOAT, DOUBLE, INT, CHAR, EPOCH) conform among others the output of this command.

CDF_CONTROL: This procedure allows the user to obtain or set information for a CDF file, its variables and its attributes. It is the main control deck for the contents of the CDF file. Mostly all information regarding the CDF file or the information encoded inside can be accessed using this procedure.

CDF_VARGET: By means of this procedure, multiple values from a variable contained inside a CDF file can be read. This is the procedure which is used to extract the values from the variables in a ready-to-use format.

CDF_EPOCH: This procedure computes or breaks down CDF_EPOCH values included in a CDF file. The epoch value is the number of milliseconds since 1 January 2000 at the time $00:00:00$, and it is the variable which indicates the time at which each measurement is taken. This procedure switches from Epoch format to its equivalent date and vice versa.

CDF_CLOSE: This command closes the specified CDF file. It flushes all CDF's data buffers, closes all of the CDF's open files and frees the CDF ID. Used when the information of a CDF is already extracted and no longer needed.

Those are the commands which were used to handle the CDF files, although the list of procedures that IDL possesses to work with CDF files is much longer. Further information regarding the commands can be found in the IDL manual [25].

The variables which are contained in a CDF file contain all the information measured by a single spacecraft in x, y and z directions on GSE as can be seen from the names and descriptions of the variables shown in Tables B.1, B.2 and B.3 such as 'B_vec_xyz_gse' or 'velocity_gse'. This arrangement of the data is not very appropriate for the objective of this study, as it would be much more efficient to have each of the measurements of one direction in GSE from all spacecraft together. For this reason, a new set of variables is created from the ones extracted from the CDF file. Variables which contained vector information in GSE are rearranged to 3 new different variables, each one with the information regarding one direction for all four spacecrafts, while non-vector variables are just grouped into a single new variable

with the information regarding each spacecraft in a separated column. The importance of this rearrangement is primal, since the methodology for the flux rope detection explained in Chapter 4 needs the data of each component of all four spacecrafts together.

So far, the capabilities that IDL offers to access and handle data from the CSA were mentioned. On the other hand, for the deep analysis of this data, the big core of functions and tools used during this work will belong to TDAS/SPEEDAS. The TDAS/SPEEDAS software offers the user a wide range of possibilities to analyze spacecraft data in time or frequency domain, switch data from one coordinate system to another or find the minimum variance coefficients of a matrix, among other functionalities. The functions from TDAS which were mainly used during this work are:

tplot: Creates a time series plot from user defined quantities. The input variables need to be previously created with the function *store_data:* The variables to be plotted using the *tplot* function can be created from the user using this function, the tags to be represented in each of the axis of the time series are also defined here.

tplot_names: This procedure gives as output a matrix of strings containing the names of the existing *tplot* variables. It is useful to determine the number of existing variables.

time_double: This routine takes as input a date (in string format *YYYY-MM-DD/hh:mm:ss*) and returns the number of seconds since January 1st of 1970, which is the 0 point of the *tplot* time series. It is important to remember, that epoch value from the CDF files of the cluster spacecraft is referenced in milliseconds to the 1st of January of 2000, so a conversion of this epoch value has to be realized. The routines *CDF_EPOCH* and *time_double* allow this conversion.

time_string: This routine makes the inverted sequence of *time_double*. An epoch value referenced to 1st of January 1970 is introduced as input and a string containing the date is obtained as output.

timebar: This commands takes an epoch value or a string containing a date as input and places a vertical line in the *tplot* time series. This function will be very useful to determine visually the exact point where a flux rope is detected.

tlimit: Allows the user to zoom in or out on the *tplot* time series. The initial value of scaling can be restored using the command *tlimit, /FULL*.

minvar_matrix_make: This routine generates a matrix or set of matrices from a time series of 3-d vector data that will transform three dimensional data into a minimum variance coordinate system. It takes a *tplot* variable that stores 3 dimensional vector data as an input argument and produces a *tplot* variable storing the transformation matrix or matrices.

tvector_rotate: Using this routine an array of data can be rotated by a set of coordinate transformation matrices, inputs and outputs are *tplot* variables. This will be used to rotate the GSE coordinate matrices to a minimum variance coordinate system using minimum

variance transformation matrices.

Combining the main functions of IDL and the capabilities of TDAS/SPEEDAS, there are plenty of tools available to execute a deep and detailed analysis of the data acquired from the CSA. The methodology followed in this work for the detection of the flux ropes, and how the signals containing the information of the variables in the CDF files of the CSA have to be examined to determine the existence of such structures was presented in Chapter 4.

C. The Minimum Variance Analysis (MVA)

The main purpose of *Minimum* or *Maximum Variance Analysis (MVA)* is to find, from single-spacecraft data, an estimator for the direction normal to a one-dimensional or approximately one-dimensional current layer, wave front, or other transition layer in a plasma. In the case of the Minimum variance analysis of the magnetic field (MVAB) the normal vector $\hat{\mathbf{n}}$ acquired by crossing of the current sheet will be estimated. The new coordinate system obtained through this analysis is called LMN coordinate system and will be much more adequate to detect the magnetic field patterns of the flux ropes, since it is referenced to the current sheet.

During a time traversal of the current sheet, several measurements from a magnetometer are registered $\mathbf{B^{(m)}}$ $(m = 1, 2, 3, \cdots, M)$. The method identifies that direction in space along which the field-component set $\left\{\mathbf{B^{(m)}} \cdot \hat{\mathbf{n}}\right\}$ $(m = 1, 2, 3, \cdots, M)$ has minimum variance, which is obtained by minimization of the variance function.

$$\sigma = \frac{1}{M}\left|\mathbf{B^{(m)}} - \langle \mathbf{B} \cdot \hat{\mathbf{n}} \rangle\right|^2 \tag{B.1}$$

$$\langle \mathbf{B} \rangle = \frac{1}{M}\sum_{m=1}^{M} \mathbf{B^{(m)}} \tag{B.2}$$

The minimization is now subjected to the normalization constraint $|\hat{\mathbf{n}}|^2 = 1$ implemented using a lagrange multiplier λ. The solution is now the set of three linear homogeneous equations:

$$\frac{\partial}{\partial n_x}\left(\sigma^2 - \lambda\left(|\hat{\mathbf{n}}|^2 - 1\right)\right) = 0 \tag{B.3}$$

$$\frac{\partial}{\partial n_y}\left(\sigma^2 - \lambda\left(|\hat{\mathbf{n}}|^2 - 1\right)\right) = 0 \tag{B.4}$$

$$\frac{\partial}{\partial n_z}\left(\sigma^2 - \lambda\left(|\hat{\mathbf{n}}|^2 - 1\right)\right) = 0 \tag{B.5}$$

After the differentiations are realized, the equation set can be written in matrix form as follows.

$$\sum_{v=1}^{3} M^B_{\mu\nu} n_\nu = \lambda_\mu \tag{B.6}$$

Where the subscripts μ,$\nu = 1, 2, 3$ denote the cartesian X,Y,Z components of the former system and $M^B_{\mu\nu}$ is the magnetic variance matrix. Since $M^B_{\mu\nu}$ is symmetric, the eigenvalues are all real and the corresponding eigenvectors, x_1, x_2, and x_3, are orthogonal. The three eigenvectors represent the directions of maximum, intermediate, and minimum variance of the field component along each vector.

$$\mathbf{M^B_{\mu\nu}} = \langle \mathbf{B}_\mu \mathbf{B}_\nu \rangle - \langle \mathbf{B}_\mu \rangle \langle \mathbf{B}_\nu \rangle \tag{B.7}$$

Summarizing, the minimum variance analysis consists of constructing the magnetic variance matrix $M^B_{\mu\nu}$ in terms of the measured field data and the cartesian coordinate system

in which the measured data are represented, and then finding the three correspondent eigenvalues λ_i and eigenvectors x_i of the matrix. The eigenvector x_3 corresponding to the smallest eigenvalue, is used as the estimator for the vector normal to the current sheet and λ_3 itself represents the variance of the magnetic field component along the estimated normal. The eigenvectors x_1 and x_2, correspond to maximum and intermediate variance, and are tangential to the transition layer. The eigenvector set $\{x_1, x_2, x_3\}$ arranged as a right-handed orthonormal triad provides suitable basis vectors for the local coordinates[19].

D. Additional statistics.

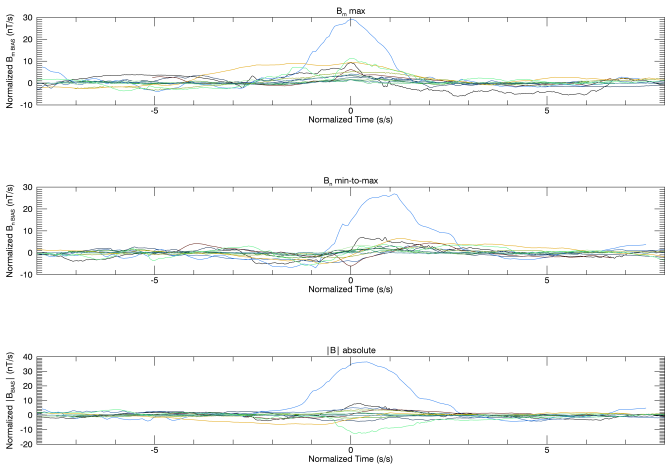

(a) Case 1 - Full range

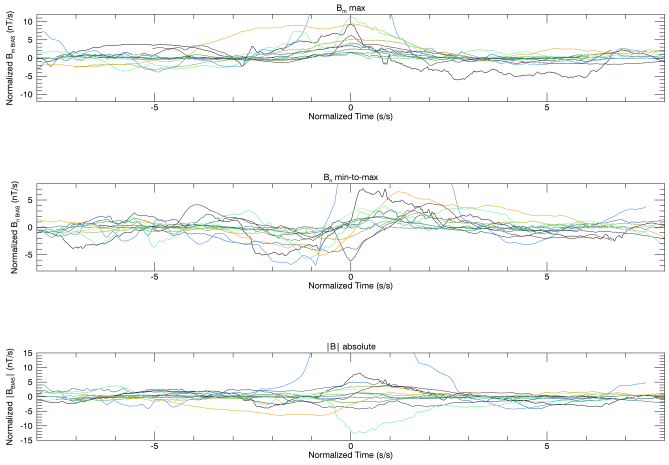

(b) Case 1 - Reduced range

Figure B.8: Figures representing **case 1**: variation from minimum to maximum on B_n and maximum in B_m, all values are normalized relative to the background values. The range of values the bottom figure is zoomed referring to the upper

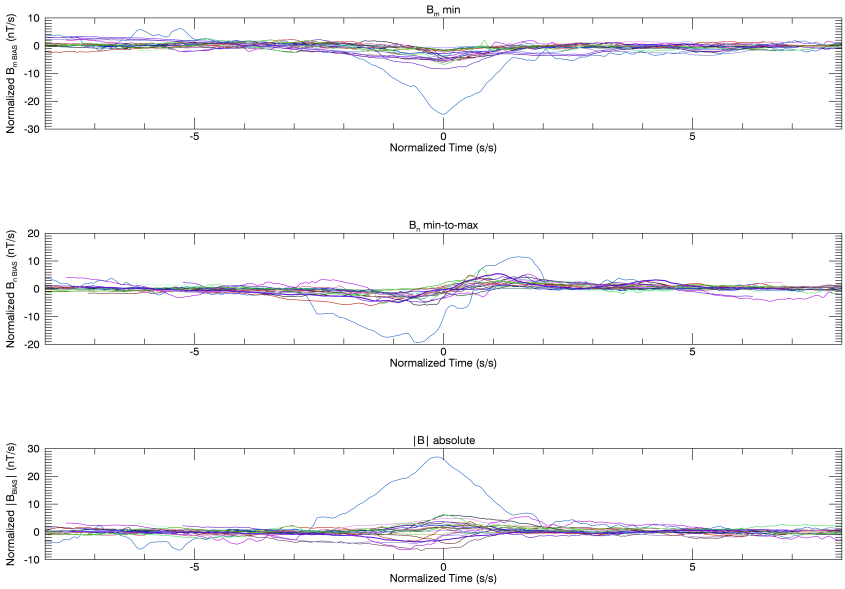

(a) Case 2 - Full range

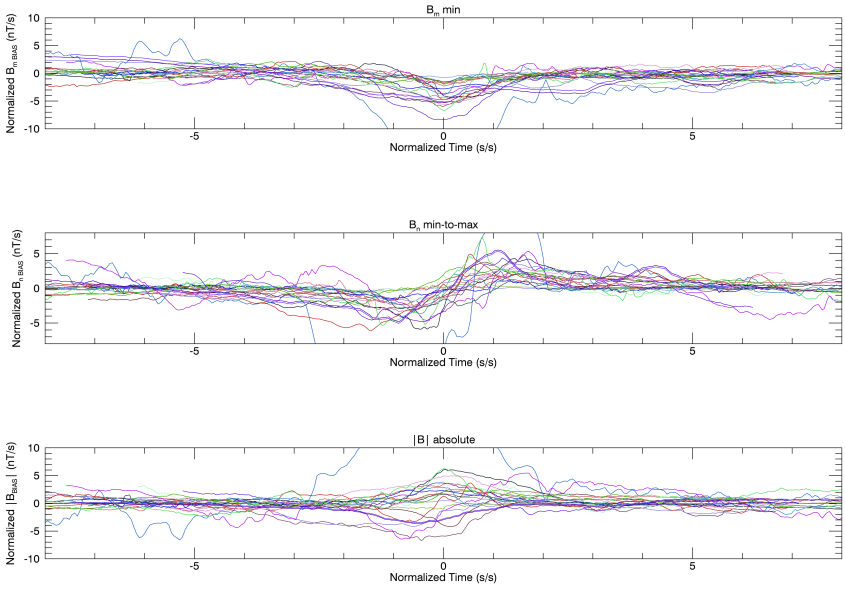

(b) Case 2 - Reduced range

Figure B.9: Figures representing **case 2**: variation from minimum to maximum on B_n and minimum in B_m, all values are normalized relative to the background values. The range of values the bottom figure is zoomed referring to the upper

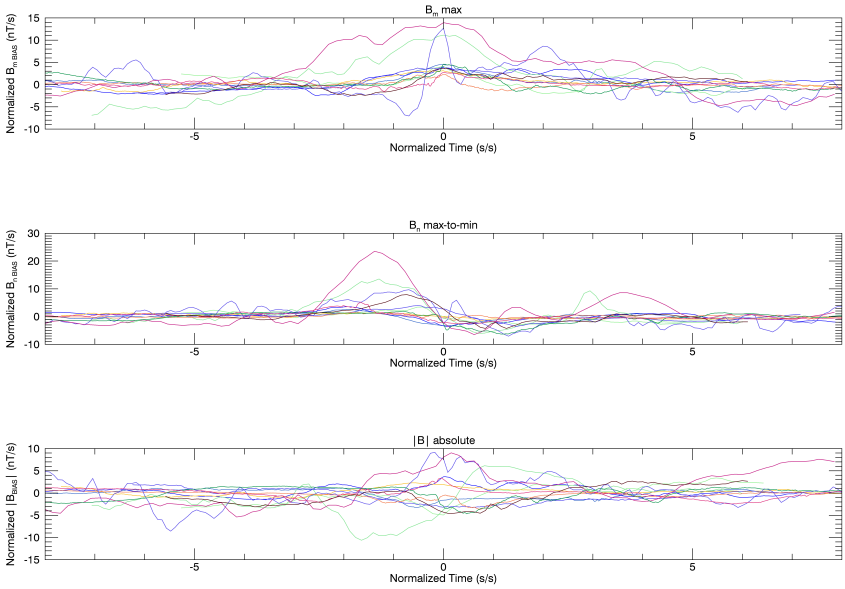

(a) Case 3 - Full range

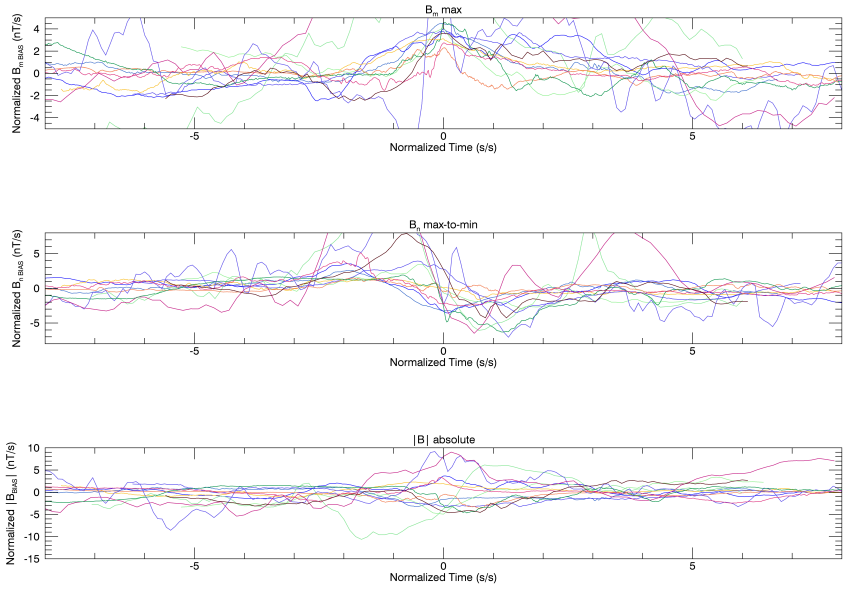

(b) Case 3 - Reduced range

Figure B.10: Figure representing **case 4**: variation from maximum to minimum on B_n and minimum in B_m, all values are normalized relative to the background values. The range of values the bottom figure is zoomed referring to the upper

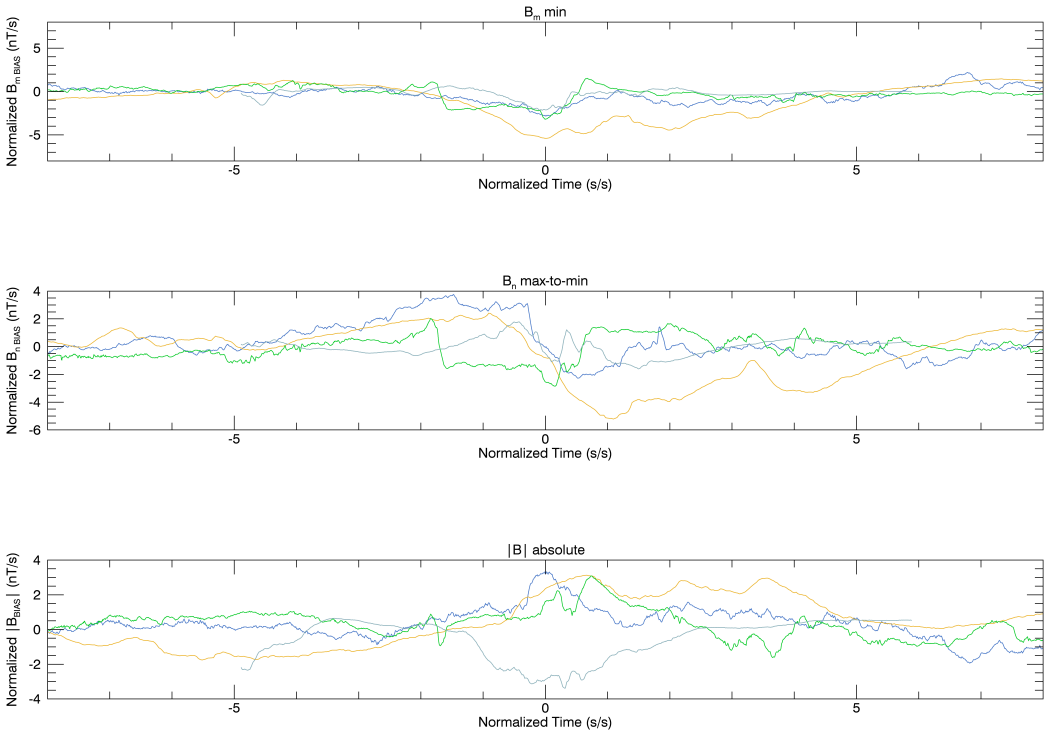

Figure B.11: Figures representing **case 3**: variation from maximum to minimum on B_n and minimum in B_m, all values are normalized relative to the background values.

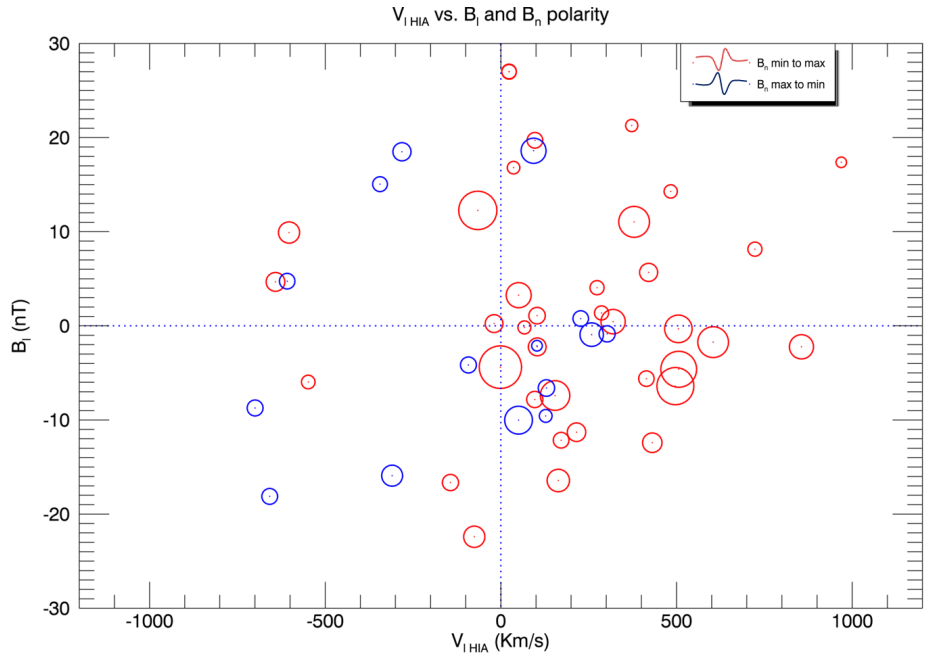

(a) B_n polarity and duration using $V_{l\,HIA}$

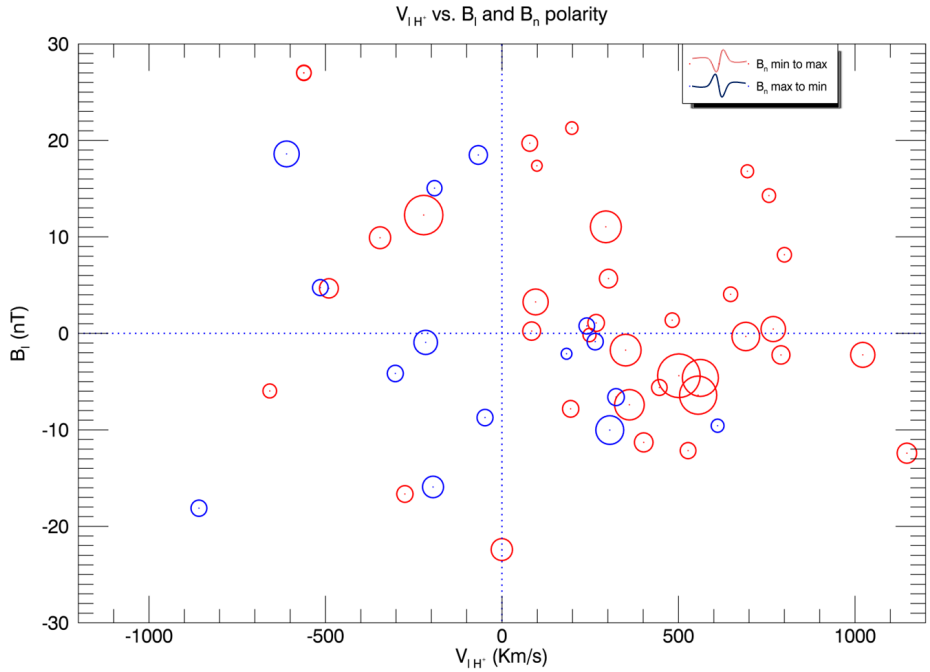

(b) B_n polarity and duration using $V_{l\,H+}$

Figure B.12: Spatial distribution map of the flux ropes and the polarity of the B_n oscilation using the auxiliary parameters $V_{l\,HIA}$ (Top) and $V_{l\,H^+}$ (Bottom). The duration of the flux ropes are normalized and represented by the size of each circle.

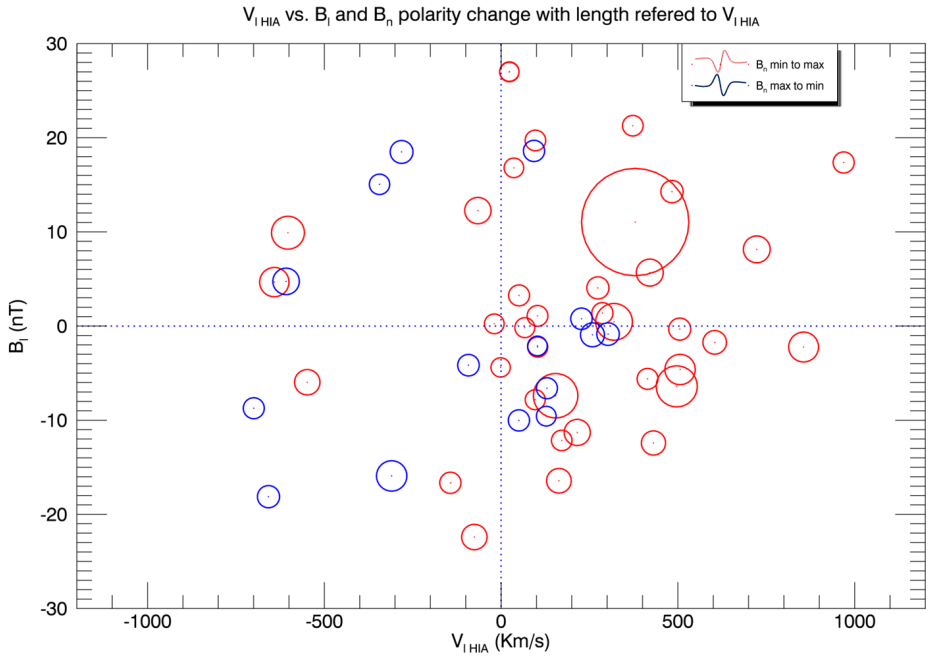

(a) B_n polarity and size using $V_{l\,HIA}$

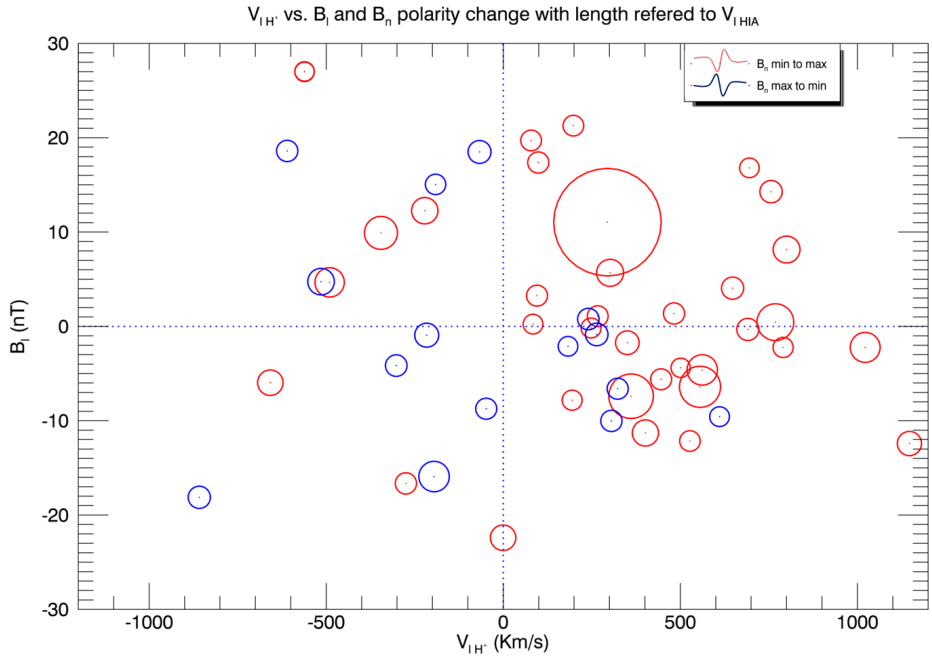

(b) B_n polarity and size using $V_{l\,H+}$

Figure B.13: Spatial distribution map of the flux ropes and the polarity of the B_n oscilation using the auxiliary parameters $V_{l\,HIA}$ (top) and $V_{l\,H+}$ (bottom). The size of the flux ropes referring to $V_{l\,HIA}$ are normalized and represented by the size of each circle.

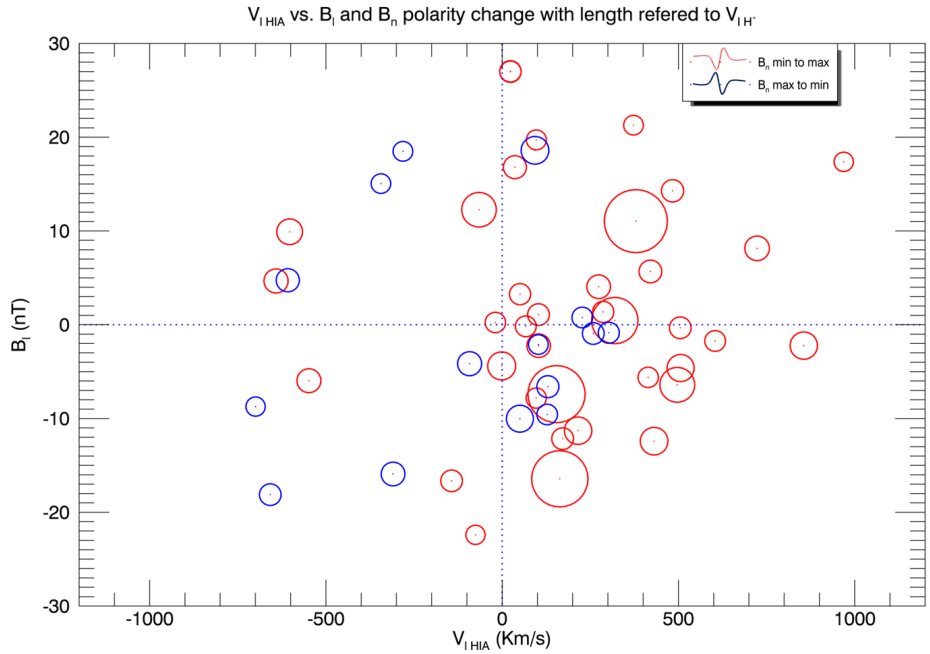

(a) B_n polarity and size using $V_{l\,HIA}$

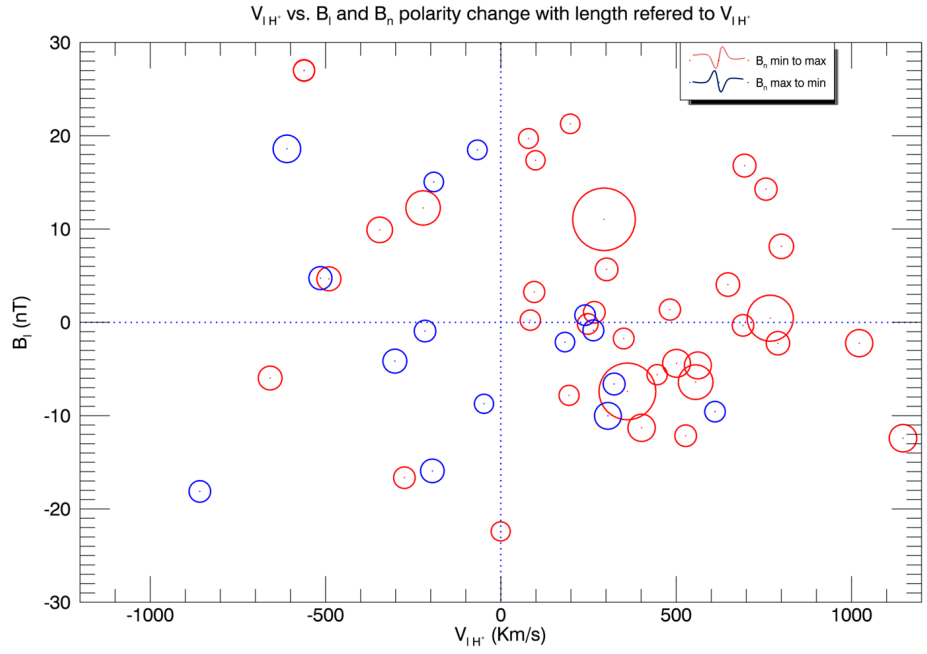

(b) B_n polarity and size using $V_{l\,H+}$

Figure B.14: Spatial distribution map of the flux ropes and the polarity of the B_n oscilation using the auxiliary parameters $V_{l\,HIA}$ (top) and $V_{l\,H+}$ (bottom). The size of the flux ropes referring to $V_{l\,H+}$ are normalized and represented by the size of each circle.

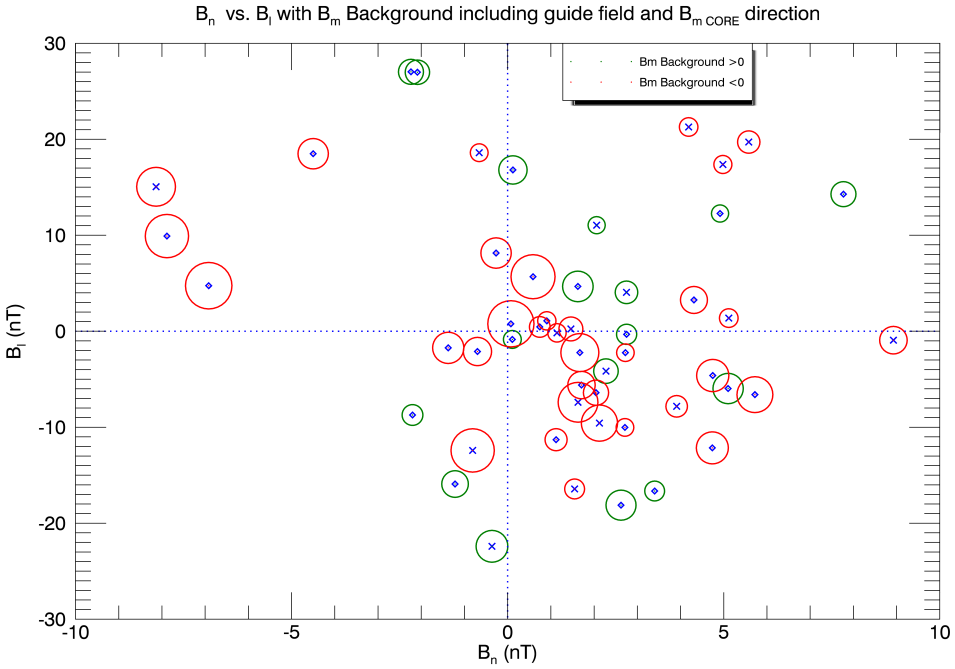

(a) B_m background polarity with guide field using B_n

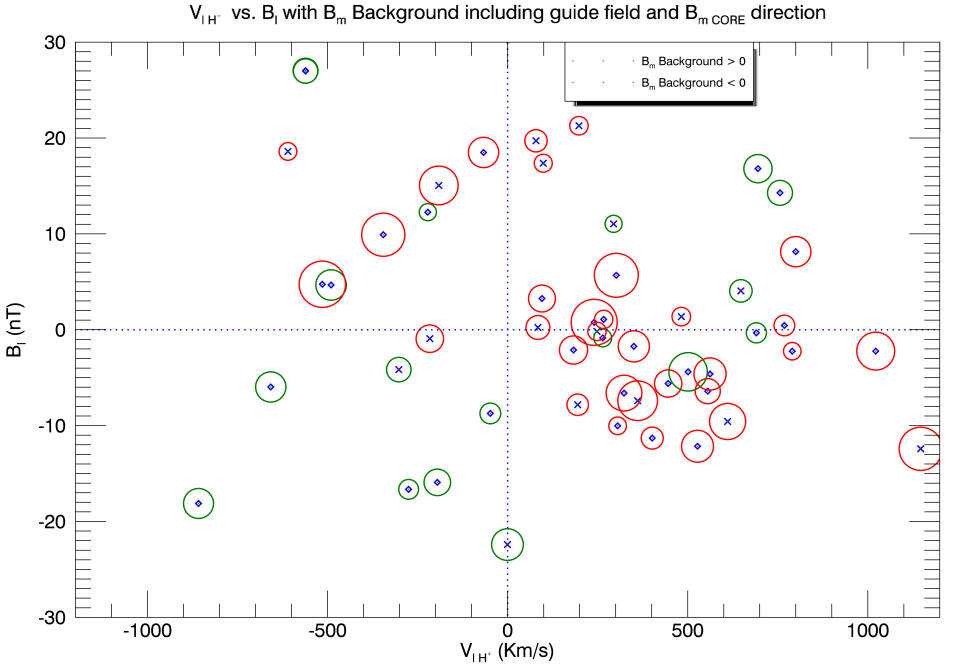

(b) B_m background polarity with guide field using $V_{l\,H+}$

Figure B.15: Spatial distribution map of the flux ropes and the polarity of the B_m background including the guide field using the auxiliary parameter B_n (top) and $V_{l\,H+}$ (bottom). The direction of the core field is represented by a diamond if coincides with the background and a cross if they are anti-parallel.

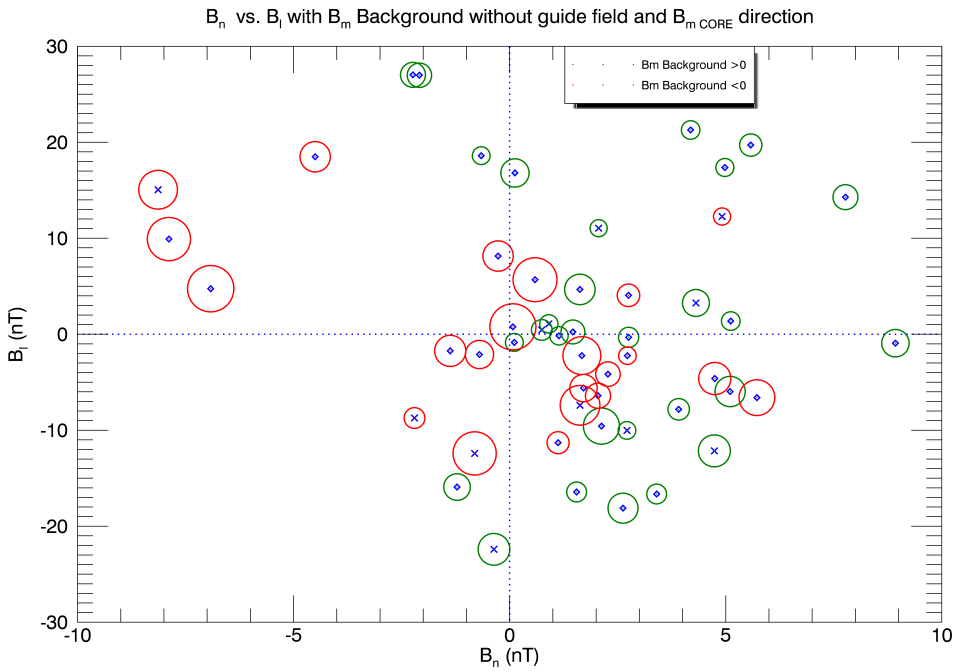

(a) B_m background polarity without guide field using B_n

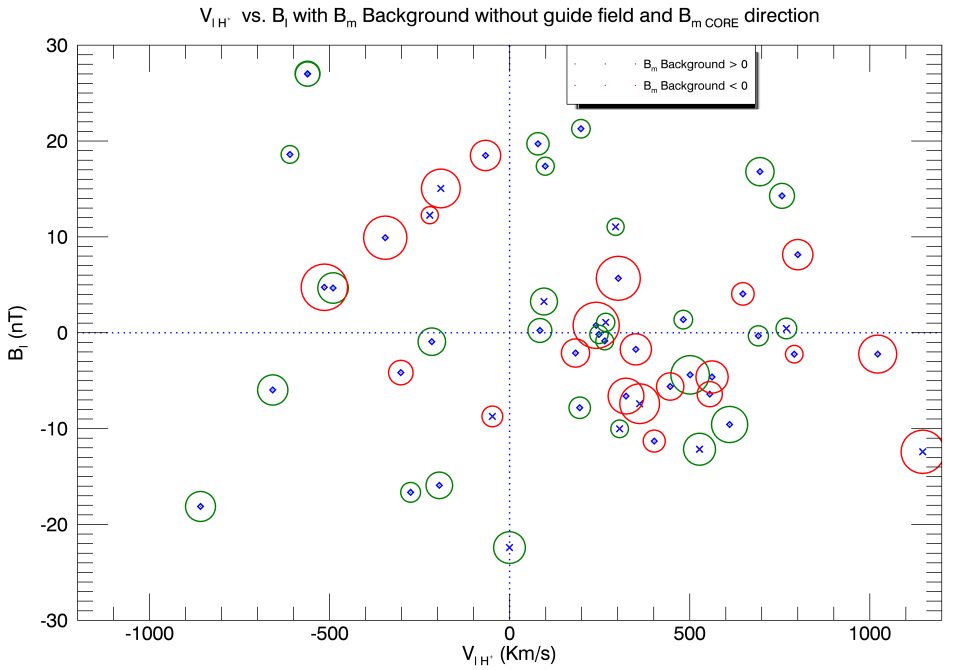

(b) B_m background polarity without guide field using $V_{l\,H+}$

Figure B.16: Spatial distribution map of the flux ropes and the polarity of the B_m background without the guide field using the auxiliary parameter B_n (top) and $V_{l\,H+}$ (bottom). The direction of the core field is represented by a diamond if coincides with the background and a cross if they are anti-parallel.

List of Figures

List of Tables

List of Abbreviations

CDF Compact Data Format

MVA Minimum Variance Analysis

GSE Geocentric Solar Ecliptic

CSA Cluster Science Archive

CPU Central Processing Unit

ESA European Space Agency

TDAS Themis Data Analysis Software

SPEDAS Space Physics Environment Data Analysis Software

CIS Cluster Ion Spectromenter

FGM Flux Gate Magnetometer

HIA Hot Ion Analyzer

CODIF COmposition and DIstribution Function analyzer

WEC Wave Experiment Consortium

STAFF Spatio-Temporal Analysis of Field Fluctuations

EFW Electric Field Wave experiment

WHISPER Waves of High frequency and Sounder for Probing of Electron density

WBD Cluster Wide-BanD plasa wave

DWP Digital Wave Processing

EDI Electron Drift Instrument

ASPOC Active Spacecraft POtential Control

PEACE Plasma Electron and Current Experiment

RAPID Research with Adaptive Particle Imaging Detectors

MHD Magnetohydrodynamics

PSBL Plasma Sheet Boundary Layer

AU Astronomical Unit

HMT HydroMagnetic Theorem

IMF Interplanetary Magnetic Field

NENL Near Earth Neutral Line

DNL Distant Neutral Line

MEP Main Equipment Plattform

RCS Reaction Control System

OBDH On Board Data Handling

AOCMS Attitude and Orbit Control and Measurement

DPU Data Processing Unit

IDL Interactive Data Language

MSC Multi SpaceCraft